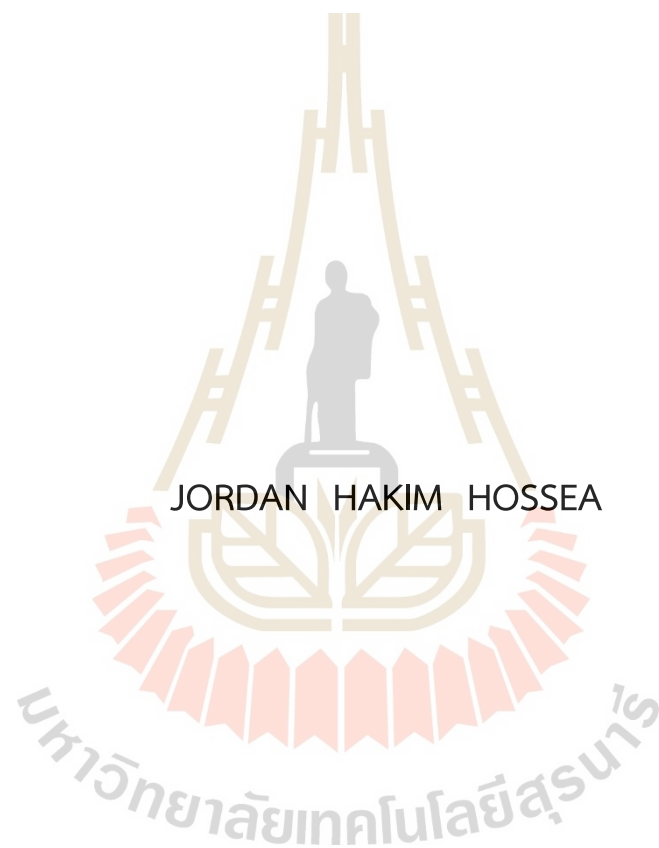


STUDIES OF SURFACE PLASMON RESONANCE SENSOR USING
DIVERGENT BEAM AND MISALIGNMENT EFFECTS OF SENSOR CHIP



A Thesis Submitted in Partial Fulfillment of the Requirements for the
Degree of Doctor of Philosophy in Electrical Engineering
Suranaree University of Technology
Academic Year 2021

การศึกษาเซนเซอร์แบบคลื่นผิวพลาสมอนเรโซแนนซ์โดยใช้ลำแสงกระจาย
และผลกระทบจากการติดตั้งชิพเซนเซอร์



นายจอร์แดน ฮาคิม โฮสเซีย

วิทยานิพนธ์นี้เป็นส่วนหนึ่งของการศึกษาตามหลักสูตรปริญญาวิศวกรรมศาสตรดุษฎีบัณฑิต
สาขาวิชาวิศวกรรมไฟฟ้า
มหาวิทยาลัยเทคโนโลยีสุรนารี
ปีการศึกษา 2564

STUDIES OF SURFACE PLASMON RESONANCE SENSOR USING DIVERGENT
BEAM AND MISALIGNMENT EFFECTS OF SENSOR CHIP

Suranaree University of Technology has approved this thesis submitted in
partial fulfillment of the requirements for the Degree of Doctor of Philosophy

Thesis Examining Committee



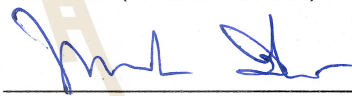
(Dr. Siriwat Soontaranon)

Chairperson



(Prof. Dr. Joewono Widjaja)

Member (Thesis Advisor)



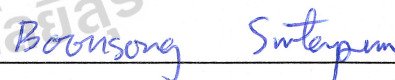
(Assoc. Prof. Dr. Panomsak Meemon)

Member



(Dr. Wanvisa Talataisong)

Member



(Asst. Prof. Dr. Boonsong Sutapun)

Member



(Assoc. Prof. Dr. Chatchai Jothityangkoon)

Vice Rector for Academic Affairs
and Quality Assurance



(Assoc. Prof. Dr. Pornsiri Jongkol)

Dean of Institute of Engineering

นายจอร์แดน ฮาคิม โฮสเซีย: การศึกษาเซนเซอร์แบบคลื่นผิวพลาสมอนเรโซแนนซ์โดยใช้
ลำแสงกระจายและผลกระทบจากการติดตั้งชิพเซนเซอร์ (STUDIES OF SURFACE
PLASMON RESONANCE SENSOR USING DIVERGENT BEAM AND MISALIGNMENT
EFFECTS OF SENSOR CHIP) อาจารย์ที่ปรึกษา : ศาสตราจารย์ ดร.โจโวโน วิดจาया, 93
หน้า.

คำสำคัญ: เซนเซอร์แบบคลื่นผิวพลาสมอนเรโซแนนซ์/ช่วงการตรวจวัดแบบกว้าง/ลำแสงกระจาย/
เลนส์ฟาวเวลล์/การติดตั้งชิพเซนเซอร์แบบมีช่องว่าง/การแทรกสอด

งานวิจัยนี้มีจุดประสงค์ 2 ส่วน ในส่วนแรกคือเพื่อทำงานวัดดัชนีหักเหของแสงในช่วงวัดที่
กว้าง โดยใช้การติดตั้งแบบ Kretschmann ด้วยลำแสงแบบกระจาย ส่วนที่สองคือการศึกษา
ผลกระทบของสัญญาณ SPR ที่จากการติดตั้งชิพเซนเซอร์

วิทยานิพนธ์นี้เสนอการใช้เซนเซอร์แบบคลื่นผิวพลาสมอนเรโซแนนซ์ (SPR) โดยใช้การติดตั้ง
แบบ Kretschmann สำหรับการวัดดัชนีหักเหของแสงในช่วงวัดที่กว้างซึ่งใช้ลำแสงแบบกระจาย
ในขั้นตอนการทดลองตัวอย่างของสารที่แตกต่างกันจะถูกจัดวางบนพื้นที่เซ็นเซอร์ที่ใช้ในการวัดและ
แบ่งอย่างเป็นสัดส่วน ซึ่งสามารถทำให้วัดได้หลายตัวอย่างในการวัดเพียงครั้งเดียวจึงช่วยลดเวลาใน
การวัดค่าดัชนีหักเหของแสงของแต่ละตัวอย่าง ในการทดลองนี้เลนส์ฟาวเวลล์ถูกใช้เพื่อสร้าง
พลังงานโฟตอนที่สม่ำเสมอซึ่งจำเป็นต่อการเกิดคลื่นผิวพลาสมอนเรโซแนนซ์ขนาดใหญ่ระหว่างชั้น
โลหะและชั้นตัวอย่างไดอิเล็กทริก วิธีการที่นำเสนอมีข้อได้เปรียบมากกว่าวิธีการวัดเชิงมุมแบบทั่วไป
ซึ่งนอกจากจะปราศจากการสแกนเชิงกลและสามารถถ่ายโอนพลังงานโฟตอนที่สม่ำเสมอแล้ว ยังให้
ผลลัพธ์การสะท้อนของแสงแบบเชิงเส้น ซึ่งส่งผลให้โปรแกรมสามารถตรวจวัดได้ง่าย การศึกษานี้
ได้แสดงให้เห็นว่าในการวัดหนึ่งครั้งสามารถครอบคลุมดัชนีหักเหของแสงตั้งแต่ 1.0003 ~
1.3580

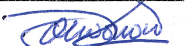
การศึกษาผลกระทบของสัญญาณ SPR ที่จากการติดตั้งชิพเซนเซอร์ได้ทำการศึกษาทั้งทาง
ทฤษฎีและปฏิบัติ จากผลการทดลองพบว่าผลกระทบจากความหนาของกระจกที่ใช้ทำชิพเซ็นเซอร์มี
มากกว่าผลกระทบที่เกิดจากช่องว่างที่เกิดจากการติดตั้งชิพด้วยน้ำมัน matching index เนื่องจาก
ความหนาของกระจกที่ใช้ทำชิพเซ็นเซอร์มีค่ามากกว่าช่องว่างนั้นๆ และการแทรกสอดจากการ
สะท้อนหลายครั้งทำให้สัญญาณของ SPR ถูกบดบัง นอกจากนี้งานวิจัยนี้พบว่าช่องว่างระหว่าง
เซ็นเซอร์และปริซึมเนื่องมาจากอากาศจะไม่สามารถทำให้เกิดคลื่นผิวพลาสมอนเรโซแนนซ์ได้เพราะ
อากาศขัดขวางการถ่ายเทพลังงานโฟตอนกับประจุที่พื้นผิว

สาขาวิชาวิศวกรรมอิเล็กทรอนิกส์
ปีการศึกษา 2564

ลายมือชื่อนักศึกษา



ลายมือชื่ออาจารย์ที่ปรึกษา



JORDAN HAKIM HOSSEA : STUDIES OF SURFACE PLASMON RESONANCE SENSOR USING DIVERGENT BEAM AND MISALIGNMENT EFFECTS OF SENSOR CHIP. THESIS ADVISOR : PROF. JOEWONO WIDJAJA, Ph.D., 93 PP.

Keyword: Surface Plasmon Resonance/Wide Dynamic Range/Divergent Beam Illumination/Powell Lens/Misalignment Gap/Interference Fringe.

This thesis proposes an optical implementation of Kretschmann-based surface plasmon (SPR) sensor for wide dynamic range of refractive index measurements by using divergent beam illumination. In the proposed method, different samples are spatially distributed across either a large or a partitioned sensing area. Instead of taking sequentially multiple measurements of samples having different refractive indices, a parallel measurement of different samples could be done in a single-shot acquisition, which reduces a response time. In order to measure simultaneously broad refractive index variation, Powell lens is used to generate uniform photon energy required to resonate surface plasmons on a large interface between a metal sensing layer and dielectric samples. The proposed method has advantages over the conventional angular interrogation methods in that besides being free from mechanical scanning and able to transfer uniform photon energy, it provides a linear SPR reflectance output, resulting in simple detection algorithm. Single-shot measurements of the refractive index variation from 1.0003 ~ 1.3580 are experimentally demonstrated.

Finally, this research work studies theoretically and experimentally effects of a misalignment of the gold-coated glass sensing plate on SPR reflectivity signal. The investigation discovered that because the glass thickness is more than matching liquid (ML), there is interference fringe generation on the SPR signal. Again, it was discovered that the interference fringe amplitude grows as the glass thickness increases. Additionally, it was determined through analysis and observation that the ML gap-induced misalignment of the glass plate has no impact on the SPR signal because the ML gap thickness is significantly smaller than the glass thickness. Lastly the study found that the misaligned glass plate resulted by the air does not produce SPR phenomena because air hinders photon energy transfer, hence no interaction between the surface charges and photons.

School of Electronics Engineering
Academic Year 2021

Student's Signature _____
Advisor's Signature _____

ACKNOWLEDGEMENTS

I would like to express my gratitude to My Lord Jesus Christ for good health provision and sufficient vitality to complete this thesis at Suranaree University of Technology, Thailand.

Prof. Dr. Joewono Widjaja, my adviser, deserves my heartfelt gratitude for his constant support, insightful guidance, patience, inspiration, and encouragement during my studies. Apart from that, he showed me how to achieve anything meaningful by requiring commitment, perseverance, discipline, and focus. Despite his intelligent suggestions, I was constantly given the chance to develop and test my ideas based on my inquisitive mind.

Special gratitude should also be extended to the committee for, which includes Dr. Siriwat Soontaranon (Chairperson), Assoc. Prof. Dr. Panomsak Meemon (Member), Dr. Wanvisa Talataisong (Member), and Asst. Prof. Dr. Boonsong Sutapun (Member), for their constructive suggestions, comments, and support.

I am joyful to extend my heartfelt gratitude to all staff and other workers in the School of Electronic Engineering for their generosity and assistance.

I am grateful to Suranaree University of Technology (SUT), School of Electronic Engineering, for providing me with the Vithedbundith Scholarship during my studies.

Also, a big thank you to Miss. Waramanee Netphrueksaratb and Mr. Sangchai Paijit for their help with the experiment and motivating each other as a team.

Special appreciation should go to my lovely wife Flora J. Mangula, as well as my son Hospian and daughter Rafrona. They have been a continual source of love and support for me.

Lastly, I would want to convey my gratitude to all members of Christian Community Center and all friends who have become part of my family for their generosity and spiritual support.

Jordan Hakim Hossea

TABLE OF CONTENTS

	Page
ABSTRACT (THAI).....	I
ABSTRACT (ENGLISH).....	II
ACKNOWLEDGEMENTS.....	III
TABLE OF CONTENTS.....	IV
LIST OF TABLES.....	VII
LIST OF FIGURES.....	VIII
SYMBOLS AND ABBREVIATIONS.....	XII
CHAPTER	
I INTRODUCTION	1
1.1 Literature review.....	1
1.2 Significance of the study.....	9
1.3 Problem statement.....	9
1.4 Research procedure.....	10
1.5 Scope of the study.....	10
1.6 Expected result.....	10
1.7 Organization of the thesis.....	11
II GENERAL THEORY	12
2.1 General theory of surface plasmon resonance.....	12
2.1.1 Evanescent wave.....	12
2.1.2 Surface plasmon resonance.....	15
2.2 Transmittance and reflectance in multilayer media.....	17
2.3 Propagation of TM waves in Kretschmann prism configuration.....	19
2.3.1 Electric field incident on the prism.....	21
2.3.2 Electric field transmitted at the air-prism interface.....	23
2.3.3 Electric field incident at the prism-gold interface.....	27
2.3.4 Electric field transmitted at the prism-gold interface.....	29
2.3.5 Electric field incident at the gold-sample interface.....	32
2.3.6 Electric field transmitted at the gold-sample interface.....	34
2.3.7 Electric field reflected from the sample-gold interface.....	38

TABLE OF CONTENTS (Continued)

	Page
2.3.8 Electric field incident at the gold-prism interface.....	41
2.3.9 Electric field transmitted at the gold-prism interface.....	43
2.3.10 Electric field transmitted at the prism-air interface	46
III RESEARCH METHODOLOGY.....	51
3.1 Introduction.....	51
3.2 Divergent beam illumination and detection	51
3.2.1 SPR sensor using Powell lens	51
3.2.2 Fan, Illumination and Observation Angles	52
3.2.3 Beam widths.....	53
3.3 Effects of misalignment gap.....	55
3.3.1 Analysis of interference fringe on the SPR signal	59
3.3.2 Verification of the existence of the interference fringe.....	61
IV EXPERIMENTAL VERIFICATIONS.....	63
4.1 Beam shaping with Powell lens.....	63
4.2 Experimental measurement of refractive index.....	64
4.2.1 Simultaneous sensing of air and water.....	66
4.2.2 Simultaneous sensing of air and ethanol.....	68
4.2.3 Sensor sensitivity	69
4.3 Misalignment effects	71
4.3.1 Simulation Results.....	71
4.3.1.1 Simulation results of uniform misalignment	72
4.3.1.2 Simulation results of the non-uniform misalignment.....	73
4.3.2 Experimental results.....	74
4.3.2.1 Misalignment effects caused by the ML gap	74
4.3.2.2 Misalignment effect caused by the air gap	76
4.3.3 Discussion of the experimental misalignment effects.....	77
4.4 Experimental analysis of the fringes spacing.....	78
V CONCLUSION AND FUTURE WORKS	82
5.1 Conclusion	82
5.2 Future works.....	83

TABLE OF CONTENTS (Continued)

	Page
5.3 Challenges in implementing.....	83
REFERENCES	84
APPENDICES	
APPENDIX A PUBLICATIONS.....	91
BIOGRAPHY	93



LIST OF TABLES

Table	Page
1.1 Commercially available SPR sensors operates under angular interrogation principles.....	8
4.1 Errors in measurements of the refractive indices and their corresponding resonance angles of the three samples.....	70
4.2 Comparison of the experimental and the theoretical fringe spacings as the function of the incident angle θ_1	80



LIST OF FIGURES

Figure		Page
2.1	A schematic diagram of a TM beam propagation at the boundary of two-layer media.....	10
2.2	Vector wavefields of the incident, the transmitted and the reflected TM wave in the Kretschmann-based equilateral prism configuration.....	20
2.3	Plot of the angle of incidence for the air-prism interface as a function of the angle of incidence for the prism-gold interface.....	21
2.4	The squared modulus of the electric field components (a) $ E_{ix-01} ^2$ and (b) $ E_{iz-01} ^2$ incident on the air-prism interface.....	23
2.5	Variation of the transmission coefficients and as a function of the angle of incidence for the prism-gold interface.....	25
2.6	The squared modulus of the electric fields (a) $ E_{tx-01} ^2$ and (b) $ E_{tz-01} ^2$ as a function of the angle of incidence θ_1 for the prism-gold interface.....	27
2.7	The squared modulus of the electric fields (a) $ E_{ix-012} ^2$ and (b) $ E_{iz-012} ^2$ as a function of the angle of incidence θ_1 for the prism-gold interface.....	28
2.8	The squared modulus of the electric fields (a) $ E_{tx-012} ^2$ and (b) $ E_{tz-012} ^2$ transmitted at the prism-gold interface as a function of the angle of incidence θ_1	31
2.9	The squared modulus of the electric fields (a) $ E_{ix-0123} ^2$ and (b) $ E_{iz-0123} ^2$ incident at the gold-sample interface as a function of the angle of incidence θ_1	33
2.10	The squared modulus of the exponential phase factor $ \exp(j\beta_2) ^2$ as a function of the angle of incidence θ_1	34
2.11	Plots of (a) the transmission coefficient $ t_{23} ^2$ and (b) the power transmittance $ T_{23} ^2$ at the gold-sample interface as a function of the angle of incidence θ_1	36
2.12	The squared modulus of the electric fields (a) $ E_{tx-0123} ^2$ and (b) $ E_{tz-0123} ^2$ transmitted at the gold-sample interface as a function of the angle of incidence θ_1	37

LIST OF FIGURES (Continued)

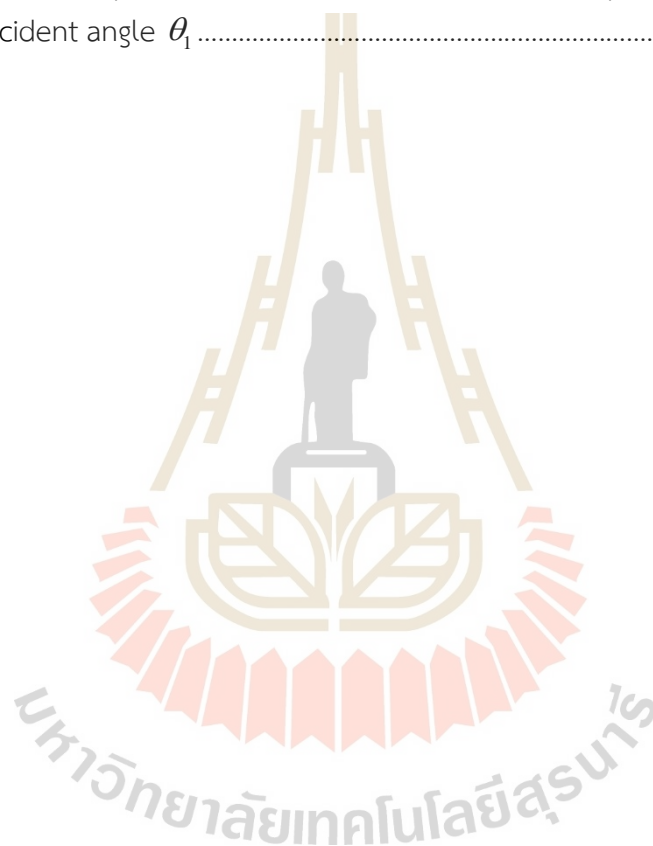
Figure	Page
2.13	The squared modulus of the reflection coefficient R_{23} at the gold-sample-gold interface as a function of the angle of incidence θ_1 39
2.14	The squared modulus of the electric fields (a) $ E_{rx-321} ^2$ and (b) $ E_{rz-321} ^2$ reflected at the sample-gold interface. 41
2.15	The squared modulus of the electric fields (a) $ E_{ix-321} ^2$ and (b) $ E_{iz-321} ^2$ incident at the gold-prism interface. 43
2.16	The total reflectance from the sample into the prism $R = r_{321} ^2$ as a function of the angle of incidence θ_1 44
2.17	The squared modulus of the electric fields (a) $ E_{rx-321} ^2$ and (b) $ E_{rz-321} ^2$ reflected from the gold-prism interface..... 46
2.18	Variation of the transmission coefficient t_{10} for the prism-air interface as a function of the angle of incidence θ_1 47
2.19	The squared modulus of the electric fields (a) $ E_{rx-3210} ^2$ and (b) $ E_{rz-3210} ^2$ transmitted at the prism-air interface. 49
2.20	The squared modulus of the total electric fields $ E_{r-3210} ^2$ detected by the sensor. 50
3.1	Schematic illustration of the divergent illumination based SPR sensor setup using Powell lens..... 52
3.2	A schematic diagram of the 6-layers of the SPR sensor. 56
3.3	Total reflectance power $R_{654321} = r_{654321} ^2$ as a function of the angle of incidence θ_1 for without glass and with the glass thickness of 1 mm and 1 μm 58
3.4	The occurrence of the interference fringes between two consecutive rays 60
3.5	Comparison of the fringe spacings calculated by using the total reflectivity of the 6-layer setup given by Eq. (3.11) and the derived formula of Eq. (3.29) and as a function of the incident angle θ_1 62
4.1	Beam profiles transmitted from (a) the laser source, (b) the cylindrical lens and (c) the Powell lens, respectively. 63

LIST OF FIGURES (Continued)

Figure		Page
4.2	The corresponding normalized beam intensities obtained from the source, the cylindrical lens, and the Powell lens.....	64
4.3	Experimental setup for implementing the divergent illumination-based SPR sensor using Powell lens.....	66
4.4	(a) SPR reflectivity pattern of air and water and (b) its corresponding normalized reflectivity averaged along the vertical direction.....	66
4.5	(a) SPR reflectivity pattern of air and ethanol and (b) its corresponding normalized reflectivity averaged along the vertical direction.....	68
4.6	Detected SPR positions as a function of the refractive index of the test samples.....	69
4.7	Total reflectance power $R_{654321} = r_{654321} ^2$ as a function of the angle of incidence θ_1 for the 80 μm ML and the air gaps.....	72
4.8	Total reflectance power as a function of the angle of incidence for the non-uniform 80 μm ML and the air gaps.....	73
4.9	The SPR reflectivity patterns obtained by using the (a) S- (b) P-polarized lights.....	74
4.10	Effects of the 80 μm uniform ML gap on the SPR reflectivity patterns obtained by using the (a) S- (b) P-polarized lights.....	74
4.11	Effects of the 80 μm non-uniform ML gap on the SPR reflectivity patterns obtained by using the (a) S- (b) P-polarized lights.....	76
4.12	The SPR reflectivity patterns obtained by using the p-polarized light with air gap (a) $d_2 = 0 \mu\text{m}$ (b) uniform $d_2 = 80 \mu\text{m}$ and (c) non-uniform $d_2 = 0 - 80 \mu\text{m}$	76
4.13	Normalized SPR reflectivity signals obtained by using the p-polarized light with and without gaps of the ML and air as a function of the angle of incidence θ_1 for (a) Normal ML and no air gap noted by black and grey (b) uniform ML and air gap $d_2 = 80 \mu\text{m}$ noted by pink and blue (c) Non-uniform ML and air gap d_2 maximum = 80 μm denoted by green and red.....	78

LIST OF FIGURES (Continued)

Figure		Page
4.14	Enlarged SPR reflectivity signal of the 1-mm glass plate without gap shown in Fig. 4.13 as the function of the incident angle.....	79
4.15	Plots of the experimental and the theoretical fringe spacings as the function of the incident angle θ_1	80

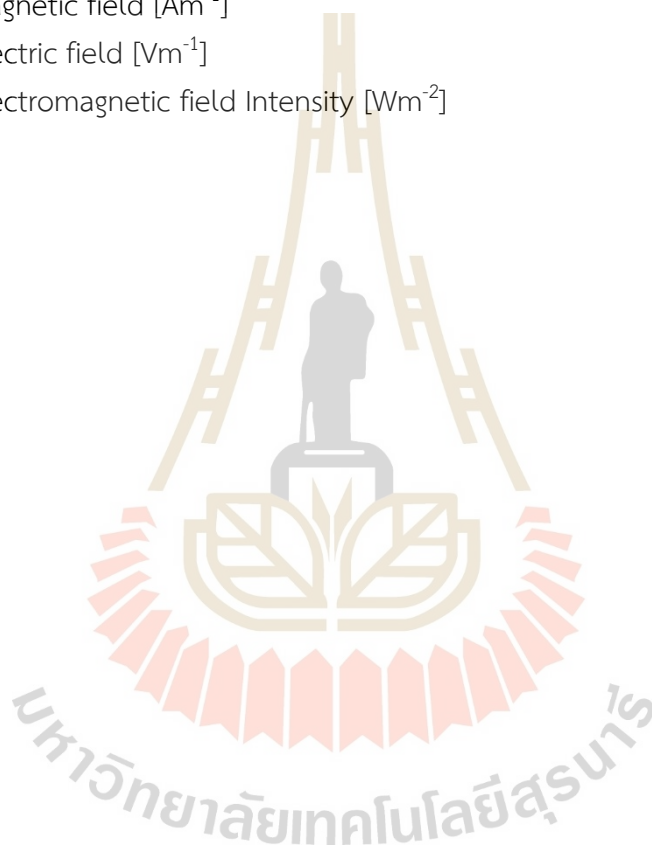


SYMBOLS AND ABBREVIATIONS

AB	=	Prism dimensions [m].
BC	=	Prism dimensions [m].
CA	=	Prism dimensions [m].
AE	=	Entrance position of the ray DE [m].
AG	=	Reflectance position of the light ray EG [m].
AH	=	Reflectance position of the light ray FH [m].
BI	=	Exit position of the light ray HI [m].
DE	=	Upper peripheral ray [m].
EG	=	Upper peripheral rays [m].
GJ	=	Upper peripheral ray [m].
JN	=	Upper peripheral ray [m].
DF	=	Lower peripheral ray [m].
FH	=	Lower peripheral ray [m].
HI	=	Lower peripheral ray [m].
IM	=	Lower peripheral ray [m].
DL	=	Normal distance from a prism surface to a focal point of Powell lens [m]
EF	=	Beam widths [m].
GH	=	Beam widths [m].
IJ	=	Beam widths [m].
MN	=	Beam widths [m].
GH	=	Sensing widths [m]
α	=	Base angle (°)
α_i	=	Incident angle of upper-peripheral ray (°)
α_t	=	Transmitted angle of upper-peripheral light ray (°)
β_i	=	Incident angle of lower-peripheral light ray (°)
β_{spr}	=	Resonance angle (°)
γ	=	Detection angle (°)
ϕ	=	Apex angle (°)
ξ	=	Illumination angle (°)
β_t	=	Transmitted angle of lower-peripheral light ray (°)
θ	=	Fan angle of Powell lens
ML	=	Matching liquid (°)

SYMBOLS AND ABBREVIATIONS (Continued)

- SPR* = Surface plasmon resonance
RIU = Refractive index unit
RI = Refractive index
TM = Transverse magnetic field
 λ = Wavelength [m]
H = Magnetic field [Am^{-1}]
E = Electric field [Vm^{-1}]
I = Electromagnetic field Intensity [Wm^{-2}]



CHAPTER I

INTRODUCTION

1.1 Literature review

Surface plasmon oscillations are oscillations of electron charge density confined to the boundary of a metal and dielectric material (Kretschmann and Raether 1968, Otto 1968). Owing to the displacements of the electrons relative to positive ions, surface plasmons form longitudinal waves with a certain frequency and wave vector. Surface plasmons can be excited by using monochromatic P-polarized light because the tangential component of its electric field is parallel to the longitudinal wave of the surface plasmons. When the wave vector of the incident photon is the same as that of the surface plasmons, photon energy is absorbed by free electrons on the metal surface, resonating surface plasmons. To match the two wave vectors, the light beam is shone through a prism placed in contact with the other side of the metal layer. By adjusting the angle of incidence of the photon at the prism-metal interface to be greater than the critical angle, the wave vector of an evanescent wave generated could be matched to that of the plasmons, yielding photon energy absorption by the free electrons. Hence, the reflected photon energy diminishes drastically to almost zero (Homola, Vaisocherová et al. 2005). The angle of incidence that gives the minimum reflectivity is called the resonance angle. The prism coupling configuration was first introduced by Otto (Otto 1968) and Kretschmann (Kretschmann and Raether 1968). Therefore, SPR-based sensors that employ the minimum dip reflectivity detection could be used to monitor changes in the refractive index of a dielectric medium adjacent to the metal layer. This SPR sensing method is called the angular interrogation method.

The angular interrogation-based SPR sensors have been widely applied to the fields of health sciences, such as monitoring environmental pollution, food safety, and disease diagnostic testing. In environmental science, micro-living organisms in soil are known to provide useful micronutrients for agricultural purposes. However, the lives of the microorganisms are easily affected by the salinity concentration of water. In

order to monitor the salinity concentration, the use of a graphene oxide-based SPR sensor has been reported by Raikwar et al. (Raikwar, Prajapati et al. 2020). In the report, the graphene oxide is sandwiched between the gold layer and the sample. The reason for this interest is that graphene oxide is permeable to water but not its impurities, such as salts and bacteria. The graphene oxide has a higher surface area and conductivity than graphene, which could enhance its sensing sensitivity by 3.3 times better than that of the graphene-based SPR sensor (Raikwar, Prajapati et al. 2020)

SENSIA, S.L. (Spain) developed a two-channel SPR sensor to detect six types of pesticides, such as DDT, chlorpyrifos, and carbaryl. The first three samples are placed on one of the channels, while the others are on the other channel. Thus, the two SPR channels can measure six pesticide samples simultaneously (Mauriz, Calle et al. 2007). The developed SPR could perform real-time monitoring onsite by letting the water being tested flow through a flow cell. This method has a faster detection time than the conventional method, which requires six sensing channels.

Furthermore, detection of microplastics' presence in water is also important for protecting the existence of living microorganisms. Unlike traditional methods, which can only detect micromolar-order microplastic concentrations, a SPR sensor can detect molar concentrations on the nano scale. (Huang, Narasimha et al. 2021).

In food safety monitoring, a prism-based SPR sensor was first reported for detecting a low level of adulteration in the pure of honey (Zainuddin, Fen et al. 2018). The study showed that when adulteration occurs, its corresponding resonance angle becomes lower than that of pure honey. This is because its refractive index is lower than pure honey. Besides being able to detect salmonella bacteria in milk in real time, detection (Mazumdar, Hartmann et al. 2007). SPR sensors have been found to be useful for precisely measuring metal ions in drinking water (Forzani, Zhang et al. 2005). In these applications, high specificity of the bacteria and metal ions is achieved by immobilizing the gold sensor chips with c18 hydrophobic and short peptides, respectively.

Recently, detection of severe acute respiratory syndrome coronavirus (SARS-CoV-2) using prism-based SPR sensors has been studied (Basso, Malossi et al. 2021, Moznuzzaman, Khan et al. 2021). The sensor chip made of TiO₂-Ag-MoSe₂ graphene was immobilized using CR3022 antigen and S-glycoprotein as an antibody. The

developed SPR sensor outperformed other single and multilayered SPR sensors in terms of sensitivity ($194^\circ/\text{RIU}$), quality factor (54.0390 RIU^{-1}), and detection accuracy (0.2702). The SPR-based detection of SARS-CoV-2 using thiol-tethered DNA as a ligand has been proposed for sensing samples taken from human nasopharyngeal swabs (Uddin, Chowdhury et al. 2021). Besides having 7.6 times better sensitivity than a conventional Kretschmann configuration SPR sensor, the proposed SPR sensor has a faster detection response compared with a reverse transcriptase quantitative polymerase chain reaction (RT-qPCR).

In an angular interrogation-based SPR sensor, the reflectivity varies with respect to the angle of incidence. Therefore, according to how the angle of incidence is scanned, the angular interrogation can be implemented by using three types of scanning mechanisms: mechanical, converging, and diverging beam scanning. In a comparison with the spectral interrogation method, which requires a polychromatic light source and a spectrometer (Homola, Vaisocherová et al. 2005), the angular interrogation is cheaper and simpler. Thus, it is widely used for biosensors.

The mechanical beam scanning mechanism involves either rotational or translational movement of the illumination part or the sensing part, which includes the prism and the gold sensor chip, and the detection part, which consists of a small size photodiode by means of a single or double prism. The single prism configuration is based on the $\theta/2\theta$ goniometer geometry, with the sensing part rotated by an angle θ . The rotation angle of a photodetector is set to θ (Kretschmann 1972, Gordon and Swalen 1977, Gwon and Lee 2010, Liang, Miranto et al. 2010, Daniyal, Fen et al. 2019, Saleviter, Fen et al. 2020). Thus, two stepper motors are needed to rotate the two parts of the system. The rotational of the sensing could increase a span of the dynamic measurement range of the sample's refractive index. Thus, to enhance SPR angular resolution, the optical moving part of the SPR sensor must be manufactured at a high level of precision and accuracy. Consequently, an overall SPR sensor system will be heavy, bulky, expensive and have high electric power consumption. Spin-off company Sensia S.L. (Zagorodko, Bouckaert et al. 2015), Sensby Biotech Co. Ltd (Ltd.), SPR NAVI (Life Sciences), Bio-rad (Bio-Rad), and NanoSPR Devices (Nanospr) are a few examples of

manufacturers who make SPR sensors that work with this technique. Model and specifications of their instruments are shown in **Table 1.1**.

The double prism configuration was introduced to replace the expensive goniometer by using two right-angle prisms, which are equal in dimension, and a fixed photodetector. The first prism coupled directly with the laser source serves as the sensing part, with the gold sensor chip attached to its hypotenuse. The second prism placed between the first prism and a photodetector maintains that the beam incident on the photodetector always has the same angle (Mohanty and Kasiviswanathan 2005, Boruah, Mohanta et al. 2015). To achieve the same incident angle, the apex of the first prism is aligned with the vertex of the second prism in such a way that the two surfaces form a particular separation angle. When the beam reflected by the boundary of the prism-sensor layer enters the entrance surface of the second prism, it will be reflected by the hypotenuse. By satisfying the required separation angle, the beam is normally transmitted from the exit surface of the second prism. However, it is hard to ensure that the exit light is always incident on the fixed point over a wide dynamic angular range. Owing to deployment of the two prisms, the intensity of the detected beam on the photodetector decreases. Hence, its sensitivity is reduced as well (Devanarayanan, Manjuladevi et al. 2016).

Since relative motions of solid surfaces of optical components cause friction, the mechanical scanning causes laser intensity fluctuations, thermal drifts, and mechanical noises (Tao, Boussaad et al. 1999). Furthermore, the step size and the speed of the stepper motor determine the angular resolution of about $0.1 \sim 0.002^\circ$ and the sensing response time of several minutes. In addition, the mechanical scanning-based SPR requires the use of an expensive lock-in amplifier to remove noise buried in the signal at nanovolt scales (Devanarayanan, Manjuladevi et al. 2016). For the preceding reasons, the mechanical scanning based SPR is unsuitable for multichannel sensing (Matsubara, Kawata et al. 1988, O'Brien II, Pérez-Luna et al. 2001, Palumbo, Pearson et al. 2003, Hong, Kim et al. 2007, Hossain and Rana 2016).

In order to solve the problems of mechanical beam scanning using stepper motors, the direction of the illuminating beam is changed by vibrating a mirror (Kooyman, Lenferink et al. 1991, Lenferink, Kooyman et al. 1991, Kausaite, van Dijk et

al. 2007) , which can be driven by either a coil or piezo motor. Vibrating the mirror by a coil deflects the angle of the incidence on the sensing chip, increasing the range of the refractive index measurements and improving the SPR sensor's time response. When the mirror is deflected at a particular angle, the reflected laser beam will be incident on the prism and shine on the prism-gold interface. The incident position of the laser beam on the interface is determined by the mirror's deflecting angle. Consequently, when the beam width is small, two adjacent incident beams will be spatially separated. This spatial separation is called the displacement between two adjacent incident beams. As a result, the bigger the displacement, the lower the measured refractive index resolution (Kooyman, Lenferink et al. 1991). The beam displacement on the interface can be eliminated, provided that the incident beam width is not a small spot. Therefore, to solve the beam displacement error, an expanded parallel beam is used as the illuminating beam. In order to have the same size of the beam width on the interface, a cylindrical lens placed between the mirror and the prism is employed to generate the image of the illuminating beam with a unity magnification, eliminating the displacement error (Lenferink, Kooyman et al. 1991). Among the manufacturer that make SPR sensors, which operate vibration mirrors, are Metrohm Autolab B.V. (Autolab) and IBIS Technologies (Technologies). For further details regarding the technical specifications of the SPR instruments which works under this mechanism, see **Table 1.1**.

Using convergent beam illumination is an alternative method for implementing angular interrogation without the problems associated with mechanical scanning (Matsubara, Kawata et al. 1988, O'Brien II, Pérez-Luna et al. 2001, Palumbo, Pearson et al. 2003, Hong, Kim et al. 2007, Lokate, Beusink et al. 2007, Shin, Kim et al. 2010, Zhang, Liu et al. 2017). According to this optical implementation setup, an expanded laser beam is focused on the sensing area, yielding a micrometer-order spot area. Since the incident beam is a focused beam, light rays confined by a cone-shaped beam strike the sensing gold chip at different angles. The reflected beam is detected by a CCD/CMOS array sensor. The focused beam's angular scan range depends on the ratio of the expanded beam size and the focal length of the focusing lens (Hickel and Knoll 1991). The higher the ratio, the larger the angular scan. The reflected beam is then

recollimated by another lens and detected by an array of sensors. Consequently, the divergent-beam illumination based SPR sensors have a bulky system. Examples of companies that manufacture SPR sensors that operate using convergent beam scanning include Plasmatrix (Plasmatrix 2022, June, 27) and Biacore AB system (Liang, Gan et al. 2018). Some of the instrument models and specifications that use this technique are shown in **Table 1.1**.

The measurable range of the resonance angles could be increased by using a rotating mirror (Hong, Kim et al. 2007, Lokate, Beusink et al. 2007, Beusink, Lokate et al. 2008, Shin, Kim et al. 2010, Geng, Zhang et al. 2012, Nguyen, Yi et al. 2016), an acoustic-optical deflector (AOD) (VanWiggeren, Bynum et al. 2007) and a galvo scanner (Zeng, Zhou et al. 2019). However, this SPR sensor setup becomes costly, bulky, and consumes more electricity for operating an RF oscillator and stepper motor. Hence, it is unsuitable for offsite sensing. Bruker is only company that produces SPR sensor which works under acoustic-optical deflector principle as has been shown in **Table 1.1** (Bruker).

Unlike the mechanical and the converging beam scanning, the implementation of the angular-based SPR setups using divergent beam illumination offers high-sensitivity and high-throughput sensors (Chinowsky, Quinn et al. 2003). The coherent divergent beam could be optically generated by using either a light-emitting diode (Chinowsky, Quinn et al. 2003), a cylindrical lens (Chan and Jutamulia 2012), or a laser diode (Isaacs and Abdulhalim 2015). In contrast to the convergent beam illumination, the divergent beam, which has an inverted cone shape, is spatially incident on a wide sensing area of the sensors. This type of illumination may be employed to facilitate the implementation of multichannel SPR sensing (Wang, Loo et al. 2018). Thus, each light ray has its own particular angle of incidence. Despite having the capability of producing divergent beams, the cylindrical lens, the light-emitting diode, and the laser diode provide inherently a Gaussian beam, which has photon energy distributions in the shape of a two-dimensional bell curve. As a result, besides being hard to identify whether the observed minimum dip intensity is a result of either the beam shape or the plasmon resonance phenomena, its corresponding dark band appears as a curved line. The curved dark band may broaden the SPR reflectance signal. Consequently, it

requires an advanced mathematical transformation to extract the SPR dip (Karabchevsky, Karabchevsky et al. 2011). The non-uniform energy distribution becomes more severe in the case of multichannel sensing. Apart from the non-uniform beam distribution, the three conventional methods have a narrow divergence or fan angle. This is another factor that will limit the number of multichannel sensing. Table 1 lists some of the SPR sensors that operate under diverging beam scanning (Photonicsys, Chinowsky, Quinn et al. 2003)

In order to solve the above drawbacks, the use of a Powell lens that could produce a divergent beam with uniform intensity distribution across a wide fan angle (Powell 1989) has been reported in the implementation of the SPR sensor (Chen, Wang et al. 2015). However, the report did not describe the rigorously necessary conditions for optimizing the beam illumination and detection for SPR sensing. Our previous theoretical study addressed these important issues by using geometrical optics analysis (Hossea and Widjaja 2020). Our study found that there are three important aspects in the optimization of the beam illumination and detection. The first aspect is the determination of the fan and the illumination angles of the divergent beam for a given refractive index to be measured. The second one is the alignment of an array light detector with respect to the reflected output beam. The third one is the mathematical relation between the spatial position along the sensor plane and the resonance angle. The final one is the effects of the prism types and materials on the beam parameters.

Table 1.1. Commercially available SPR sensors operates under angular interrogation principles

No	Angular interrogation	Manufacturer	Instrument model	Angular resolution (°)	Resolution (RIU)	RI Range (RI)	Prism (RI)	λ (nm)
1	Mechanical scanning	Sensia S.L.	Indicator	-		-	1.569	650
		Sensby Biotech Co. Ltd.	SPR-T200, SPR-T210, SPR-I300	0.02, 0.01, 0.001	3×10^{-6}	1.33 – 1.4	1.845	632.8
			SPR NAVI.	SPR NAVI 220A	-	1×10^{-6}	1 - 1.45	-
		Bio-Rad.	ProteOn XPR36	-	1×10^{-6}	1.33-1.37	-	-
		NanoSPR Devices	NanoSPR-77	-	5×10^{-6}	1.0 – 1.15/ 1.3 – 1.46	-	650
2	Convergent beam scanning	Plasmetrix	CORGI 11F Cubic/ CORGI cubic	-	1×10^{-6}	1.33 - 1.36	1.598	650
		Biacore AB	BIACore T200 system	-	1×10^{-7}	1.33 - 1.39	1.515	632.8
3	Mirror-based convergent beam scanning	Metrohm Autolab B.V	Autlab Twingle/Springle	0.02m	1×10^{-6}	1.26-1.38 1.32-1.44 1.40-1.52	-	670 -
		IBIS Technologies	IBIS-MX96	-	3×10^{-6}	-	1.518	840
4	AOD-based convergent beam scanning	Bruker	Sierra SPR-32 Pro		1.8×10^{-6}	1.33 - 1.38	1.7	780/830
5	Divergent-beam scanning	Texas Instrument	SPREETA 2000	-	1×10^{-6}	1.33- 1.37	-	830
		PhotonicsSys	SPR00 H5	-	1×10^{-5}	1.3-1.42	1.778	632
					-	1×10^{-6}	1- 1.4	1.778

1.2 Significance of the study

Despite the promising features offered by the Powell lens-based divergent beam scanning, the developed theory of the divergent beam illumination and the detection conditions has never been experimentally validated. The advantage of using Powell lens to generate the divergent beam is that it not only efficiently transfers uniform photon energy to a large sensing area but also simplifies the detection algorithm of the SPR dip intensity. Therefore, the first aim of this thesis work is to validate experimentally the developed theory by measuring simultaneously a broad refractive index variation of 1.0003 ~ 1.3580.

Furthermore, the uniform intensity of the wide divergent beam produced by the Powell lens signifies the application of the SPR to multichannel sensing, where a large dynamic range of SPR measurement is vital for monitoring biomolecule interactions (Geng, Zhang et al. 2012). In this application, different samples are spatially distributed across either a large or a partitioned sensing area. Instead of taking sequentially multiple measurements of samples having different refractive indices, a parallel measurement of different samples could be done in a single-shot acquisition. However, the large sensing area requires a large the gold sensor chip. Due to the large size requirement, placing the chip on top of the prism may easily introduce a misalignment gap and violate the illumination condition, hampering the sensor performance (Sharma, Jha et al. 2010). Therefore, the second aim of this thesis is to conduct a theoretical study of the effects of the misalignment gap on the SPR reflectivity signals by applying boundary conditions for TM wave propagation across different layer interfaces.

1.3 Problem statement

i. To solve the problems of conventional angular interrogations in surface plasmon resonance (SPR) sensors, the implementation of the SPR sensors using divergent beam illumination has been experimentally verified.

ii. The effects of using a wide sensing plate in the SPR sensor based on the divergent beam illumination on the resonance reflectivity are theoretically studied by means of the boundary conditions for the TM wave propagation across different layer interfaces.

1.4 Research procedure

- i. To verify experimentally the developed divergent-beam illumination and detection conditions in the SPR sensor using Powell lens.
- ii. To measure experimentally the refractive indices of the air–water sample and the air–ethanol sample in a single-shot acquisition.
- iii. To derive the analytical formulas for the propagation of the TM wavefields in the 5-layer SPR sensor.
- iv. To study the effects of the misalignment gap on the SPR reflectivity signal by calculating the TM fields across different layer interfaces with Matlab software.

1.5 Scope of the study

- i. To verify experimentally the developed divergent-beam illumination and detection conditions in the SPR sensor using Powell lens.
- ii. The diverging beam is generated by using the Powell lens (Thorlabs, PL0160).
- iii. The experimental verifications are done to measure the wide dynamic range of the refractive indices from air to water and air to ethanol.
- iv. A gold-evaporated glass chip (NanoSPR, BA1000) is used as a sensor chip.
- v. Refractive indices matching liquid (Cargille, series A) are used to reduce light loss through the prism.
- vi. A SPR reflectivity pattern is detected by using a CMOS sensor (Sony, Exmor R IMX251).
- vii. The TM wavefields in each layer of the SPR sensor are mathematically derived by the boundary conditions for the wave propagation in the multi-layer medium.
- viii. The effects of the misalignment gap of the gold-evaporated glass chip on the SPR reflectivity signal are theoretically studied using computer simulations.

1.6 Expected result

- i. We experimentally verified the conditions of the divergent-beam illumination and detection in the SPR sensor.

- ii. Experimentally verified single-shot acquisition of the wide-range variation of refractive indices using the divergent beam-based SPR sensor.
- iii. Improved knowledge of the effects of the misalignment gap of the gold-evaporated glass chip on the SPR reflectivity signal.

1.7 Organization of the thesis

There are five chapters in this research. The following subtopics are covered in **Chapter I** literature review, study importance, problem statement, research technique, study scope, and expected findings. The general theory and derivation of evanescent wave, surface plasmon resonance and the propagation of TM waves in 3-layers SPR-prism based Kretschmann configuration are described in the **Chapter II**. **Chapter III** mathematical modelling of the experimental setup and derivation of the fringe spacing. Experimental verification and results are presented and discussed in **Chapter IV**, and lastly conclusion of the research work and recommendations of future work are presented in **Chapter V**.



CHAPTER II GENERAL THEORY

2.1 General theory of surface plasmon resonance

2.1.1 Evanescent wave

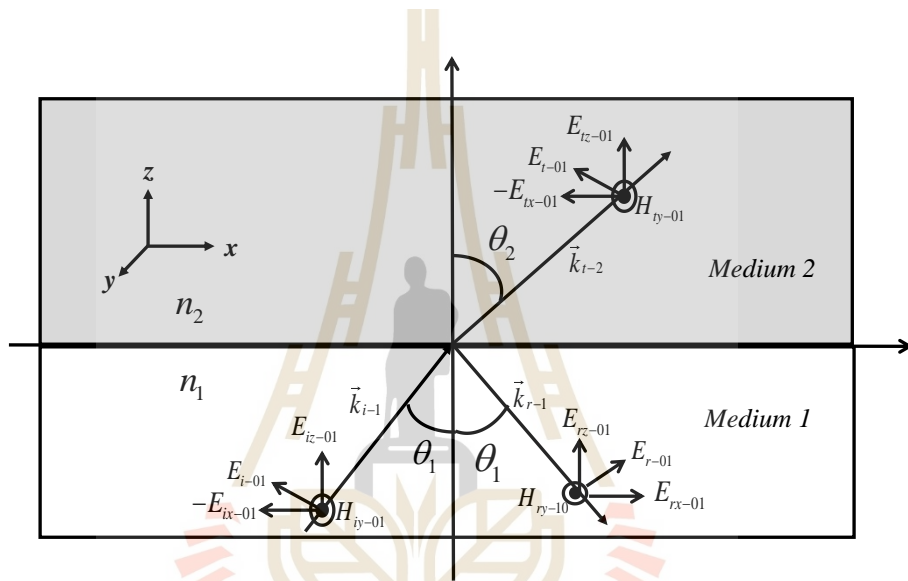


Figure 2.1. A schematic diagram of a TM beam propagation at the boundary of two-layer media.

Figure 2.1 illustrates a schematic diagram of an oblique illumination of the TM wave with a wavelength λ at the interface of two media with refractive indices $n_1 > n_2$. The plane of incidence is parallel to the x - z plane of the figure. \vec{k}_i , \vec{k}_r , and \vec{k}_t correspond to the wave vectors of the incident, the reflected, and the transmitted wave propagations, respectively. θ_1 and θ_2 represents the angles of the incidence and the transmission of the waves, respectively.

The electric field of the incident light wave can be mathematically expressed as

$$\vec{E}_{i-01}(x, z) = E_{i-01} \left(-\vec{a}_x \cos \theta_1 + \vec{a}_z \sin \theta_1 \right) \exp \left[-j\vec{k}_{i-1} \left(x \sin \theta_1 + z \cos \theta_1 \right) \right], \quad (2.1)$$

where E_{i-01} is the amplitude of the incident electric field. The corresponding magnetic field is given by

$$\vec{H}_{i-01}(x, z) = \left(\vec{a}_y E_{i-01} / Z_1 \right) \exp \left[-j \vec{k}_{i-1} (x \sin \theta_1 + z \cos \theta_1) \right] \quad (2.2)$$

The fields transmitted into the medium 2 can be written

$$\vec{E}_{t-01}(x, z) = E_{t-01} \left(-\vec{a}_x \cos \theta_2 + \vec{a}_z \sin \theta_2 \right) \exp \left[-j \vec{k}_{t-2} (x \sin \theta_2 + z \cos \theta_2) \right], \quad (2.3)$$

and

$$\vec{H}_{t-01}(x, z) = \left(\vec{a}_y E_{t-01} / Z_2 \right) \exp \left[-j \vec{k}_{t-2} (x \sin \theta_2 + z \cos \theta_2) \right], \quad (2.4)$$

respectively. Here, Z_1 and Z_2 are the wave impedances of the media 1 and 2, respectively. The amplitude of the transmitted electric field E_{t-01} is equal to $t_{12} E_{i-01}$ with t_{12} is the transmission coefficient at the interface between medium 1 and medium 2.

Furthermore, the two transmitted fields can be rewritten in terms of the incident angle θ_1 by using Snell's law

$$\sin \theta_2 = (n_1 / n_2) \sin \theta_1 \quad (2.5)$$

and

$$\cos \theta_2 = \pm \sqrt{1 - \left((n_1 / n_2) \sin \theta_1 \right)^2}. \quad (2.6)$$

Substitutions of Eqs. (2.5) and (2.6) into (2.3) and (2.4) give the fields as

$$\begin{aligned} \vec{E}_{t-01}(x, z) = & \left(-E_{tx-01} \vec{a}_x + E_{tz-01} \vec{a}_z \right) \exp \left[-j(2\pi/\lambda) n_1 (x \sin \theta_1) \right] \\ & \times \exp \left[-j(2\pi/\lambda) n_2 \left(z \sqrt{1 - \left((n_1/n_2) \sin \theta_1 \right)^2} \right) \right] \end{aligned} \quad (2.7)$$

$$\begin{aligned} \vec{H}_{t-01}(x, z) = & \left(\vec{a}_y E_{t-01} / Z_2 \right) \exp \left[-j(2\pi/\lambda) n_1 (x \sin \theta_1) \right] \\ & \times \exp \left[-j(2\pi/\lambda) n_2 \left(z \sqrt{1 - \left((n_1/n_2) \sin \theta_1 \right)^2} \right) \right] \end{aligned} \quad (2.8)$$

With $E_{tx-01} = E_{t-01} \cos \theta_2$ and $E_{tz-01} = E_{t-01} \sin \theta_2$.

When the incident angle is greater than the critical angle, Eq. (2.6) has imaginary roots

$$\cos \theta_2 = \pm j \sqrt{\left((n_1/n_2) \sin \theta_1 \right)^2 - 1} \quad (2.9)$$

Consequently, by substituting Eq. (2.9) into Eqs. (2.7) and (2.8) can be rewritten as

$$\begin{aligned} \vec{E}_{t-01}(x, z) = & \left(-E_{tx-01} \vec{a}_x + E_{tz-01} \vec{a}_z \right) \exp \left[-j(2\pi/\lambda) n_1 (x \sin \theta_1) \right] \\ & \times \exp \left[-(2\pi/\lambda) n_2 \left(z \sqrt{\left((n_1/n_2) \sin \theta_1 \right)^2 - 1} \right) \right] \end{aligned} \quad (2.10)$$

and

$$\begin{aligned} \vec{H}_{t-01}(x, z) = & \left(\vec{a}_y E_{t-01} / Z_2 \right) \exp \left[-j(2\pi/\lambda) n_1 (x \sin \theta_1) \right] \\ & \times \exp \left[-(2\pi/\lambda) n_2 \left(z \sqrt{\left((n_1/n_2) \sin \theta_1 \right)^2 - 1} \right) \right] \end{aligned} \quad (2.11)$$

Therefore, Eqs. (2.10) and (2.11) are the mathematical expressions of the electric and magnetic field for the evanescent wave. The negative sign is chosen

because it is impossible to have an increasing field as the propagation distance z increases.

2.1.2 Surface plasmon resonance

This section considers that medium 1 is a prism, while medium 2 is a gold layer with a refractive index n_g . The generated evanescent wave propagates along the interface of the two media. The resonance condition of the surface plasmon is analyzed as follows. Consider that the wavevector of the incident field at the dielectric-gold interface is given by

$$\vec{k}_{i-1} = n_1 \omega c = \frac{n_1 2\pi}{\lambda}. \quad (2.12)$$

Since the surface plasmon wave oscillates longitudinally at the interface, the tangential components of the incident and transmitted wave vectors at each layer are the same

$$\vec{k}_{i-1} \sin \theta_1 = \vec{k}_{t-2} \sin \theta_2, \quad (2.13)$$

in which \vec{k}_{t-2} is the transmitted wavevector at the gold layer. Substitution of Eq. (2.12) into Eq. (2.13) gives the horizontal component of the evanescent wavevector (Otto 1968)

$$k_{ev-x} = \frac{2\pi}{\lambda} n_1 \sin \theta_1. \quad (2.14)$$

According to Otto (Otto 1968), the evanescent wave momentum is written as

$$p_{eva} = \hbar k_{ev-x}. \quad (2.15)$$

The photon energy carried by the evanescent wave can be obtained by substituting Eq. (2.14) into Eq. (2.15)

$$p_{eva} = \frac{n_1 h}{\lambda} \sin \theta_1. \quad (2.16)$$

When a dielectric sample with a refractive index n_s is placed on top of the gold layer, the oscillation of the surface charges on the gold layer gives the surface plasmon wave vector k_{sp} , can be expressed as (Otto 1968)

$$k_{sp} = \frac{2\pi}{\lambda} \sqrt{\frac{n_g^2 n_s^2}{n_g^2 + n_s^2}}. \quad (2.17)$$

The momentum of the surface plasmon resonance wave can be expressed as follows

$$p_{sp} = \frac{h}{\lambda} \sqrt{\frac{n_g^2 n_s^2}{n_g^2 + n_s^2}}. \quad (2.18)$$

Thus, when the two momenta match, the surface plasmon wave resonates with the photon wave, causing a maximum absorption of the photon energy (Otto 1968). The matching condition can be expressed as

$$p_{eva} = p_{sp}. \quad (2.19)$$

Therefore, substituting Eq. (4.17) and Eq. (4.18) into Eq. (4.19), gives

$$\frac{n_1 h}{\lambda} \sin \theta_1 = \frac{2\pi}{\lambda} \sqrt{\frac{n_g^2 n_s^2}{n_g^2 + n_s^2}} \quad (2.20)$$

This implies that the photon energy is coupled by electrons within the gold film. At this state of resonance, the reflectivity spectrum showed minimum reflectivity, which corresponds to the resonance angle and can be mathematically expressed as (Otto 1968)

$$\theta_{sp} = \sin^{-1} \left[\frac{1}{n_1} \sqrt{\frac{n_g^2 n_s^2}{n_g^2 + n_s^2}} \right] \quad (2.21)$$

2.2 Transmittance and reflectance in multilayer media

One of the objectives of this study is to investigate the misalignment effects of the gold sensor chip on the SPR reflectance signals. In order to study how transmissions and reflections of the electric fields in each SPR layer are affected by the misalignment gap, power transmittance and the reflectance of the layers will be employed, because light power is determined by photon energy. The transmittance and the reflectance can be described by applying the boundary conditions for TM wave propagation across different interfaces separating different media as shown in **Fig. 2.1**. During the propagation across two different media with the refractive indices of n_1 and n_2 , the electric field E_{i-01} is reflected and refracted. Assume that the field E_{i-01} incident at the angle θ_i on the boundary of the two media has the beam width w_i , while the electric field E_{t-01} refracted at the angle of refraction of θ_t into the medium 2 has the beam width w_t . According to Snells' law of reflection, the electric field E_{r-01} reflected off the boundary at the angle of reflection $\theta_r = \theta_i$ has the beam width $w_r = w_i$. At the beam intersection position on the interface between the two media, the electric fields E_{i-01} and E_{r-01} have the same beam width of $w_i / \cos \theta_i$, which is equal to the width $w_t / \cos \theta_t$. The incident, the reflected and the transmitted beam intensities can be

expressed as $I_i = n_1 \varepsilon_0 c |E_{i-01}|^2 / 2$, $I_r = n_1 \varepsilon_0 c |E_{r-01}|^2 / 2$ and $I_t = n_2 \varepsilon_0 c |E_{t-01}|^2 / 2$, respectively. The boundary conditions give

$$-E_{i-01} \cos \theta_i + E_{r-01} \cos \theta_r = -E_{t-01} \cos \theta_t \quad (2.22)$$

and

$$H_{iy-01} + H_{ry-01} = H_{ty-01} \quad (2.23)$$

Equations (2.22) and (2.23) can be solved by expressing the electric fields in terms of the magnetic fields. The amplitude ratios $r = H_{r-01}/H_{i-01}$ and $t = H_{t-01}/H_{i-01}$ given by

$$t = \frac{2n_2 \cos \theta_i}{n_2 \cos \theta_i + n_1 \cos \theta_t} \quad (2.24)$$

and

$$r = \frac{n_2 \cos \theta_i - n_1 \cos \theta_t}{n_2 \cos \theta_i + n_1 \cos \theta_t} \quad (2.25)$$

are known as the reflection and the transmission coefficients, respectively. They are sometimes referred to as Fresnel's equations (Ohta and Ishida 1990). It can be understood that the two coefficients disregard the beam area changes at the boundary of the two media, which determines light power. Therefore, the effectiveness of materials in transmitting and reflecting photon energy must be described by using their power transmittance and reflectance.

Applying the energy conservation principle to light propagation, the transmittance and reflectance can be derived.

$$P_i = P_r + P_t, \quad (2.26)$$

where P_i , P_r and P_t denote the incident, reflected and transmitted optical powers, respectively. By expressing mathematically, the optical power as the product of the intensity and the beam area, the three corresponding intensities can be expressed in

terms of the electric field as $I_i = n_1 \epsilon_0 c |E_{i-01}|^2 / 2$, $I_r = n_1 \epsilon_0 c |E_{r-01}|^2 / 2$ and $I_t = n_2 \epsilon_0 c |E_{t-01}|^2 / 2$. Therefore, Eq. (2.26) can be expressed as

$$n_1 \epsilon_0 c |E_{i-01}|^2 A_i / 2 = n_1 \epsilon_0 c |E_{r-01}|^2 A_r / 2 + n_2 \epsilon_0 c |E_{t-01}|^2 A_t / 2, \quad (2.27)$$

where A_i , A_r , and A_t represent the beam areas of the incident, reflected and transmitted beams at the intersection position. Division of the two terms on the right hand side by the power of the incident beam followed by expressing the beam area by the beam width results in

$$1 = r^2 + \left(n_2 \cos \theta_t / n_1 \cos \theta_i \right) t^2 \quad (2.28)$$

In Eq. (2.28), the first term on the right-hand side is known as the power reflectance $R = r^2$, while the second term defines the power transmittance $T = \left(n_2 \cos \theta_t / n_1 \cos \theta_i \right) t^2$. As a result, Eq. (2.28) can be rewritten as

$$R + T = 1. \quad (2.29)$$

Unlike the transmission coefficient, it is apparent that the power transmittance is dependent upon the refractive index of the medium and the angle of the beam propagation.

2.3 Propagation of TM waves in Kretschmann prism configuration

Although the preceding section describes the relationship between the resonance angle and the refractive indices of the prism, the gold layer, and the sample, the classical SPR theory does not provide information about the effect of the misalignment gap on the SPR reflectivity curve that is important to the present study. In this section, the SPR reflectivity curve is studied by taking into account the power transmittance and reflectance together with the metal layer thickness. To gain a better understanding, the following discussion assumes that the equilateral prism ($n_p = 1.785$)

is illuminated by p-polarized light with an operating wavelength of $\lambda = 632.8$ nm. The sensing chip is the gold layer ($n_g = 0.1726 + j3.4218$) with a thickness of d_2 .

Figure 2.2 illustrates a schematic diagram of a three-layer structure of the SPR optical sensor based on the Kretschmann prism configuration. The plane of incidence is parallel to the x-z plane of the setup. In order to resonate the surface plasmon, the TM wave with a wavelength λ is shined upon the prism-gold-sample sandwich structure at an angle θ_1 , which is higher than the critical angle of the prism. The incident beam at the air-prism interface has the angle of incidence of θ_0 . This angle can be expressed in terms of the angle of incidence θ_1 at the prism-gold interface and the prism angle α as

$$\begin{aligned}\theta_0 &= \arcsin(n_p \sin \theta_1) \\ &= \arcsin[n_p \sin(\alpha - \theta_1)].\end{aligned}\quad (2.30)$$

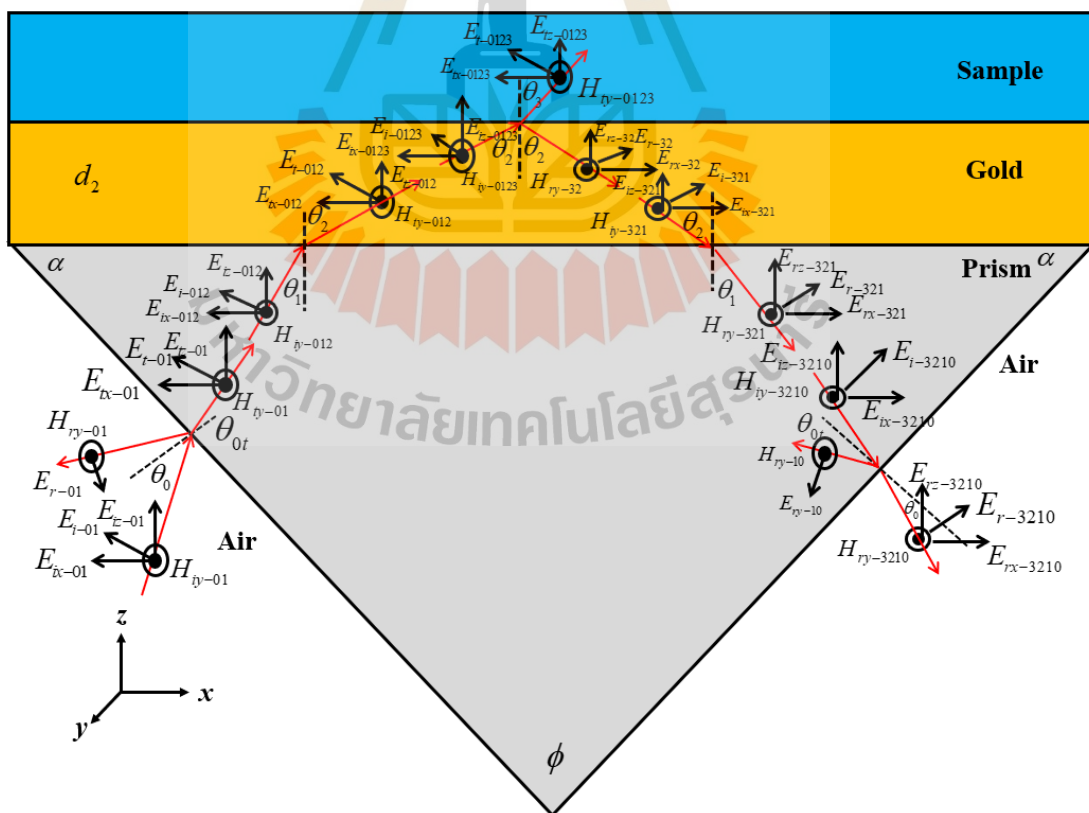


Figure 2.2. Vector wavefields of the incident, the transmitted and the reflected TM wave in the Kretschmann-based equilateral prism configuration.

Fig. 2.3 shows a plot of the incident angle θ_0 as a function of the angle θ_1 calculated by using Eq. (2.30a). They have an inverse relationship such that the bigger the angle of incidence at the prism-gold interface the smaller the incident angle at the air-prism interface. When the angle θ_1 is equal to the prism angle $\alpha = 60^\circ$, the illuminating light is incident normally at the air-prism interface, causing $\theta_0 = 0^\circ$

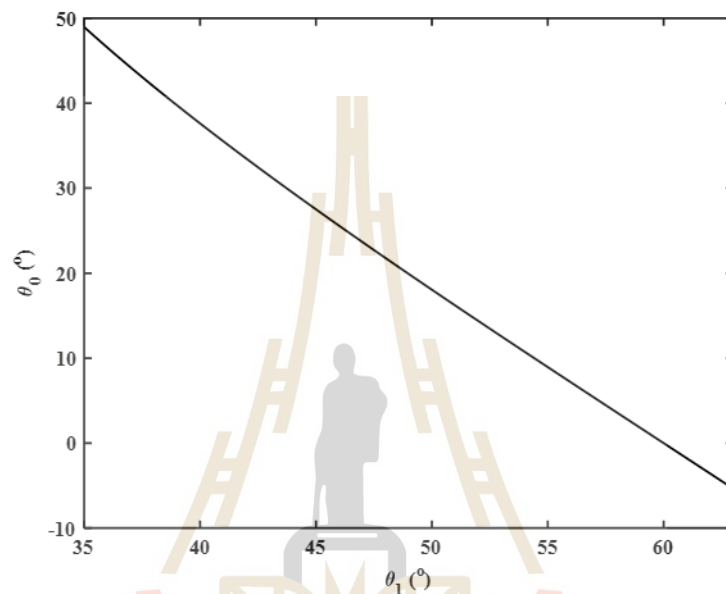


Figure 2.3. Plot of the angle of incidence θ_0 for the air-prism interface as a function of the angle of incidence θ_1 for the prism-gold interface

2.3.1 Electric field incident on the prism

Let us consider that the incident TM wave on the air-prism interface has a unit amplitude magnetic field H_{iy-01}

$$H_{iy-01} = 1. \quad (2.31)$$

The corresponding incident electric field is calculated by multiplying the magnetic field and the wave impedance of free space Z_0 that is approximately equal to 120π (Olsen and Rouseff 1985)

$$E_{i-01} = 120\pi H_{iy-01}. \quad (2.32)$$

The amplitudes of the incident electric field components E_{ix-01} and E_{iz-01} can be mathematically expressed as

$$E_{ix-01} = (120\pi \cos \theta_0) H_{iy-01} \quad (2.33a)$$

and

$$E_{iz-01} = (120\pi \sin \theta_0) H_{iy-01}, \quad (2.33b)$$

respectively. **Figs. 2.4(a)** and **2.4(b)** show plots of the two incident electric field components, $|E_{ix-01}|^2$ and $|E_{iz-01}|^2$, as a function of the angle θ_0 . They are calculated by using Eqs (2.33a) and (2.33b) respectively. Unlike the constant magnetic field, the x- and z-components of the electric field are highly dependent on the angle of incidence θ_0 . The electric field in x -component is maximum, when the angle of incidence is 0° or the illuminating light wave is incident normally on the prism surface. Its amplitude decreases as the angle of incidence becomes larger. Meanwhile, the z-component of the electric field varies inversely proportional to the x-component such that the z-component becomes zero when the x-component is at its maximum.

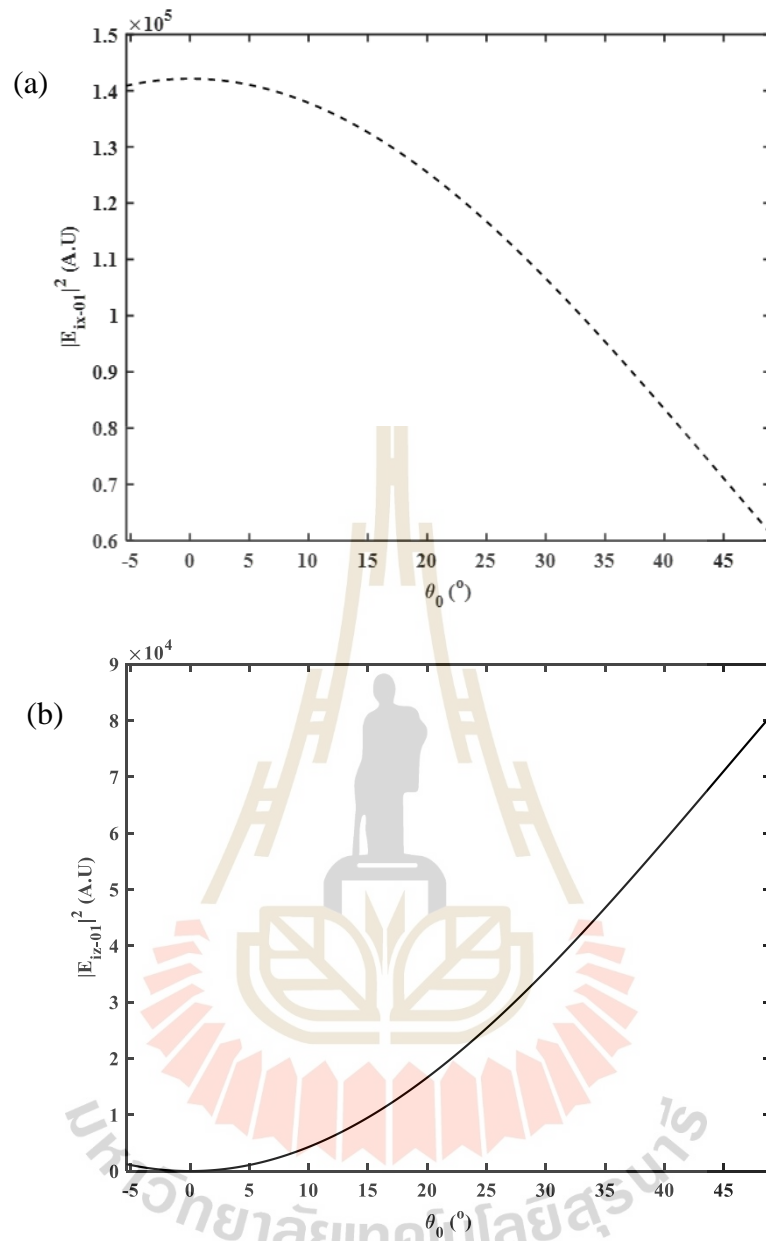


Figure 2.4. The squared modulus of the electric field components (a) $|E_{ix-01}|^2$ and (b) $|E_{iz-01}|^2$ incident on the air-prism interface.

2.3.2 Electric field transmitted at the air-prism interface

The transmitted magnetic field can be simply calculated as $H_{ty-01} = t_{01} H_{iy-01}$, where t_{01} is the transmission coefficient for the air-prism interface. For the unit-amplitude H_{iy-01} , the transmitted magnetic field H_{ty-01} is solely determined by the transmission coefficient t_{01} at the air-prism interface. By applying the boundary

condition for the oblique incidence of the wave at the plane boundary, the fields are equal to

$$-E_{t-01} \cos \theta_0 + E_{r-10} \cos \theta_0 = -E_{t-01} \cos \theta_{0r} \quad (2.34a)$$

and

$$H_{iy-01} + H_{ry-10} = H_{ty-01}. \quad (2.34b)$$

By expressing the electric fields in terms of the magnetic fields and solving Eqs. (2.34a) and (2.34b), the transmission coefficient is found to be equal to

$$t_{01}^H = \left(\frac{2n_p \cos \theta_0}{n_p \cos \theta_0 + n_0 \cos \theta_{0r}} \right), \quad (2.35a)$$

where θ_{0r} is the transmitted angle of the wave field into the prism given by $\theta_{0r} = \alpha - \theta_1$. Furthermore, solving Eqs. (2.34a) and (2.34b) in terms of the electric fields gives the conventional transmission coefficient given by

$$t_{01}^E = \left(\frac{2n_0 \cos \theta_0}{n_p \cos \theta_0 + n_0 \cos \theta_{0r}} \right). \quad (2.35b)$$

Fig. 2.5 shows the variation of the both transmission coefficients of t_{01}^H and t_{01}^E as a function of the incident angle θ_1 . Both the transmission t_{01}^H and t_{01}^E increases as the angle θ_1 becomes bigger. It reaches maximum at the angle $\theta_1 = 60^\circ$, which corresponds to the normal incident angle at the air-prism interface. The transmission coefficient t_{01}^H is greater than t_{01}^E because of the effect of the wave impedance.

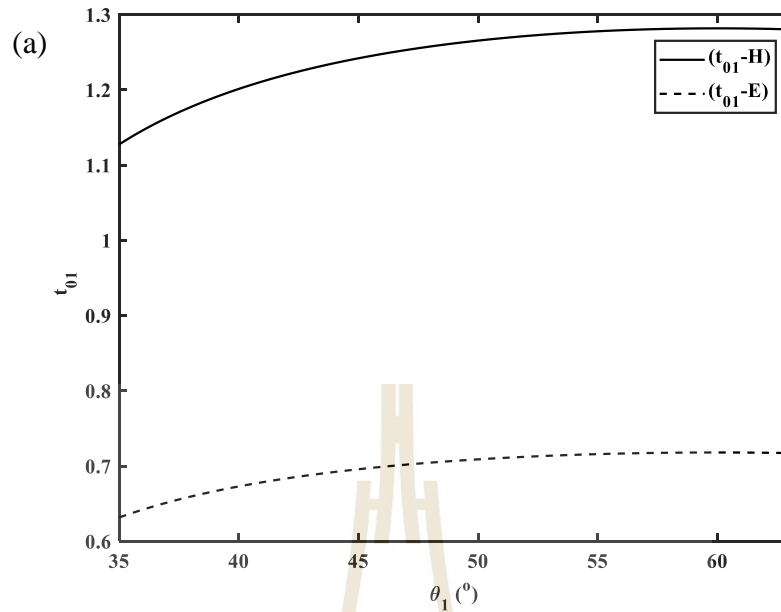


Figure 2.5 Variation of the transmission coefficients t_{01}^H and t_{01}^E as a function of the angle of incidence θ_1 for the prism-gold interface.

The boundary condition for the air-prism interface gives

$$-E_{i-01} \cos \theta_0 + E_{t-10} \cos \theta_0 = -E_{t-01} \cos \theta_{0t} \quad (2.36a)$$

and

$$H_{iy-01} + H_{ty-10} = H_{ty-01} \quad (2.36b)$$

The corresponding transmitted electric field E_{t-01} is the product of the wave impedance of the prism Z_p and the transmitted magnetic field H_{ty-01}

$$\begin{aligned} E_{t-01} &= Z_p H_{ty-01} \\ E_{t-01} &= (120\pi/n_p) H_{ty-01} \end{aligned} \quad (2.37)$$

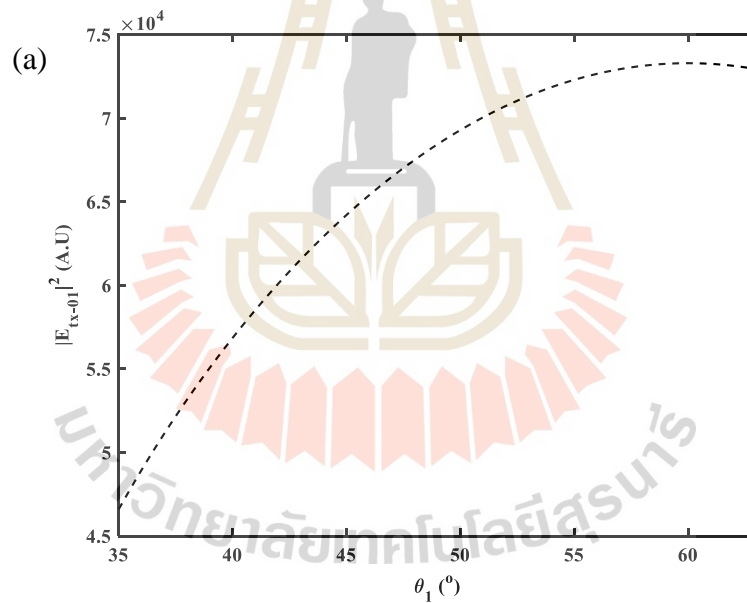
The horizontal and vertical components of the transmitted electric field, E_{tx-01} and E_{tz-01} , can be written as

$$E_{tx-01} = \left[(120\pi/n_p) \cos \theta_{0r} \right] H_{ty-01} \quad (2.38a)$$

and

$$E_{tz-01} = \left[(120\pi/n_p) \sin \theta_{0r} \right] H_{ty-01}, \quad (2.38b)$$

respectively. Plots of the square modulus of the two electric components given by Eqs. (2.38a) and (2.38b) as a function of the incident angle at the prism-gold interface θ_1 is shown in **Fig. 2.6**. Their variations can be explained by considering the relationship $\theta_{0r} = \alpha - \theta_1$, which indicates that the transmitted angle at the air-prism interface θ_{0r} will become smaller, when the incident angle θ_1 increases. As the term $\cos \theta_{0r}$ in Eq. (2.38a) increases, the transmitted electric field E_{tx-01} becomes higher. In contrast, the decrease in the term $\sin \theta_{0r}$ in Eq. (2.38b) reduce the field E_{tx-01} .



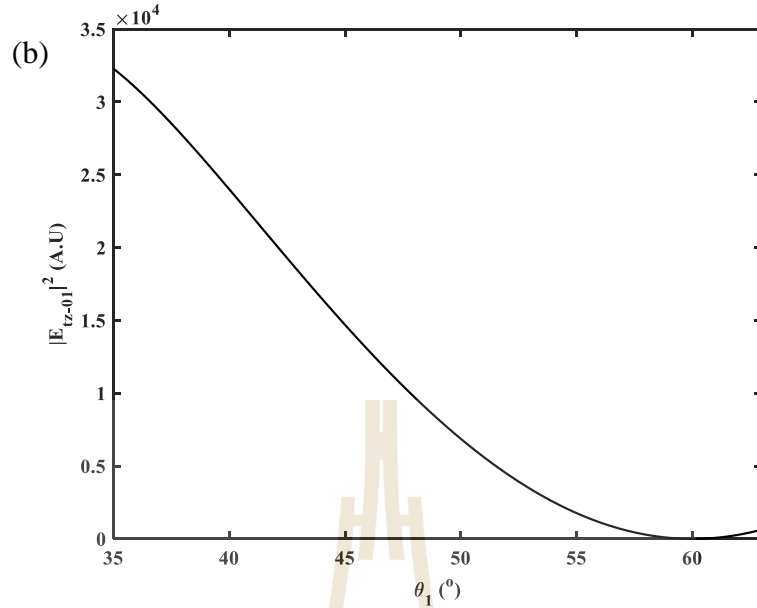


Figure 2.6. The squared modulus of the electric fields (a) $|E_{tx-01}|^2$ and (b) $|E_{tz-01}|^2$ as a function of the angle of incidence θ_1 for the prism-gold interface.

2.3.3 Electric field incident at the prism-gold interface

The magnetic field incident at the prism-gold interface H_{iy-012} is given by the transmitted field H_{ty-01} modulated by the phase shift factor $\exp(j\beta_1)$ due to the propagation within the prism. Here, $\beta_1 = (2\pi/\lambda)d_1 n_p \cos \theta_1$ and d_1 is the separation distance from the air-prism interface to prism-gold interface. The electric field incident at the prism-gold interface can be obtained by taking the prism wave impedance Z_p into account that is $E_{i-012} = Z_p H_{iy-012} = (120\pi/n_p) H_{ty-01} \exp(j\beta_1) = (120\pi/n_p) H_{ty-01} \exp(j\beta_1)$. Therefore, the electric components become

$$\begin{aligned} E_{ix-012} &= \left[(120\pi/n_p) \cos \theta_1 \right] H_{iy-012} \\ &= (120\pi/n_p) \cos \theta_1 \exp(j\beta_1) H_{ty-01} \end{aligned} \quad (2.39a)$$

and

$$\begin{aligned} E_{iz-012} &= \left[(120\pi/n_p) \sin \theta_1 \right] H_{iy-012} \\ &= (120\pi/n_p) \sin \theta_1 \exp(j\beta_1) H_{ty-01} \end{aligned} \quad (2.39b)$$

Figures 2.7(a) and 2.7(b) show the components of the electric fields E_{ix-012} and E_{iz-012} , plotted using Eqs. (2.39a) and (2.39b) respectively. The square modulus of the electric field E_{ix-012} decreases as the incidence angle θ_1 at the prism-gold interface increases. This is because the cosine term decreases as the angle θ_1 becomes larger. On other hand, the sine term in Eq. (2.39b) causes the increase of the field E_{iz-012} .

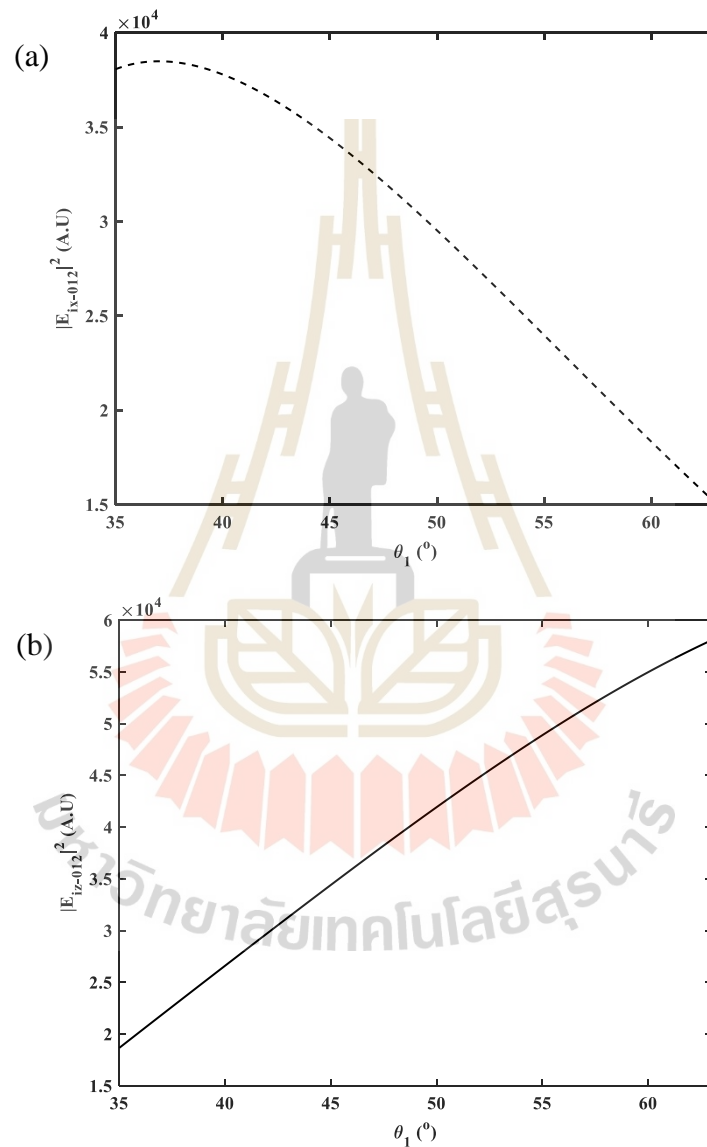


Figure 2.7. The squared modulus of the electric fields (a) $|E_{ix-012}|^2$ and (b) $|E_{iz-012}|^2$ as a function of the angle of incidence θ_1 for the prism-gold interface.

2.3.4 Electric field transmitted at the prism-gold interface

On the basis of the boundary condition for the prism-gold interface, the electric and the magnetic fields can be expressed as

$$-E_{i-012} \cos \theta_1 + E_{r-321} \cos \theta_1 = -E_{t-012} \cos \theta_2 + E_{i-321} \cos \theta_2 \quad (2.40a)$$

and

$$H_{iy-012} + H_{ry-321} = H_{ty-012} + H_{iy-321} \quad (2.40b)$$

In the above equations, E_{r-321} and H_{ry-321} denote the total reflected electric and magnetic fields originated from the gold-sample interface. The transmitted magnetic field in the gold layer is

$$H_{ty-012} = H_{iy-012} \left[\left(\frac{q_1 + q_2}{2q_2} \right) - r_{321} \left(\frac{q_1 - q_2}{2q_2} \right) \right], \quad (2.41)$$

where r_{321} represents the general expression of the total reflection coefficient from the sample to the gold layer (Shalabney and Abdulhalim 2010)

$$r_{321} = \frac{(m_{11} + q_3 m_{12}) q_1 - (m_{21} + q_3 m_{22})}{(m_{11} + q_3 m_{12}) q_1 + (m_{21} + q_3 m_{22})} \quad (2.42)$$

with m_{11} , m_{12} , m_{21} and m_{22} are the elements of the transfer matrix M , which is given as (Shalabney and Abdulhalim 2010)

$$M = \begin{bmatrix} \cos \beta_2 & -i \frac{1}{q_2} \sin \beta_2 \\ -jq_2 \sin \beta_2 & \cos \beta_2 \end{bmatrix} = \begin{bmatrix} m_{11} & m_{12} \\ m_{21} & m_{22} \end{bmatrix}. \quad (2.43)$$

Here, β_2 denotes the phase shift suffered by the light wave passing through the gold layer with a thickness of d_2 given by

$$\beta_2 = \frac{2\pi d_2}{\lambda} (n_g^2 - n_p^2 \sin^2 \theta_1)^{\frac{1}{2}}. \quad (2.44)$$

The factors q_2 and q_3 correspond to the wave impedances of the gold and the sample along the x-axis are defined as (Shalabney and Abdulhalim 2010)

$$q_2 = Z_g \cos \theta_2 \quad (2.45a)$$

and

$$q_3 = Z_s \cos \theta_3. \quad (2.45b)$$

The transmitted electric field at the prism-gold interface can be obtained as the product of the wave impedance of the gold layer Z_g and the transmitted magnetic field H_{ty-012} , that is $E_{t-012} = Z_g H_{ty-012}$. Thus, resolving the transmitted electric field into the x- and the z- directions gives

$$\begin{aligned} E_{tx-012} &= \cos \theta_2 E_{t-012} = \cos \theta_2 Z_g H_{ty-012} \\ &= \left\{ \left[n_g^2 - (n_p \sin \theta_1)^2 \right]^{\frac{1}{2}} / n_g \right\} (120\pi / n_g) H_{ty-012} \\ &= \left[(n_g^2 - 1) / (n_p \sin \theta_1) \right]^{\frac{1}{2}} n_p \sin \theta_1 \left[120\pi / n_g^2 \right] H_{ty-012} \end{aligned} \quad (2.46a)$$

and

$$\begin{aligned} E_{tz-012} &= \sin \theta_2 E_{t-012} = \sin \theta_1 Z_g H_{ty-012} \\ &= (n_p / n_g) \sin \theta_1 Z_g H_{ty-012} = n_p \sin \theta_1 \left[120\pi / n_g^2 \right] H_{ty-012} \end{aligned} \quad (2.46b)$$

Figure 2.8(a) and 2.8(b) show the square modulus of the two electric field components E_{tx-012} and E_{tz-012} as a function of the incident angle θ_1 . They are plotted by using Eqs. (2.46a) and (2.46b). It is obvious that the z-component of the transmitted electric field in the gold layer shown in Fig. 2.8(b) is 1 order of magnitude weaker than the electric field E_{tx-012} in Fig. 2.8(a). This can be understood by considering the fact that the gold layer is a good conductor with high attenuation loss. It is worth

mentioning that the two plots exhibit a discontinuous maximum peak at the angle $\theta_1 = 48.2^\circ$ that corresponds to the critical angle of the prism-water interface. Furthermore, when the incident angle becomes higher than the critical angle, there is a sharp attenuation of the transmitted electric field as a result of photon energy absorption by the surface plasmons of the gold layer. Note that gold has a dielectric constant with a high absorption coefficient (Mitsushio, Miyashita et al. 2006). The square modulus of the transmitted electric fields after the resonance angle is always lower than that before the resonance. This is due to the effect of multiple reflections within the three-layer system.

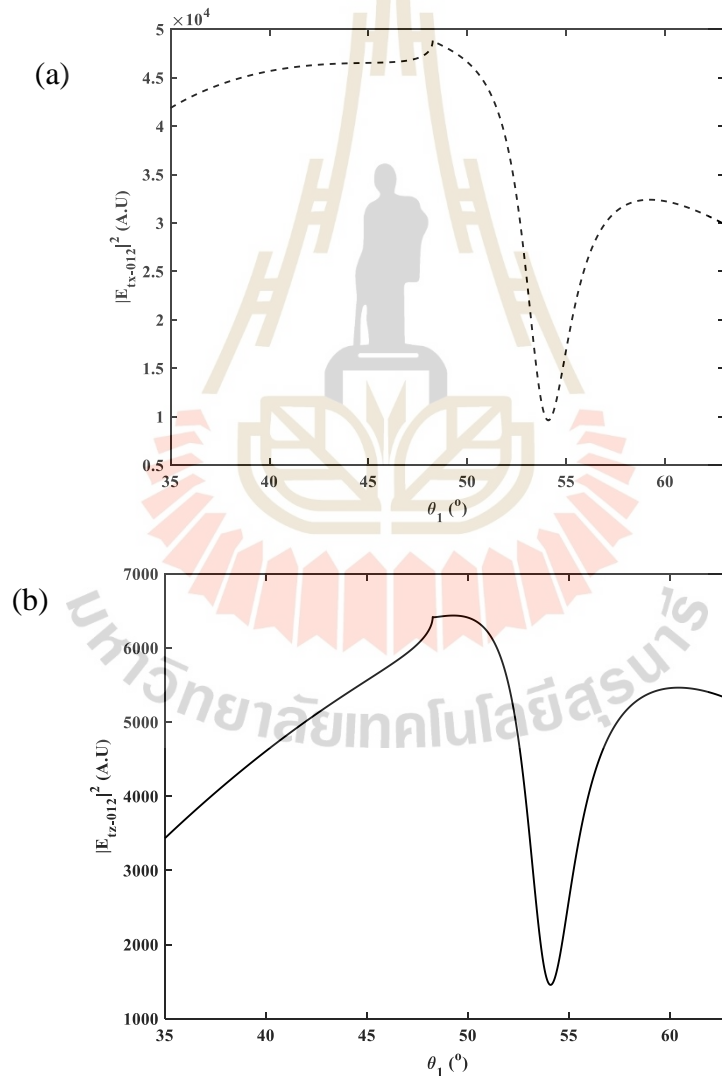


Figure 2.8. The squared modulus of the electric fields (a) $|E_{tx-012}|^2$ and (b) $|E_{tz-012}|^2$ transmitted at the prism-gold interface as a function of the angle of incidence θ_1 .

2.3.5 Electric field incident at the gold-sample interface

To determine the wavefields at the gold sample interface, the phase shift β_2 caused by the gold finite thickness is further taken into consideration. The incident magnetic field at this interface is calculated as

$$H_{iy-0123} = H_{ty-012} e^{j\beta_2}. \quad (4.47)$$

Consequently, the corresponding electric field can be expressed by using the product of the wave impedance Z_g and the magnetic field H_{iy-012} as $E_{i-0123} = Z_g H_{iy-0123} = Z_g H_{ty-012} e^{j\beta_2}$. The resolved resultant electric fields in the x- and the z - directions components give

$$\begin{aligned} E_{ix-0123} &= \cos \theta_2 Z_g \exp(j\beta_2) H_{ty-012} \\ &= \left\{ \left[n_g^2 - (n_p \sin \theta_1)^2 \right]^{\frac{1}{2}} / n_g \right\} (120\pi/n_g) \exp(j\beta_2) H_{ty-012} \\ &= \left[(n_g^2 - 1) / (n_p \sin \theta_1)^2 \right]^{\frac{1}{2}} n_p \sin \theta_1 [120\pi/n_g^2] \exp(j\beta_2) H_{ty-012} \end{aligned} \quad (2.48a)$$

and

$$\begin{aligned} E_{iz-0123} &= \sin \theta_2 Z_g \exp(j\beta_2) H_{ty-012} \\ &= (n_p/n_g) \sin \theta_1 Z_g \exp(j\beta_2) H_{ty-012} \\ &= (n_p/n_g) \sin \theta_1 (120\pi/n_g) H_{ty-012} \\ &= n_p \sin \theta_1 [120\pi/n_g^2] \exp(j\beta_2) H_{ty-012} \end{aligned} \quad (2.48b)$$

Plots of Eqs. 2.48(a) and (b) are shown in **Figs. 2.9(a)** and **2.9(b)**, respectively. It is obvious that the two incident fields decrease significantly by a maximum 96% in comparison to those of the transmitted electric fields at the prism-gold interface. A comparison of Eq. (2.47) to Eq. (2.48) shows that the difference is caused by the exponential phase factor, shown in **Fig. 2.10**, whose magnitude is smaller than one tenth and decreases as the function of the incident angle θ_1 at the prism-gold interface increases. As a result, the corresponding two components of the electric fields $E_{ix-0123}$

and $E_{iz-0123}$ change accordingly. Practically, the reduction of the electric fields is mainly caused by the inherent attenuation loss and the destructive interference caused by multiple wavefield reflections within the gold layer (Chen and Chen 1981).

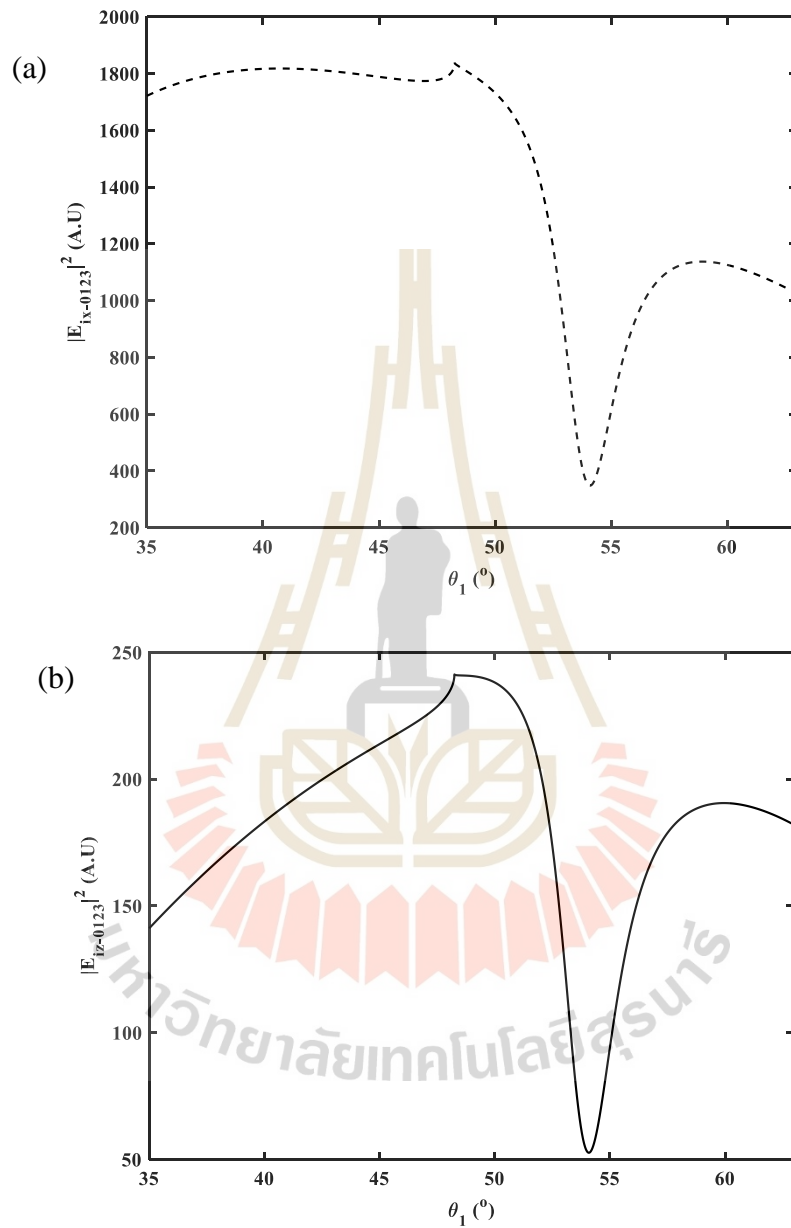


Figure 2.9. The squared modulus of the electric fields (a) $|E_{ix-0123}|^2$ and (b) $|E_{iz-0123}|^2$ incident at the gold-sample interface as a function of the angle of incidence θ_1 .

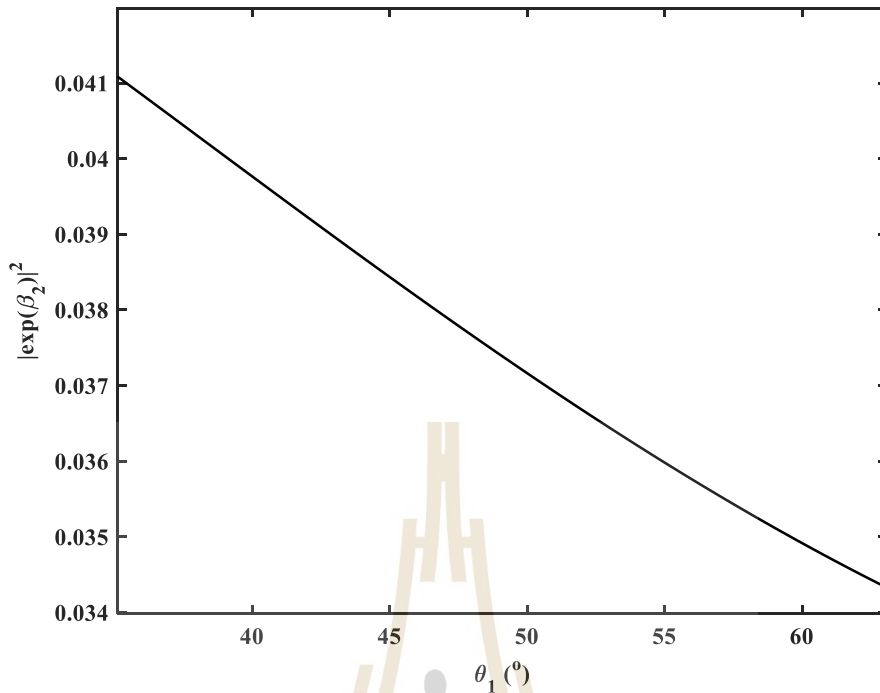


Figure 2.10. The squared modulus of the exponential phase factor $|\exp(j\beta_2)|^2$ as a function of the angle of incidence θ_1 .

2.3.6 Electric field transmitted at the gold-sample interface

The amplitude of the transmitted magnetic field $H_{ty-0123}$ is formulated by applying the boundary condition at the gold-sample interface.

$$-E_{t-012} \cos \theta_2 e^{j\beta_2} + E_{r-32} \cos \theta_2 e^{-j\beta_2} = -E_{t-0123} \cos \theta_3 \quad (2.49a)$$

and

$$H_{ty-012} e^{j\beta_2} + H_{ry-32} e^{-j\beta_2} = H_{ty-0123} \quad (2.49b)$$

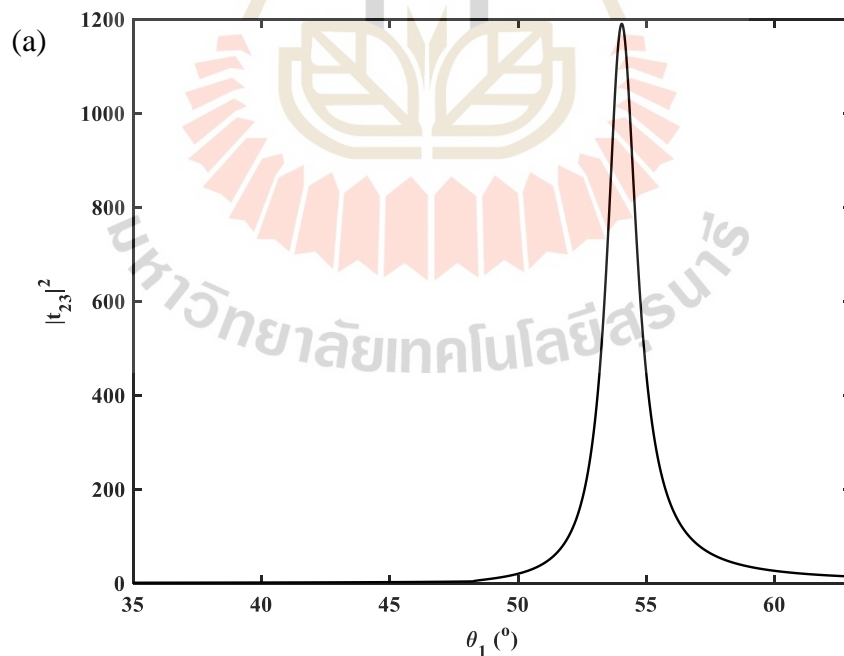
with

$$H_{ty-0123} = t_{23} H_{ty-012} \quad (2.50)$$

In Eq. (2.50), the factor t_{23} given by

$$t_{23} = \frac{2n_s^2 \left(n_g^2 - (n_p \sin \theta_1)^2 \right)^{1/2}}{n_s^2 \left(n_g^2 - (n_p \sin \theta_1)^2 \right)^{1/2} + n_g^2 \left(n_s^2 - (n_p \sin \theta_1)^2 \right)^{1/2}} \quad (2.51)$$

represents the transmission coefficient for the gold-sample interface. **Figs. 2.11(a)** and **(b)** show the square modulus of the transmission coefficient $|t_{23}|^2$ given by Eq. (2.51) and the corresponding power transmittance $|T_{23}|^2$ at the gold-sample interface plotted as a function of the angle of incidence θ_1 . The figures reveal that both the field transmission and the power transmittance have the shape of a Gaussian pulse centered at the resonance angle with a fast rise and fall. This is because, around the resonance angle, photon energy starts to be absorbed by the gold layer. The absorption of the photon energy abruptly increases when the matching conditions are satisfied at the resonance angle. The absorbed energy is then transmitted to the sample according Eq. (2.51). This highlights the optical interaction between the metal layer and the dielectric sample.



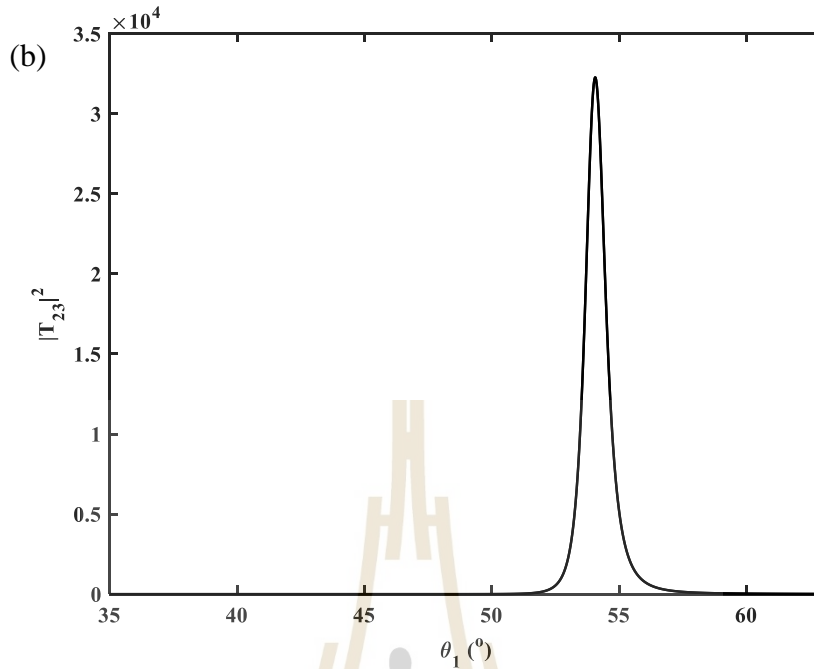


Figure 2.11. Plots of (a) the transmission coefficient $|t_{23}|^2$ and (b) the power transmittance $|T_{23}|^2$ at the gold-sample interface as a function of the angle of incidence θ_1 .

The amplitude of the transmitted electric field in the sample is found as the product of the wave impedance of the sample Z_s and the transmitted magnetic field $E_{t-0123} = Z_s H_{ty-0123}$. The two orthogonal components of the transmitted electric field can be expressed as

$$\begin{aligned}
 E_{tx-0123} &= \cos \theta_3 E_{t-0123} = \cos \theta_3 Z_s H_{ty-0123} \\
 &= \left\{ \left[n_s^2 - (n_p \sin \theta_1)^2 \right]^{\frac{1}{2}} / n_s \right\} (120\pi / n_s) H_{ty-0123} \\
 &= \left[(n_s^2 - 1) / (n_p \sin \theta_1) \right]^{\frac{1}{2}} n_p \sin \theta_1 [120\pi / n_s^2] H_{ty-0123}
 \end{aligned} \tag{2.52a}$$

and

$$\begin{aligned}
 E_{tz-0123} &= \sin \theta_3 E_{t-0123} = \sin \theta_3 Z_s H_{ty-0123} \\
 &= (n_p/n_s) \sin \theta_1 Z_s H_{ty-0123} \\
 &= n_p \sin \theta_1 [120\pi/n_s^2] H_{ty-0123}
 \end{aligned} \tag{2.52b}$$

Figures 2.12(a) and (b) show the square modulus of the transmitted electric fields, $E_{tx-0123}$ and $E_{tz-0123}$, plotted by using Eqs (2.52a) and (2.52b), respectively. Due to the power transmittance T_{23} , the transmitted electric fields become maximum at the resonance angle position.

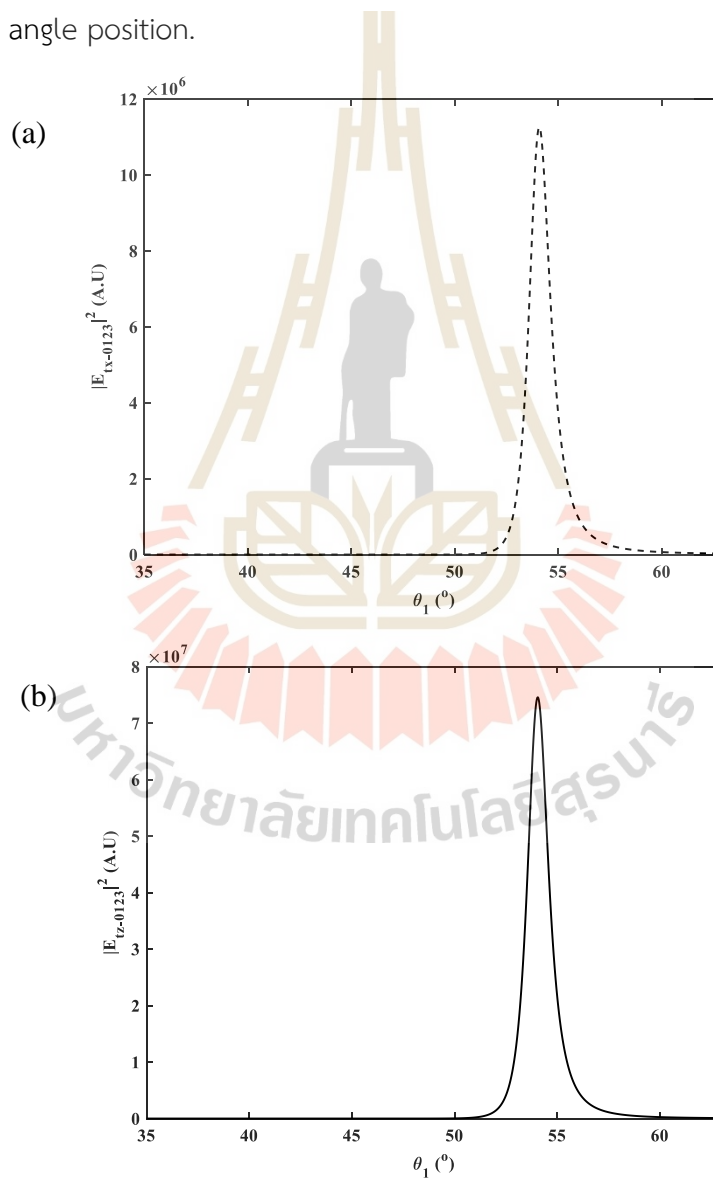


Figure 2.12. The squared modulus of the electric fields (a) $|E_{tx-0123}|^2$ and (b) $|E_{tz-0123}|^2$ transmitted at the gold-sample interface as a function of the angle of incidence θ_1 .

2.3.7 Electric field reflected from the sample-gold interface

Application of the boundary conditions at the sample-gold interface gives the following relationships:

$$-E_{r-012} \cos \theta_2 e^{j\beta_2} + E_{r-32} \cos \theta_2 = -E_{r-0123} \cos \theta_3 \quad (2.53a)$$

and

$$H_{ry-012} e^{j\beta_2} + H_{ry-32} = H_{ry-0123} \quad (2.53b)$$

The reflection coefficient given by

$$r_{23} = \frac{n_s^2 \left(n_g^2 - (n_p \sin \theta_1)^2 \right)^{1/2} - n_g^2 \left(n_s^2 - (n_p \sin \theta_1)^2 \right)^{1/2}}{n_s^2 \left(n_g^2 - (n_p \sin \theta_1)^2 \right)^{1/2} + n_g^2 \left(n_s^2 - (n_p \sin \theta_1)^2 \right)^{1/2}} \quad (2.54)$$

is obtained by solving Eqs. (2.53a) and (2.53b). This coefficient relates the magnetic field reflected from the sample-gold interface and the incident field as

$$H_{ry-32} = r_{32} H_{ry-0123} \quad (2.55)$$

Fig. (2.13) shows the square modulus of the reflectance coefficient R_{23} at the gold-sample interface plotted as a function of the angle of incidence θ_1 by using Eq. (2.54). The smaller value of the reflectance than that of the transmittance T_{23} suggests that more photonic energy will be absorbed and transmitted to the sample than the energy reflected from the sample-gold interface.

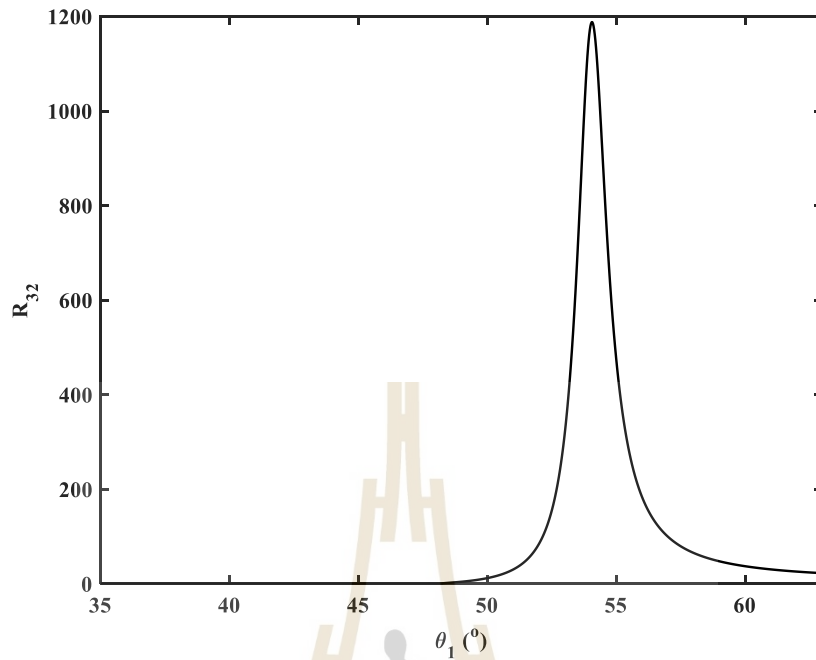


Figure 2.13. The squared modulus of the reflection coefficient R_{23} at the gold-sample-gold interface as a function of the angle of incidence θ_1 .

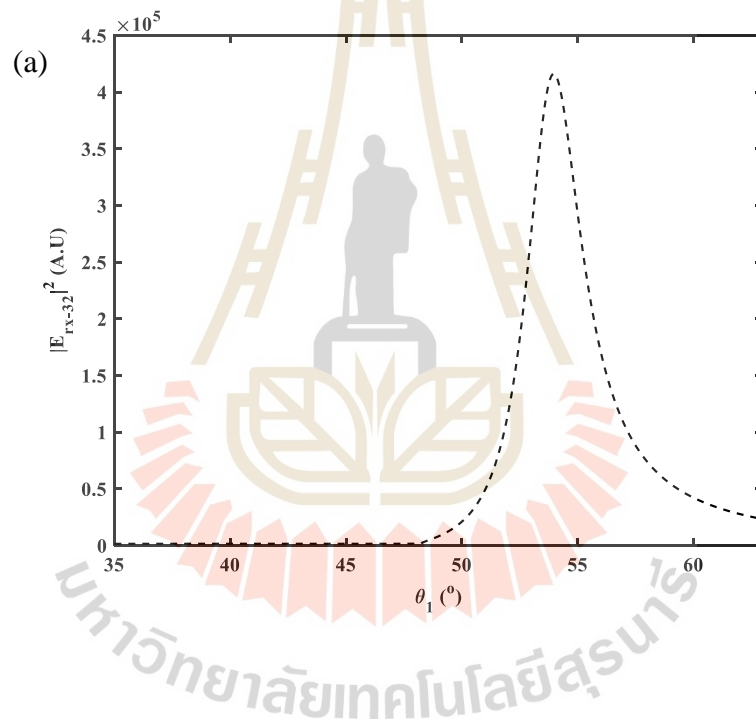
The electric field reflected back in the gold is found as the product of the wave impedance of the gold Z_g and the reflected magnetic field $E_{r-32} = Z_g H_{ry-32}$. The formula of two perpendicular components of the reflected electric field is derived as

$$\begin{aligned}
 E_{rx-32} &= \cos \theta_2 E_{r-32} = \cos \theta_2 Z_g H_{ry-32} \\
 &= \left\{ \left[n_g^2 - (n_p \sin \theta_1)^2 \right]^{\frac{1}{2}} / n_g \right\} (120\pi / n_g) H_{ry-32} \\
 &= \left[(n_g^2 - 1) / (n_p \sin \theta_1) \right]^{\frac{1}{2}} n_p \sin \theta_1 [120\pi / n_g^2] H_{ry-32}
 \end{aligned} \tag{2.56a}$$

and

$$\begin{aligned}
 E_{rz-32} &= \sin \theta_2 E_{r-32} = \sin \theta_2 Z_g H_{ry-32} \\
 &= \left(n_p / n_g \right) \sin \theta_1 Z_g H_{ry-32} \\
 &= n_p \sin \theta_1 \left[120\pi / n_g^2 \right] H_{ry-32}
 \end{aligned}
 \tag{2.56b}$$

Figs. 2.14(a) and (b) show the square modulus of the transmitted electric fields, E_{rx-32} and E_{rz-32} , plotted by using Eqs (2.56a) and (2.56b), respectively. Due to the characteristic of the reflection coefficient r_{23} , the reflected electric fields become maximum at the resonance angle position.



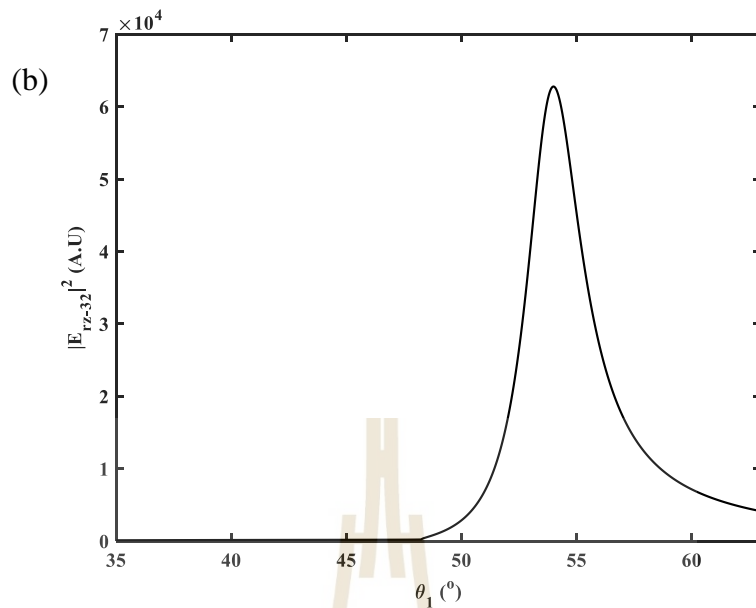


Figure 2.14. The squared modulus of the electric fields (a) $|E_{rx-32}|^2$ and (b) $|E_{rz-32}|^2$ reflected at the sample-gold interface.

Comparisons of Figs. (2.14) and (2.12) reveals that the electric field reflected back in the gold layer is smaller than that transmitted to the sample. It is worth mentioning that the tangential and the normal components of the reflected electric field are smaller by about two and three orders of magnitudes than those of the normal component of the reflected field. This confirms that the maximum absorption of the photon energy occurs due to the plasmon resonance.

2.3.8 Electric field incident at the gold-prism interface

The amplitude of the incident magnetic field H_{iy-321} at the gold-prism interface can be expressed as the product of the reflected magnetic field H_{ry-32} and the exponential function of the phase shift β_2 , which depends on the optimum thickness of the gold layer

$$H_{iy-321} = H_{ry-32} e^{j\beta_2}. \quad (2.57)$$

By expressing the corresponding electric field as the product of the gold's wave impedance Z_g and the magnetic field H_{iy-321} , $E_{i-321} = Z_g H_{iy-321} = Z_g H_{ry-32} e^{j\beta_2 z}$, the x- and the z- components of the electric field can be written as follows

$$\begin{aligned}
 E_{ix-321} &= \cos \theta_2 Z_g \exp(j\beta_2 z) H_{ry-32} \\
 &= \left\{ \left[n_g^2 - (n_p \sin \theta_1)^2 \right]^{\frac{1}{2}} / n_g \right\} (120\pi/n_g) \exp(j\beta_2 z) H_{ry-32} \quad (2.58a) \\
 &= \left[(n_g^2 - 1) / (n_p \sin \theta_1) \right]^{\frac{1}{2}} n_p \sin \theta_1 \left[120\pi/n_g^2 \right] \exp(j\beta_2 z) H_{ry-32}
 \end{aligned}$$

and

$$\begin{aligned}
 E_{iz-321} &= \sin \theta_2 Z_g \exp(j\beta_2 z) H_{ry-012} \\
 &= (n_p/n_g) \sin \theta_1 Z_g \exp(j\beta_2 z) H_{ry-32} \quad (2.58b) \\
 &= (n_p/n_g) \sin \theta_1 (120\pi/n_g) H_{ry-012} \\
 &= n_p \sin \theta_1 \left[120\pi/n_g^2 \right] \exp(j\beta_2 z) H_{ry-32}
 \end{aligned}$$

It is apparent from the plots of the two electric field components shown in **Fig. 2.15** that incident electric field components $|E_{ix-321}|^2$ and $|E_{iz-321}|^2$ at the gold-prism interface reduce by maximum 96% in comparison to the reflected electric fields $|E_{rx-32}|^2$ and $|E_{rz-32}|^2$. The attenuation loss of the metal layer and the destructive interference caused by the opposite phase shift factor are the cause of the reduction of the fields (see **Fig. 2.10**).

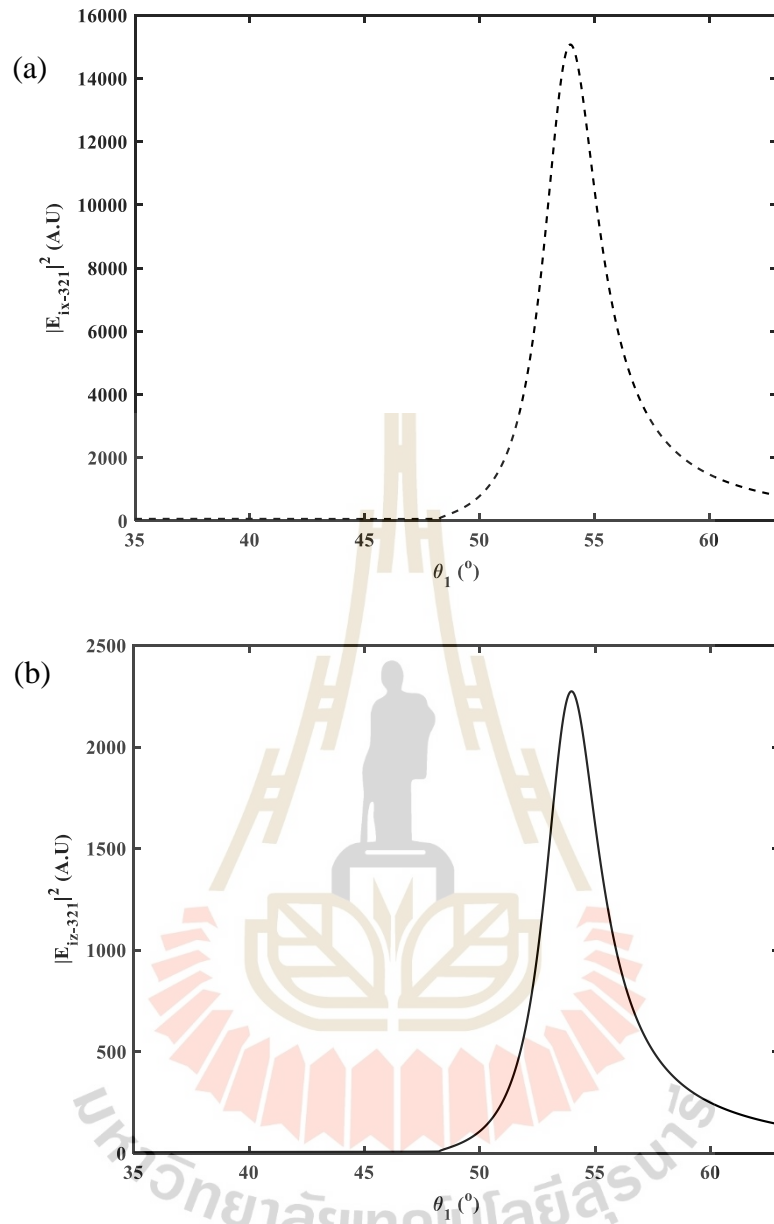


Figure 2.15. The squared modulus of the electric fields (a) $|E_{ix-321}|^2$ and (b) $|E_{iz-321}|^2$ incident at the gold-prism interface.

2.3.9 Electric field transmitted at the gold-prism interface

The boundary conditions at the gold-prism interface are given by

$$-E_{i-012} \cos \theta_1 + E_{r-321} \cos \theta_1 = -E_{t-012} \cos \theta_2 + E_{i-321} \cos \theta_2 \quad (2.59a)$$

and

$$\mathbf{H}_{iy-012} + \mathbf{H}_{ry-321} = \mathbf{H}_{iy-012} + \mathbf{H}_{iy-321} \quad (2.59b)$$

From the two equations above, the reflected magnetic field \mathbf{H}_{ry-321} is related to incident magnetic field in \mathbf{H}_{iy-012} as

$$\mathbf{H}_{ry-321} = r_{321} \mathbf{H}_{iy-012}, \quad (2.60)$$

in which r_{321} represents the total reflection coefficient from sample into the prism expressed in the general form as Eq. (2.41). **Fig. (2.16)** shows the total reflectance $R = |r_{321}|^2$ plotted as a function of the angle of incidence θ_1 by using Eq. (2.41). The plot contains the discontinuity point corresponds to the critical angle of the prism interfaced with water at 48.2° , while the minimum point is the dip intensity of the SPR reflectivity.

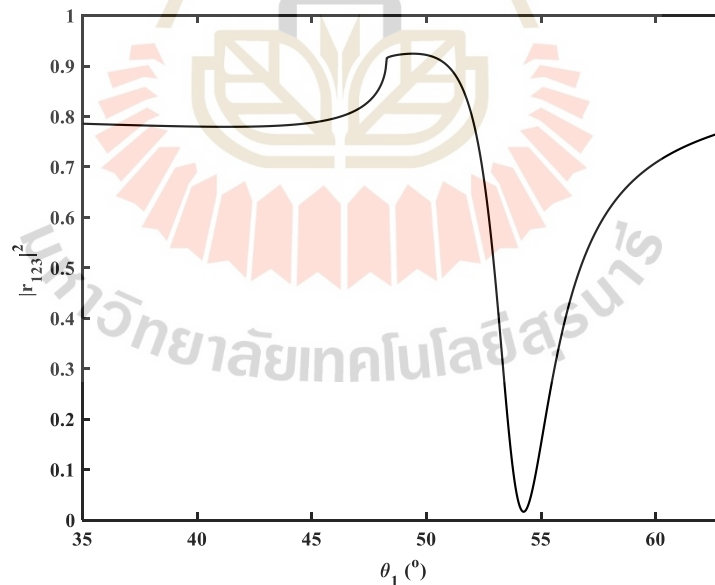


Figure 2.16. The total reflectance from the sample into the prism $R = |r_{321}|^2$ as a function of the angle of incidence θ_1 .

Henceforth, the product of the wave impedance Z_g and the magnetic field H_{iy-321} gives
 Since the resultant reflected electric field in the prism can be written as $E_{r-321} = Z_g H_{ry-321}$, the components of the electric field in the x and the z directions are given by

$$\begin{aligned}
 E_{rx-321} &= \left[(120\pi/n_p) \cos \theta_1 \right] H_{ry-321} \\
 &= (120\pi/n_p) \cos \theta_1 H_{ry-321}
 \end{aligned}
 \tag{2.61a}$$

and

$$\begin{aligned}
 E_{rz-321} &= \left[(120\pi/n_p) \sin \theta_1 \right] H_{ry-321} \\
 &= (120\pi/n_p) \sin \theta_1 H_{ry-321}
 \end{aligned}
 \tag{2.61b}$$

respectively. **Figure. 2.17(a)** and **17(b)** show the variation of the reflected electric fields along the x and the z directions as a function of the angle of the incidence θ_1 , respectively. The two plots show that due to the prism is non-conducting material, the reflected field becomes higher than that inside the gold layer. In general, $|E_{rx-321}|^2$ tends to decrease, while $|E_{rz-321}|^2$ increases as the angle θ_1 becomes higher. The discrepancy of the fields is caused by the fact that the cosine and the sine function exhibit opposite variations. These trends are in agreement with those of the field incident on the prism-gold interface shown in **Fig. (2.7)**. A sharp attenuation of the reflected electric fields is the direct result of the photon energy absorption by the surface plasmons.

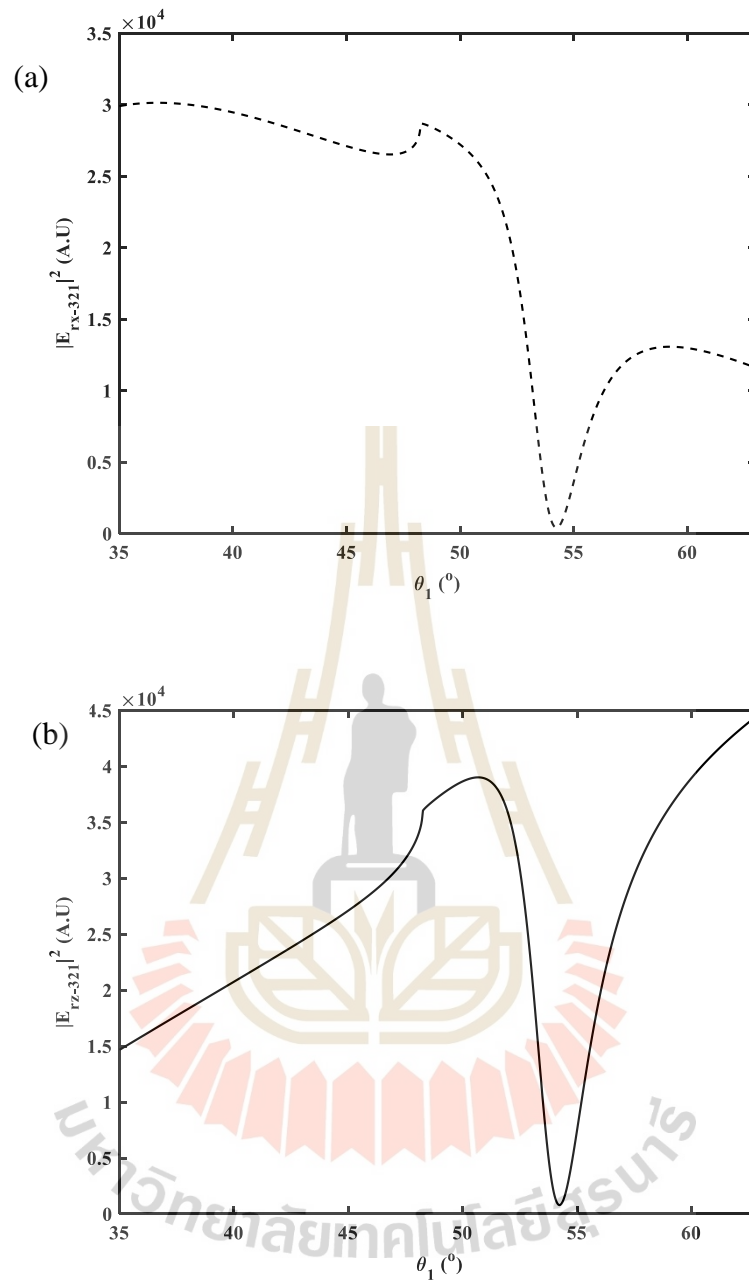


Figure 2.17. The squared modulus of the electric fields (a) $|E_{rx-321}|^2$ and (b) $|E_{rz-321}|^2$ reflected from the gold-prism interface.

2.3.10 Electric field transmitted at the prism-air interface

The light intensity detected by an array image sensor can be determined by finding the mathematical expression for the transmitted electric field. The boundary conditions at the prism-air interface can be expressed as

$$-E_{i-3210} \cos \theta_0 + E_{r-01} \cos \theta_0 = -E_{r-43210} \cos \theta_{0r} \quad (2.62a)$$

and

$$H_{iy-3210} + H_{ry-01} = H_{ry-3210} \quad (2.62b)$$

Therefore, when two boundary equations are solved, the transmitted magnetic field is found as $H_{ry-3210} = t_{10}H_{iy-3210}$, where t_{10} denotes the transmission coefficient for the prism-air interface given by

$$t_{10} = \frac{2n_0 \cos(\alpha - \theta_1)}{n_0 \cos(\alpha - \theta_1) + n_p \cos\left[\sin^{-1}\left(n_p \sin(\alpha - \theta_1)\right)\right]} \quad (2.63)$$

Figure 2.18 plots the transmission coefficient t_{10} as a function of the angle of incidence θ_1 . The transmission becomes bigger as the angle θ_1 decreases. This is because the refractive index of the second medium is smaller than that of the first medium. It reaches minimum at the angle $\theta_1 = 60^\circ$, which corresponds to the normal incident angle at the air-prism interface.

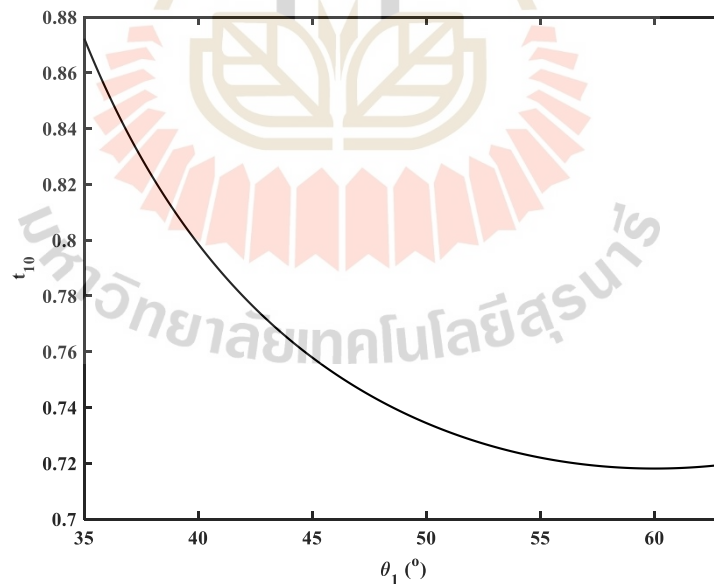


Figure 2.18 Variation of the transmission coefficient t_{10} for the prism-air interface as a function of the angle of incidence θ_1 .

Furthermore, $H_{iy-3210}$ represents the magnetic field incident at the prism-air interface, which is equal to the phase-shifted magnetic field $H_{ry-321} \exp(j\beta_1)$.

The resultant of the transmitted electric field E_{r-3210} is determined by multiplying the transmitted magnetic field $H_{ry-3210}$ and the wave impedance Z_0 of the free space that is $E_{r-3210} = Z_0 H_{ry-3210} = 120\pi H_{ry-3210}$. The x and the z components of the electric field is finally computed from resultant electric field E_{r-3210} as follows

$$E_{rx-3210} = 120\pi \cos\left[\sin^{-1}\left(n_p \sin(\alpha - \theta_1)\right)\right] H_{ry-3210} \quad (2.64a)$$

and

$$E_{rz-3210} = 120\pi \left[n_p \sin(\alpha - \theta_1)\right] H_{ry-3210}, \quad (2.64b)$$

respectively. **Figure (2.19)** depicts the variation of the electric fields $|E_{rx-3210}|^2$ and $|E_{rz-3210}|^2$ as a function of the incident angle θ_1 at the prism-air interface. **Fig. (2.19a)** indicates the electric field $|E_{rx-3210}|^2$ slowly increases between the incidence angle $\theta_1 = 35^\circ$ to 48.2° which is the critical angle. This is because the argument of the cosine term corresponds to the incident angle θ_1 at the air-prism interface, which has an inverse relationship with the angle θ_1 as shown in **Fig. 2.3**. Beyond the critical angle, the sudden dip of the signal is due the photon energy absorption. After the resonance region, the x-component of the transmitted electric field increases with the similar reason for the region smaller than the critical angle. **Fig. (2.19b)** shows the variation of the z component of the transmitted electric field as a function of incident angle θ_1 . The decrease in the electric field $|E_{rz-3210}|^2$ is caused by the sine term in Eq. (2.64b) as the angle of incidence θ_1 increases. Furthermore, around the resonance position the field reduces to minimum, because of the photon energy absorption phenomena. At the incident angle of 60° , $|E_{rz-3210}|^2$ becomes zero. This is because the resultant electric field consists only of the x component. Finally, the resultant electric field $|E_{rx-3210} + E_{rz-3210}|^2$ detected by the sensor is plotted in **Fig. (2.20)**. It is apparent that the plot of the detected field is in a good agreement with the variation of the total reflectance from the sample into the prism $R = |r_{321}|^2$ shown in **Fig. 2.16**. Therefore, the comparison

result validates the mathematical derivation of the TM wave propagation and the numerical calculation used in this thesis work.

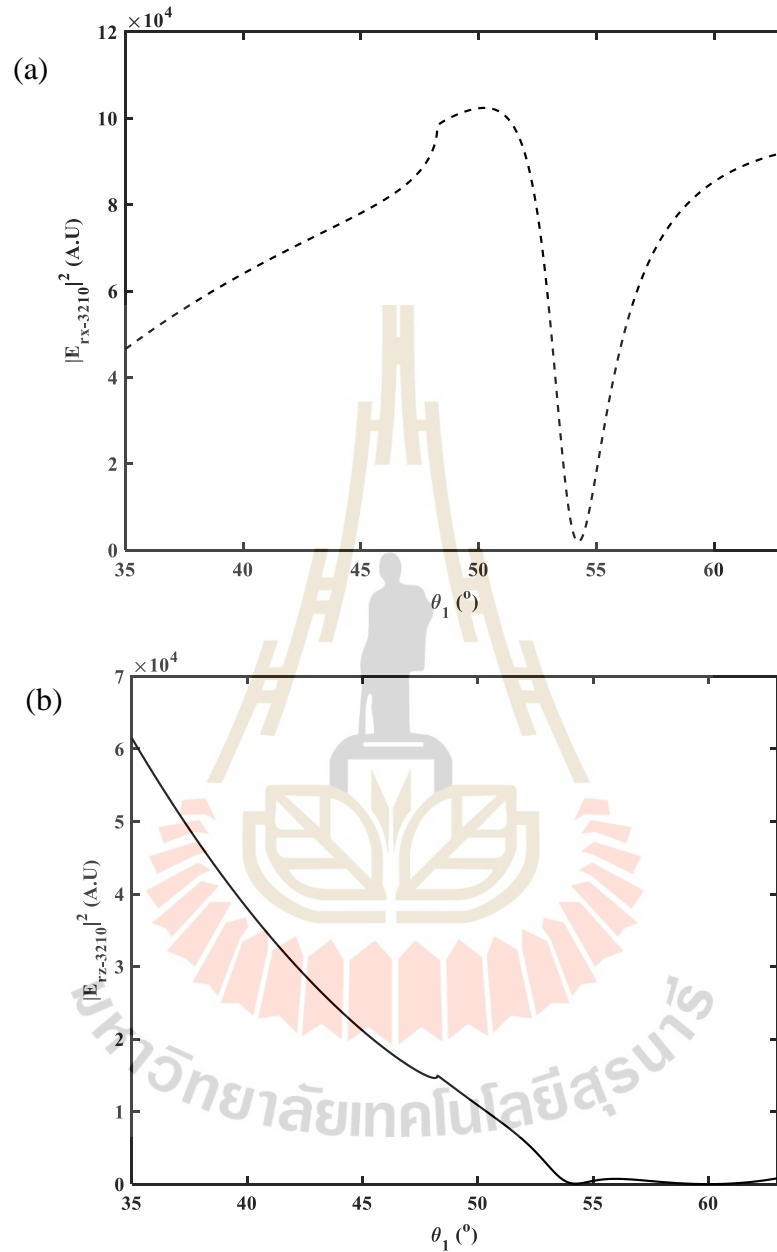


Figure 2.19. The squared modulus of the electric fields (a) $|E_{rx-3210}|^2$ and (b) $|E_{rz-3210}|^2$ transmitted at the prism-air interface.

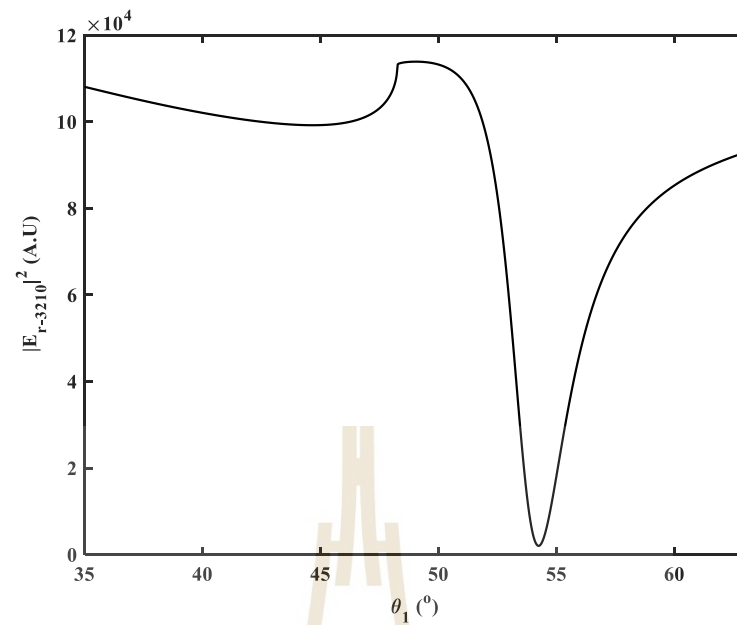


Figure 2.20. The squared modulus of the total electric fields $|E_{r-3210}|^2$ detected by the sensor.

CHAPTER III

RESEARCH METHODOLOGY

3.1 Introduction

This study has two main objectives: The first objective is to perform experimental validations of the developed theory by measuring simultaneously a broad refractive index variation of 1.0003 ~ 1.3580. Air, water and ethanol will be used as test samples. The second goal is to investigate how the misalignment gap affects SPR reflectivity in a Kretschmann-based 6-layer SPR sensor. The investigation will be conducted by analyzing the total SPR reflectivity graph's results.

3.2 Divergent beam illumination and detection

3.2.1 SPR sensor using Powell lens

A schematic illustration of the divergent illumination and detection in the SPR sensor setup using Powell lens is illustrated in **Fig. 3.1**. The setup is based on a prism coupling configuration proposed by Kretschmann (Kretschmann and Raether 1968), in which the surface plasmon excitation is achieved by using the p -polarized illumination. After passing Powell lens, the p -polarized beam diverges with uniform energy distribution. This beam is obliquely incident on the side AC of a prism with an apex angle ϕ and a refractive index n_p . In order to measure refractive index changes between n_1 and n_2 , the refracted rays EG and FH are set to be incident on the interface between the prism – gold film at angles α_{i2} and β_{i2} , respectively, which cover possible resonance angles of the refractive indices to be measured.

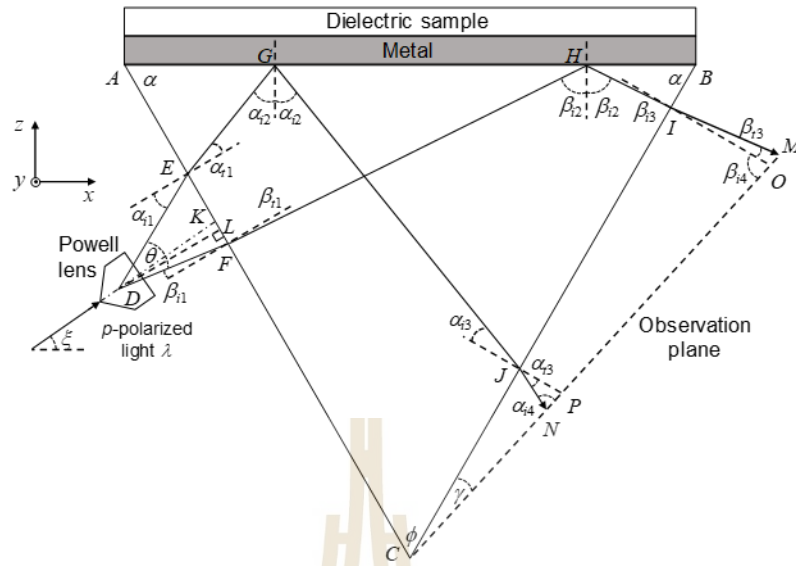


Figure 3.1 Schematic illustration of the divergent illumination-based SPR sensor setup using Powell lens

3.2.2 Fan, Illumination and Observation Angles

After the angles α_{i2} and β_{i2} are defined, the angles of incidence of the diverging beam at the side AC can be derived by using the Snell's law as

$$\alpha_{i1} = \arcsin \left[n_p \cos(\phi/2 + \alpha_{i2}) \right] \quad (3.1)$$

and

$$\beta_{i1} = \arcsin \left[n_p \cos(\phi/2 + \beta_{i2}) \right], \quad (3.2)$$

respectively. The fan angle of the readout beam can be mathematically expressed as

$$\begin{aligned} \theta &= \alpha_{i1} - \beta_{i1} \\ &= \arcsin \left[n_p \cos(\phi/2 + \alpha_{i2}) \right] + \arcsin \left[n_p \cos(\phi/2 + \beta_{i2}) \right] \end{aligned} \quad (3.3)$$

which shows that the full beam divergence angle θ must be determined by taking into account the measurable range of the resonance angles and the prism material together with its apex angle. Consequently, a principal axis of the illuminating beam must be tilted with respect to the x axis to provide an illumination angle

$$\begin{aligned}\xi &= (\phi + \theta)/2 - \beta_{i1} \\ &= (\phi + \theta)/2 + \arcsin \left[n_p \cos(\phi/2 + \beta_{i2}) \right].\end{aligned}\quad (3.3)$$

When one particular light ray is incident on the side AC at the angle

$$\beta_{spr} = \sin^{-1} \left(\frac{1}{n_p} \sqrt{\frac{n_m^2 n_s^2}{n_m^2 + n_s^2}} \right), \quad (3.5)$$

the x component of the evanescent wave vector in the interface matches to that of the surface plasmon, yielding plasmon resonance. β_{spr} in Eq. (3.5) is known as the resonance angle (Kretschmann and Raether 1968). In SPR sensing, the refractive indices of the prism and the metal n_m are known, thus, β_{spr} is dependent upon the refractive indices of the sample n_s being analyzed. When energy of the evanescent wave generated at the angle β_{spr} is absorbed by the surface plasmons, the corresponding reflected light intensity reduces drastically. Therefore, a detection of the spatial position of the dip light intensity at an observation plane can be used to measure the resonance angle. Owing to different exit angles of the totally reflected beam, the detection of the dip intensity can be accurately detected, provided that the observation plane is inclined with respect to the prism side BC by an angle

$$\gamma = (\alpha_{i1} + \beta_{i1})/2. \quad (3.6)$$

At this observation angle, the beams IM and JN will incidence at the same angle of the incidence on the light detector placed on the observation plane.

3.2.3 Beam widths

A relation between the resonance angle on the sensing area and the dip intensity position on the light detector can be mathematically established by determining widths of divergent beams on three sides of the prism and the light detector that are EF , GH , IJ and MN . According to geometrical analysis, the width EF of the divergent beam in the prism side AC is given by

$$EF = \frac{DL \sin \theta}{\cos \alpha_{i1} \cos \beta_{i1}}, \quad (3.7)$$

with DL is the normal distance from the prism surface to the focal point of the lens.

From triangles $\triangle AGE$ and $\triangle AHF$, the beam width GH on the hypotenuse is calculated by subtracting AG from AH

$$GH = AE \left[\frac{\sin(\phi/2 + \beta_{i2})}{\cos \beta_{i2}} - \frac{\sin(\phi/2 + \alpha_{i2})}{\cos \alpha_{i2}} \right] + EF \frac{\sin(\phi/2 + \beta_{i2})}{\cos \beta_{i2}}. \quad (3.8)$$

This beam width determines the minimum dimension of the sensing area. Besides being dependent upon the range of the measurable resonance angle and the prism apex angle, it is determined by the width of the incidence beam EF and its position AE measured from the vertex A .

At the exit side of the prism, the width IJ of the reflected beam is found to be

$$IJ = AB \left[\frac{\cos \alpha_{i2}}{\sin(\phi/2 + \alpha_{i2})} - \frac{\cos \beta_{i2}}{\sin(\phi/2 + \beta_{i2})} \right] - AE \left\{ 1 - \frac{\sin(\phi/2 + \alpha_{i2}) \cos \beta_{i2}}{\sin(\phi/2 + \beta_{i2}) \cos \alpha_{i2}} \right\} + GH \frac{\cos \beta_{i2}}{\sin(\phi/2 + \beta_{i2})}. \quad (3.9)$$

At the detector plane, the beam diverges further to

$$MN = \frac{IJ \cos \beta_{i1} + BI(\cos \alpha_{i1} - \cos \beta_{i1})}{\cos \gamma}, \quad (3.10)$$

with α_{i1} and β_{i1} are given by Eqs. (3.1) and (3.2). Equation (3.10) can be regarded as a mapping of the resonance angle on the detecting elements of the light detector. When the dip intensity on the detector plane is detected, the corresponding angle β_{spr} can be determined by using this equation, yielding measurement of the desired refractive index of the sample. It is clear that the output beam size is determined by the inclination angle of the light detector such that a small inclination angle causes a small

length difference between the two beams IJ and MN . Note that the incidence position AE determines whether the whole reflected beam GH will strike the prism side BC .

3.3 Effects of misalignment gap

Although the proposed divergent beam illumination is excelled in the parallel measurement of multiple samples using single-shot acquisition, the large sensing area requires a large gold sensor plate. In practice, placing the large gold plate on top of the prism may cause misalignment, in particular when index matching liquids are filled between the gap of the plate and the prism. To further validate the developed method, the effects of the misalignment gap are studied by following the real experimental setup such that the gold plate is a Swiss glass slide (20mm×20mm×1mm) with evaporated 5 nm chromium and 45 nm gold film (BA1000, Nano SPR) and the index matching liquid (IML) is Cargille refractive index liquid (Series A, Cargille).

Figure 3.2 shows a schematic diagram of the 6-layer SPR system, which comprises the equilateral prism ($n_p = 1.785$), the index matching liquid ($n_m = 1.61$), the glass slide ($n_{gl} = 1.61$), the chromium ($n_c = 3.139 + j3.316$) and the gold ($n_g = 0.1726 + j3.4218$) layers and a water sample ($n_s = 1.3317$). The p-polarized light with the same wavelength $\lambda = 632.8$ nm is incident on the interface of the prism and the glass with the gap thickness d_2 . The glass thickness d_3 is 1 mm, while the misalignments are introduced by varying uniformly and non-uniformly the thickness d_2 . According to the theoretical analysis in Chapter 2, the derived light intensity $|E_{rx-3210} + E_{rz-3210}|^2$ detected by the detector can be described by using the total reflectance $R = |r_{321}|^2$. Therefore, to avoid the repetitive analysis; the total SPR reflectivity will be applied to study the misalignment effects of the gold plate layer. As the first study step, the effect of the misalignment on the reflectivity will be studied by considering that the gap with the thickness $d_2 = 0$.

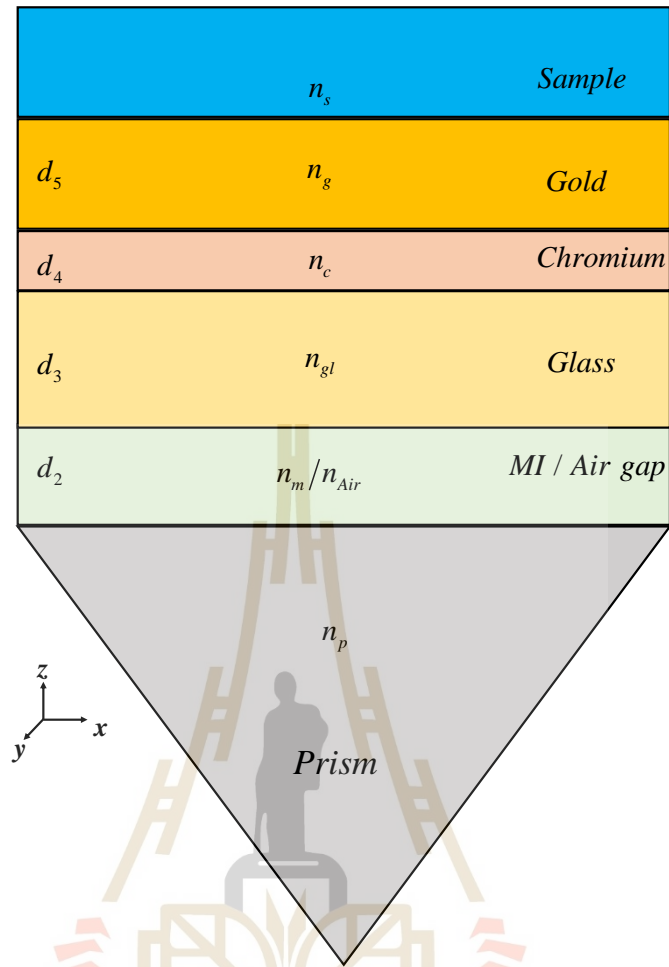


Figure 3.2 A schematic diagram of the 6-layers of the SPR sensor.

The total reflection coefficient r_{654321} from the sample to the prism is given by (Shalabney and Abdulhalim 2010)

$$r_{654321} = \frac{(m_{11} + q_6 m_{12}) q_1 - (m_{21} + q_6 m_{22})}{(m_{11} + q_6 m_{12}) q_1 + (m_{21} + q_6 m_{22})} \quad (3.11)$$

with m_{11} , m_{12} , m_{21} and m_{22} are the elements of the total transfer matrix M , Eq. (3.11) consists of five reflection coefficients that are the coefficients from the matching liquid-prism r_{21} , the matching liquid-prism r_{32} , the chromium-matching liquid r_{43} , the gold-chromium r_{54} and the water-gold r_{65} interfaces. The total transfer matrix M is defined as by (Shalabney and Abdulhalim 2010)

$$M = \left\{ \begin{bmatrix} \cos \beta_2 & -i \frac{1}{q_2} \sin \beta_2 \\ -jq_2 \sin \beta_2 & \cos \beta_2 \end{bmatrix} \begin{bmatrix} \cos \beta_3 & -i \frac{1}{q_3} \sin \beta_3 \\ -jq_3 \sin \beta_3 & \cos \beta_3 \end{bmatrix} \right. \\ \left. \times \begin{bmatrix} \cos \beta_4 & -i \frac{1}{q_4} \sin \beta_4 \\ -jq_4 \sin \beta_4 & \cos \beta_4 \end{bmatrix} \begin{bmatrix} \cos \beta_5 & -i \frac{1}{q_5} \sin \beta_5 \\ -jq_5 \sin \beta_5 & \cos \beta_5 \end{bmatrix} \right\} \quad (3.12a)$$

which is the product of the four matrices of the matching liquid, the glass, the chromium and the gold layers. The transfer matrix of each layer is determined by the wave impedance q and their phase factor β that are affected by the corresponding thickness d of the layer.

In a general matrix expression, Eq. (3.12a) can be simplified as

$$M = \begin{bmatrix} m_{11} & m_{12} \\ m_{21} & m_{22} \end{bmatrix} \quad (3.12b)$$

In Eq. (3.12a) where, β_2 , β_3 , β_4 and β_5 denote the phase shift caused by the thickness layers of the matching liquid d_2 , the glass slide d_3 , the chromium d_4 and the gold d_5 , respectively. Their corresponding phase shifts are defined as

$$\beta_2 = \frac{2\pi d_2}{\lambda} (n_m^2 - n_p^2 \sin^2 \theta_1)^{\frac{1}{2}}, \quad (3.13)$$

$$\beta_3 = \frac{2\pi d_3}{\lambda} (n_{gl}^2 - n_p^2 \sin^2 \theta_1)^{\frac{1}{2}}, \quad (3.14)$$

$$\beta_4 = \frac{2\pi d_4}{\lambda} (n_c^2 - n_p^2 \sin^2 \theta_1)^{\frac{1}{2}} \quad (3.15)$$

and

$$\beta_5 = \frac{2\pi d_5}{\lambda} (n_g^2 - n_p^2 \sin^2 \theta_1)^{\frac{1}{2}}. \quad (3.16)$$

Since the phase shift values are linearly proportional to the layer thickness, they affect the light wave propagation through each layer. Furthermore, q_2 , q_3 , q_4 and q_5 defined as (Shalabney and Abdulhalim 2010)

$$q_2 = Z_m \left[n_m^2 - (n_p \sin \theta_1)^2 \right]^{1/2} / n_m, \quad (3.17)$$

$$q_3 = Z_{gl} \left[n_{gl}^2 - (n_p \sin \theta_1)^2 \right]^{1/2} / n_{gl}, \quad (3.18)$$

$$q_4 = Z_c \left[n_c^2 - (n_p \sin \theta_1)^2 \right]^{1/2} / n_c, \quad (3.19)$$

$$q_5 = Z_g \left[n_g^2 - (n_p \sin \theta_1)^2 \right]^{1/2} / n_g \quad (3.20)$$

and

$$q_6 = Z_s \left[n_s^2 - (n_p \sin \theta_1)^2 \right]^{1/2} / n_s \quad (3.21)$$

denote the tangential component of wave impedances of the matching index, the glass, the chromium, the gold and the sample respectively.

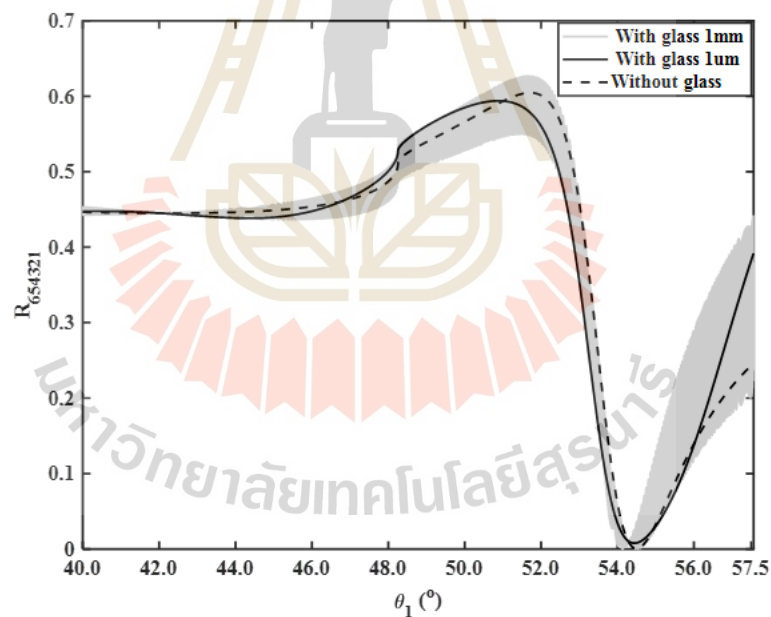


Figure 3.3. Total reflectance power $R_{654321} = |r_{654321}|^2$ as a function of the angle of incidence θ_1 for without glass and with the glass thickness of 1 mm and 1 μm .

In **Fig. 3.3** the total reflectance $|r_{654321}|^2$ is plotted as the function of the incidence angle θ_1 for different glass thickness d_3 . The gray, the black and the dashed

lines represent the reflectivity obtained by using the glass thickness d_3 of 1.0 mm, 1.0 μm and 0 μm , respectively. When the glass slide, regardless of the thickness, is directly placed on the prism, the gap d_2 is 0 μm . This implies that the phase factor β_2 is zero, thus the SPR reflectivity signal is independent upon the gap. Despite of the absence of the gap, the SPR reflectivity curve appears wider than in the case without the glass slide. This happened because of the refractive index difference between the prism and the glass. It is apparently seen that the refractive index difference leads to a ripple on the total reflectivity of the SPR signal as indicated in the **Fig. 3.3**. The ripple is the result of an interference between the ray directly reflected from the prism-glass interface and the ray reflected at the glass-chromium interface after being partly refracted from the prism-glass interface. Thus, the ripple has a form of an interference fringe (Geng, Li et al. 2010). The occurrence of the interference fringe is confirmed by reducing the glass thickness to 1.0 μm . The ripple reduces, while the broadening of the reflectance still exists due to the refractive index difference. As the result of the interference fringe on the SPR reflectivity signal, some studies have utilized a gold coated glass that was 0.3 mm thick (Zhang, Chen et al. 2014) while others have used 0.15 mm (Mauriz, Calle et al. 2007).

Furthermore, the fringe amplitude increases as the incidence angle increases. This is because the increase of the reflectivity power at the glass-prism interface. However, the fringe amplitude reduces at the Brewster angle because there is no reflection of the TM wave at the glass-prism interface and at the resonance position where most of the photon energy is absorbed to the sample. Therefore, the interference fringe on the SPR reflectivity can be eliminated by using the glass with the same optical properties as the prism.

3.3.1 Analysis of interference fringe on the SPR signal

The occurrence of the interference fringe ripple can be explained by considering the optical path difference (OPD) between a directly reflected ray on the prism-glass interface and a refracted ray after one time reflection from the glass-metal interface. The angles θ_1' and θ_3' represent the incident and the refracted angles of the ray 1, while the angle θ_1'' and θ_1''' represent incident and refracted angles of the

ray 2, respectively (see Fig. 3.4).. Ray 1 and Ray 2 are two adjacent light rays incident on the prism-glass interface

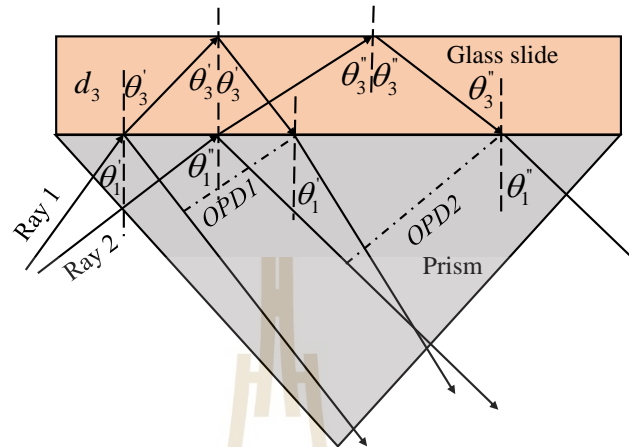


Figure 3.4 The occurrence of the interference fringes between two consecutive rays.

The OPD of the ray 1, $OPD1$, can be expressed as

$$OPD\ 1 = 2n_{gl}d_3 \cos \theta_3' \quad (3.22)$$

In similar fashion, the ray 2 has the path difference $OPD2$

$$OPD\ 2 = 2n_{gl}d_3 \cos \theta_3'' \quad (3.23)$$

The constructive interferences caused by the differences $OPD1$ and $OPD2$ can be written as

$$\Delta l_1 = 2n_{gl}d_3 \cos \theta_3' \pm \lambda/2 = m\lambda \quad (3.24)$$

and

$$\Delta l_2 = 2n_{gl}d_3 \cos \theta_3'' \pm \lambda/2 = (m+1)\lambda \quad (3.25)$$

where m is the integer number.

Consequently, the spacing of the two adjacent fringes can be expressed as [2]

$$2n_{gl}d_3(\cos\theta_3'' - \cos\theta_3') = \lambda, \quad (3.26)$$

Assuming the difference the two adjacent refracted angle is infinitesimally small $\Delta\theta_3 = \theta_3'' - \theta_3'$ Eq. (3.26) can be approximately rewritten as

$$\Delta\theta_3 = \frac{\lambda}{2n_{gl}d_3 \sin\theta_3''} \quad (3.27)$$

or

$$\Delta\theta_3 = \frac{\lambda}{2n_{gl}d_3 \sin\theta_3''} (180/\pi). \quad (3.28)$$

When the Snell's law is applied to Eq. (3.28) the fringe spacing equation can be expressed as follows

$$\Delta\theta_3 = \frac{\lambda}{2n_p d_3 \sin\theta_1} (180/\pi) \quad (3.29)$$

3.3.2 Verification of the existence of the interference fringe

Figure 3.5 shows the comparison of the fringe spacings computed by using the total reflectivity of the 6-layer setup given by Eq. (3.11) and the derived formula of Eq. (3.29) as a function of the incident angle θ_1 . They are represented by using the solid and the dashed lines, respectively. It is shown that the theoretical fringe spacing decreases as the incident angle increases. This is because the factor $\sin\theta_1$ in the denominator of Eq. (3.29) becomes higher as the incident angle increases.

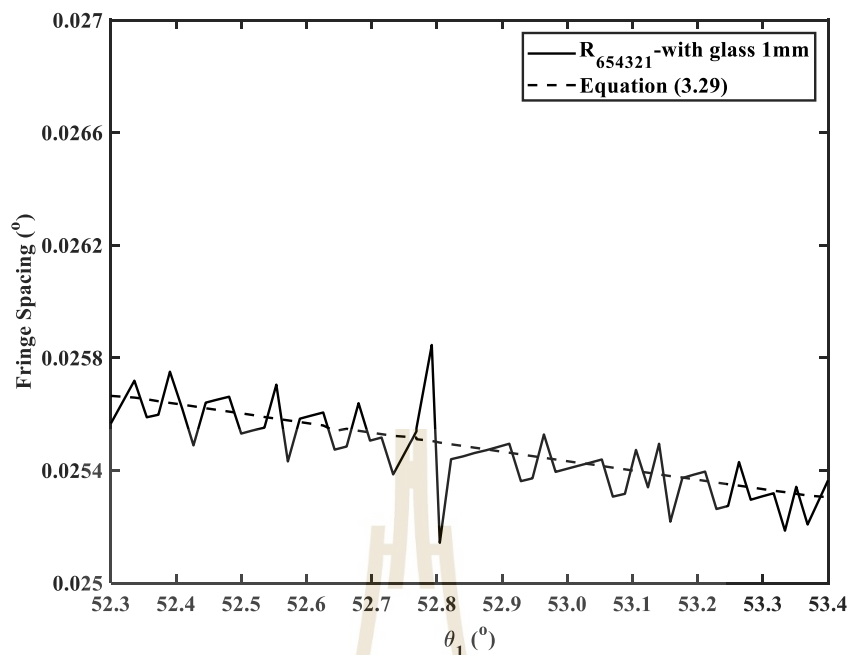


Figure 3.5 Comparison of the fringe spacings calculated by using the total reflectivity of the 6-layer setup given by Eq. (3.11) and the derived formula of Eq. (3.29) and as a function of the incident angle θ_1 .

According to the theory of interferometry (Hariharan 2010), the fringe spacing is defined as the spacing between two bright fringes. In the reflectance R_{654321} plotted by using Eq. (3.11), they are approximately equal to the alternate reflectance peaks. It is obvious from Fig. 3.5 that the spacings calculated from the reflectance fluctuate around the theoretical values. The spacing fluctuation may be caused by the fact that firstly, the fringe peaks are affected by the variation of the SPR reflectivity signal. Secondly, the reflectance was derived from the electric fields behind the prism exit surface BC , which is different than the interface between the prism-glass. Therefore, it can be concluded that the ripple on the SPR reflectance can be explained by using the principle of multiple-reflections of light. In this case, the thickness of the glass is the primary cause of the ripple on the SPR reflectivity. Furthermore, the unwanted ripple may be removed by using a band-pass filter with a center frequency given by Eq. (3.29).

CHAPTER IV

EXPERIMENTAL VERIFICATIONS

4.1 Beam shaping with Powell lens

In 1986, Ian Powell invented the Powell lens (Powell 1989). It is a type of optical lens that transforms a Gaussian beam into a uniform beam line. The Gaussian laser beam has a higher field distribution in its center than at its extremities. This may cause a problem when uniform photon energy distribution is required to equally generate plasmon resonances along a wide interface of the gold and dielectric layers. To generate uniform field distribution, Powell lens has two surfaces that are the primary and secondary surfaces. The apex of the primary surface is responsible for spreading out light radiation more quickly in the middle than at the extremities. The secondary surface uses refraction principles to increase the divergence of the incidence fan rays. When the primary surface has a higher slope of the top and the secondary surface has a higher refractive index, the fan angle becomes large. A lower slope of the primary surface and the refractive index of the secondary surface, the fan angle is small.

The difference between the beam outputs generated experimentally by using a cylindrical and Powell lenses is shown in Fig. 4.1. Fig. 4.1(a) show the beam intensity pattern of the He-Ne laser recorded at the entrance surface of the lenses. Figs. 4.1(b) and (c) are the intensity output patterns of the cylindrical and the Powell lenses recorded at distances 16 cm and 6 cm away from the lenses, respectively. It is apparent that the Powell lens diverges the beam wider than the cylindrical lens.



Figure 4.1 Beam profiles transmitted from (a) the laser source, (b) the cylindrical lens and (c) the Powell lens, respectively.

Figure 4.2 shows a comparison of the corresponding normalized beam intensities averaged along the vertical direction. The dashed, the solid and the dashed-dotted lines correspond to the laser, the cylindrical lens and the Powell lens outputs shown in Fig. 4.1. Although the cylindrical lens produces 1D divergent beam, the output still has a Gaussian-shaped distribution. In contrast, the Powell lens diverges the light rays around the optical axis more rapidly than marginal rays. As a result, the field distribution around edges is the highest.

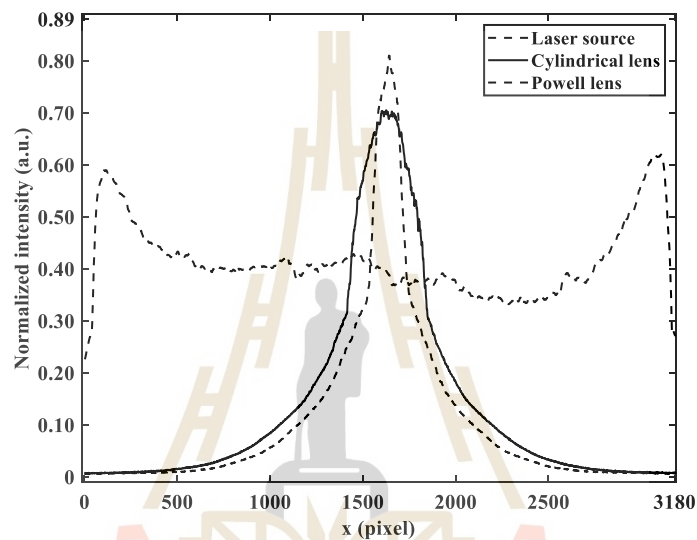


Figure 4.2 The corresponding normalized beam intensities obtained from the source, the cylindrical lens, and the Powell lens.

4.2 Experimental measurement of refractive index

Validity of the derived analytical conditions was experimentally verified at room temperature by using the Powell lens-based SPR sensor shown in **Fig. 4.3**. The polarizing beam splitter cube selected the p -polarization state of a He-Ne laser light operating at the wavelength $\lambda = 632.8$ nm, while the rotating half-wave plate was used to ensure that the illuminating beam tilted to the angle ξ by the mirror had the correct p -polarization state. The prism coupling was implemented by using a 50 mm SF11 equilateral prism ($n_p = 1.785$) having the critical angle of 34.07° . Besides water and absolute ethanol, air was used as one of the test samples for calibration. In order to produce the evanescent wave across broad range of the three refractive indices,

the incident angles at the sensing area were set to cover the range from 34° to 57° . By taking Eqs. (3.1) and (3.2) into account, the minimum fan angle θ of the divergent beam was found to be about 46° . Thus, Powell lens having a fan angle of 60° was chosen to diverge uniformly the p -polarized light. The incident distance AE was set to be 7.1 mm, while the Powell lens distance DL was 8 mm. Each SPR measurement was conducted by attaching a 20 mm \times 20 mm Au evaporated glass plates (Nano SPR, BA1000) with the refractive index $n_m = 0.1726 + j3.4218$ (Yamamoto 2002) to the hypotenuse AB . To cover a broad range of the incident angles, the diagonal of the plate was oriented to be parallel to the prism hypotenuse. Index matching liquid (Cargille series A) was added in the gap between the prism and the glass plate in order to reduce light loss. Test samples were drop at particular positions on the glass plate by using a 10-microliter pipette (Glassco). The drop position was determined by substituting the resonance angle of the corresponding liquid into Eq. (3.8). Totally reflected intensity patterns were captured by using a 2D CMOS image sensor (Sony Exmor R IMX251) with 7952 \times 5304 pixels in an area of 35.9 mm \times 23.8 mm. For the sake of clarity, a screen was installed in the observation plane inclined by the angle γ . It can be clearly seen from **Fig. 4.3** that the light output reflected from all incident angles on the sensing area forms a straight line pattern given by Eq. (3.10). As a result, unlike the conventional scanning method, the SPR reflectivity from a broad range of angles could be detected from one-shot recording.

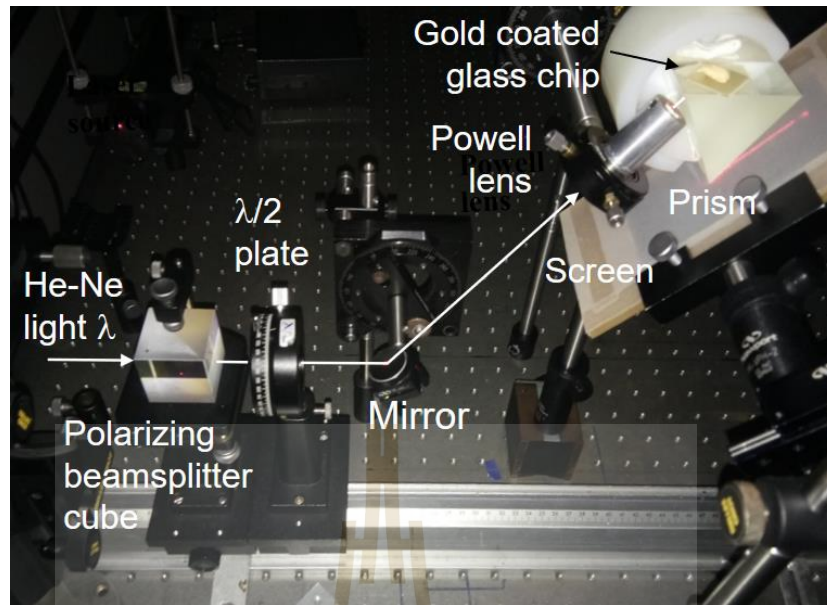


Figure 4.3 Experimental setup for implementing the divergent illumination-based SPR sensor using Powell lens (Widjaja and Hossea 2021).

4.2.1 Simultaneous sensing of air and water

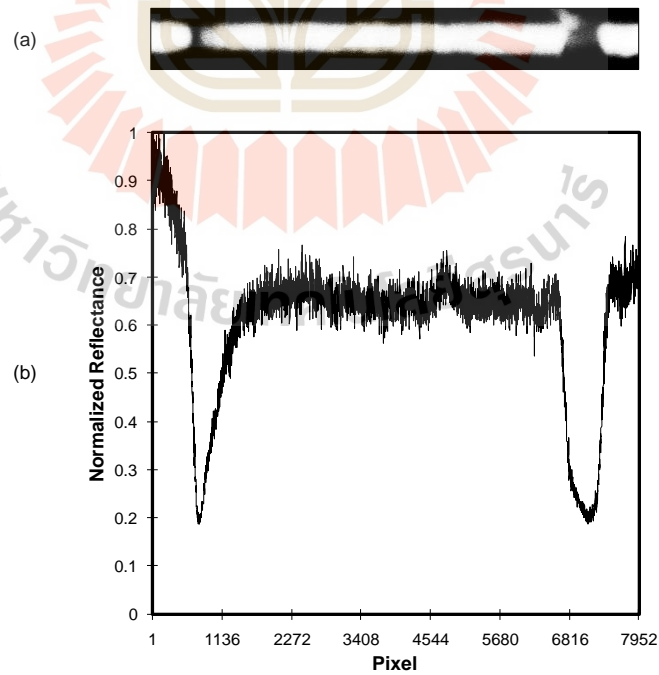


Figure 4.4 (a) SPR reflectivity pattern of air and water and (b) its corresponding normalized reflectivity averaged along the vertical direction.

The first experimental verification was conducted by measuring simultaneously the SPRs of air ($n_s = 1.0003$) (Workman and Workman 2001) and water ($n_s = 1.3317$) (Hale and Query 1973). **Figure 4.4(a)** shows the SPR reflectivity pattern captured by the CMOS sensor placed at the observation plane. The captured pattern maps the angle of incidence on the sensing area to the CMOS pixels, such that the bigger the incident angle the higher the number of pixel position. The measured width of the reflectivity pattern in the vertical direction is about 200 pixels or about 1 mm. It can be clearly seen that the reflected pattern is clearly separated into three parts by two dark bands caused by photon absorptions during the resonances of surface plasmons at the gold - air and the gold - water interfaces, respectively. The darkest level of the bands was obtained by adjusting the angle of the half-wave plate around the beam axis. The well-defined bands indicate that the gold-evaporated glass plate used in this experiment was not contaminated. The dark band appeared on the left side of the pattern has a narrower width than the one on the right side. This is because for the lower refractive index of air, the transfer of photon energy occurs over a narrower range of the incident angle. Consequently, the dark SPR band is sharpened.

To extract the positions of the SPR reflectivity minima, 1D intensity profile shown in **Fig. 4.4(b)** was calculated by taking an arithmetic mean of the reflectivity pattern along its vertical width. Although the 1D SPR reflectivity is smeared by small intensity fluctuations, which may be caused by light scattering and non-uniform distribution of the index matching liquid, the two dip intensities can be clearly identified. By measuring the lowest depth of the SPR dip of about 0.18, the energy transfer for air and water are estimated to be equal to 73 %. This represents the best efficiency of the energy transfer from the evanescent wave to surface plasmons that could be obtained in this work. Finally, the lowest depth position of the SPR absorption of air is detected at the pixel number 713 of the sensor, while that of the resonance of water sample is at the pixel 7107 (Widjaja and Hossea 2021).

4.2.2 Simultaneous sensing of air and ethanol

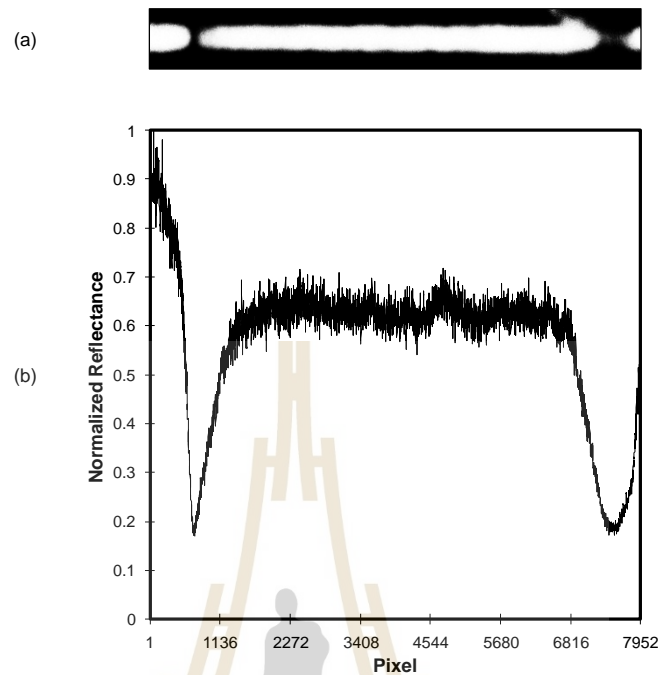


Figure 4.5 (a) SPR reflectivity pattern of air and ethanol and (b) its corresponding ‘normalized reflectivity averaged along the vertical direction.

The second experimental verification measured the SPRs of air and absolute ethanol ($n_s = 1.3580$) (Workman and Workman 2001). The SPR reflectivity pattern and its corresponding averaged intensity are shown in **Figs. 4.5(a)** and **(b)**, respectively. The first dark band is caused by the same resonance at the gold - air interface, while the second dark line is produced by that at the gold - ethanol interface. A comparison with **Fig. 4.4** shows that the lowest depth of the reflectivity caused by the SPR absorption of air in **Fig. 4.5** appeared at the same position. However, the SPR dip of ethanol is shifted toward to the pixel 7523 and its width broadened. This result is consistent with the fact that the higher refractive index of ethanol causes the energy transfer from the evanescent wave to surface plasmons occurs over a broader range of the incident angle. The efficiencies of the energy transfer are almost the same as the previous measurement (Widjaja and Hossea 2021).

4.2.3 Sensor sensitivity

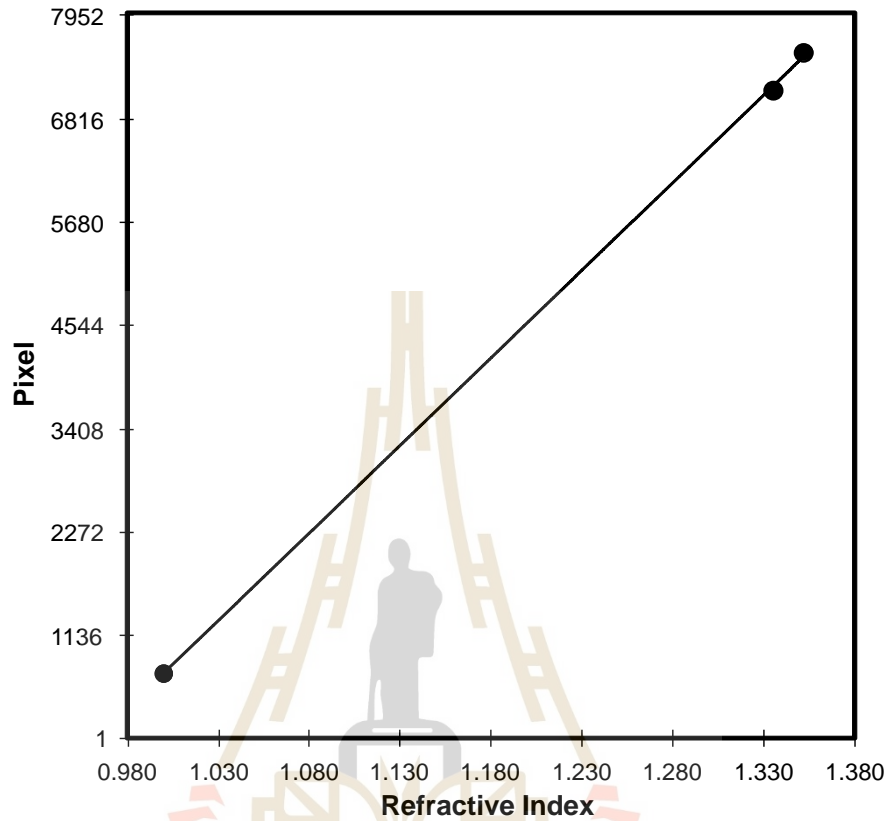


Figure 4.6 Detected SPR positions as a function of the refractive index of the test samples.

The sensor system was calibrated by using the SPR measurements of the sample refractive indices. It is found that the first and the last pixels of the light detector correspond to the angles of 33.806° and 56.802° , respectively, with the angular resolution of 0.00289° . In comparison with the theoretical values, the angle differences may be caused by a misalignment of the distance AE .

When the SPR sensors are implemented without using the mechanical scanning system, the sensitivity is widely expressed in terms of RIU/pixel (Bremer and Roth 2015, Vestri, Margheri et al. 2020). **Figure 4.6** shows a plot the pixel positions of the resultant SPR dips detected by the CMOS sensor as a function the sample refractive index. The detected dip positions represented by black circles fit very well with a straight line, which represents the linear regression line given by $y = 19221x -$

18510 and a coefficient of correlation $R = 0.99992$. The linear sensitivity of the SPR sensor system calculated from the regression line is 5.2026×10^{-5} RIU/pixel, which is close to a theoretical value of 5.1627×10^{-5} RIU/pixel for given parameters of the same sensor.

Table 4.1 Errors in measurements of the refractive indices and their corresponding resonance angles of the three samples (Widjaja and Hossea 2021).

Samples	Theory			Experiment					
	Pixel	RI	β_{spr}	Pixel	% Error	RI	% Error	β_{spr}	% Error
Air	717	1.0003	35.878	713	-0.6	1.000	-0.028	35.865	-0.036
Water	7002	1.3317	54.104	7107	1.50	1.335	0.271	54.358	0.469
Ethanol	7675	1.3580	56.002	7523	-1.98	1.352	-0.439	55.561	-0.787

Table 4.1 presents errors in measurements of the refractive indices and their corresponding resonance angles of the three samples. It is apparent that the refractive index of air can be detected with the smallest error, because it has the sharpest SPR dip. When the width of the SPR dip becomes broader due to the increase in refractive index of the sample, the error in measurement becomes higher. It is worth mentioning that although the measured range of the refractive indices is broad, the highest error is smaller than 1%. Unlike other SPR sensor, which employs an advanced mathematical transformation to extract the dip SPR (Karabchevsky, Karabchevsky et al. 2011), our experimental results are obtained by a simple arithmetic averaging. This confirms that the divergent beam produced by the Powell lens carries uniform energy distribution, yielding the SPR curve with high signal-to-noise ratio. Therefore, this SPR sensor can be used to measure refractive index of sample, which is spatially distributed across the sensing area. The first straight forward application of this type of SPR sensor is an implementation of multichannel SPR sensing, where the sensing area is partitioned into multiple sensing elements (Han and Luo 2013, Wang, Loo et al. 2018). Each sensing element detects different analyte. The second application is a large dynamic range SPR. In this application, the SPR can be implemented without the use of high prism refractive index (Canning, Qian et al. 2015). In summary, the measurement results verify

the validity of the proposed divergent beam illumination and detection proposed in our previous work.

Furthermore, in order to compare with the conventional sensitivity defined according to the mechanical-scanning-based SPR sensor, the theoretical sensitivity of our proposed system can be calculated as (Lan, Liu et al. 2015, Tiwari, Sharma et al. 2015)

$$\begin{aligned} \text{Sensitivity} &= \frac{\Delta\theta_{res}}{\Delta n} = \frac{\theta_{spr-ethanol} - \theta_{spr-air}}{n_{ethanol} - n_{water}}, \\ &= \frac{56.002^\circ - 35.878^\circ}{1.358 - 1.003} \\ &= 56.69^\circ / RIU. \end{aligned} \quad (4.1)$$

From the experiments, the sensitivity is $(55.561^\circ - 35.865^\circ) / (1.352 - 1) = 55.95^\circ / RIU$, which is close to the theoretical sensitivity. The experimental results show that the sensitivity is consistent with the resolution of the angular interrogation technique (Homola, Yee et al. 1999) and it is higher than the other published work (Bremer and Roth 2015).

4.3 Misalignment effects

4.3.1 Simulation Results

This section discusses the simulation results of the effect of the misalignment gap of the ML and air between the glass and the prism shown in Fig. 3.3. The uniform gap is implemented by placing two wedges under the plate edges, while the nonuniform gap uses a single wedge. However, due to difficulty in aligning experimentally a nanometer order wedge, an 80 μm polycarbonate microtube (Paradigm Optics, CTPC-067-100) is used as a wedge between the prism and the gold plate. In the case of the non-uniform gap, the wedge is placed around the interface having high incident angle.

4.3.1.1 Simulation Results of uniform misalignment

Fig. 4.7 shows the total reflectivity $R_{654321} = |r_{654321}|^2$ calculated by using Eq. (3.11) for uniform matching liquid and air gap misalignments. The total reflectance R_{654321} is plotted as the function of the incidence angle θ_1 for the gap thickness $d_2 = 80 \mu\text{m}$. This implies there is either the ML or air gap between the gold coated glass chip and the prism. In comparison with Fig. 3.3 in which the glass thickness was 1 mm, the $80 \mu\text{m}$ thickness of the matching liquid gap does not cause a significant interference fringe change. Therefore, in general, the matching liquid thickness does not produce a reasonable effect on the SPR reflectivity curve.

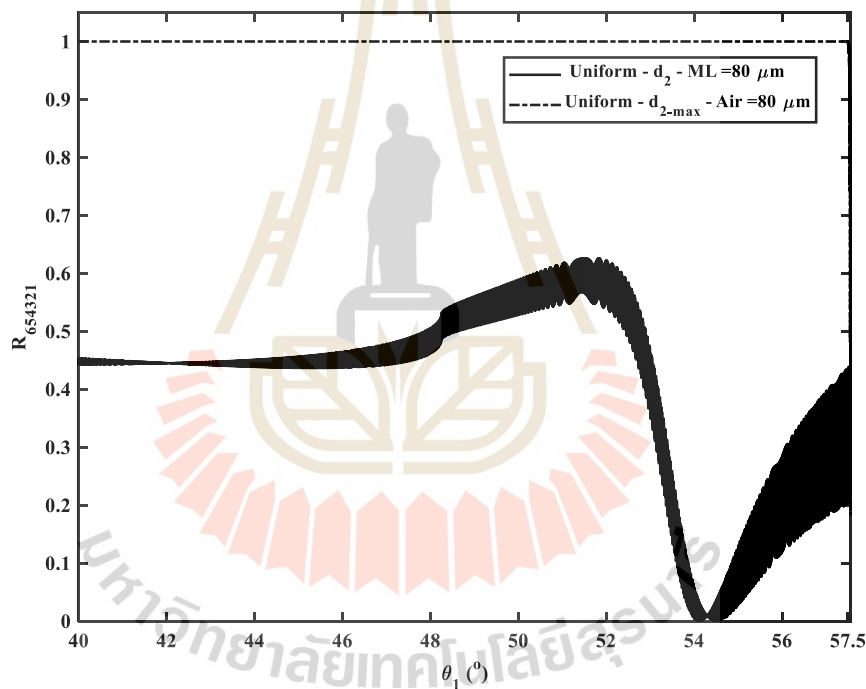


Figure 4.7 Total reflectance power $R_{654321} = |r_{654321}|^2$ as a function of the angle of incidence θ_1 for the $80 \mu\text{m}$ ML and the air gaps.

However, in the case of the $80 \mu\text{m}$ uniform air gap, the reflectivity signal is totally different than the SPR reflectance such that the SPR effect disappears. This is because the thickness of the air gap is longer than the propagation depth of the evanescent wave that is about $1.77 \mu\text{m}$ (Thirstrup, Zong et al. 2004). Thus, the generated evanescent wave diminishes, preventing the resonance of surface plasmons.

the evanescent wave diminishes before it reaches to the gold-sample interface, yielding zero light reflection from the sample. Consequently, the total SPR reflectance R_{654321} becomes zero.

4.3.1.2 Simulation Results of the non-uniform misalignment

Insignificant effect also occurs when the non-uniform ML was applied. A comparison of Figs. 4.8 and 3.3 reveals that the SPR reflectivity curve obtained by the non-uniform misalignment is the same as that by the 1 mm thick gold coated glass plate placed on top of the prism without the ML. It is noteworthy to conclude that due to a larger thickness of the glass than that of the ML, the misalignment gap does not affect significantly the total SPR reflectivity. On the other hand, the effect of the non-uniform air gap is the same as that of the uniform air gap, because of the same short penetration depth of the evanescent wave.

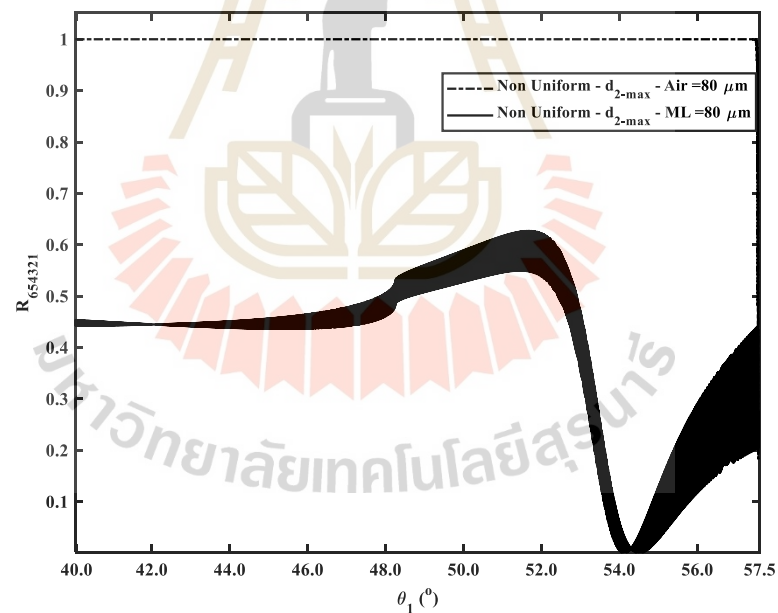


Figure 4.8 Total reflectance power $R_{654321} = |r_{654321}|^2$ as a function of the angle of incidence θ_1 for the non-uniform 80 μm ML and the air gaps.

According to the above results shown in Figs. 4.7 and 4.8, it can be summarized that firstly, the effect of the misalignment gap on the SPR reflectivity is not significant,

provided that the gap is smaller than the glass thickness. Secondly, the ripple fringe is solely produced by the gold-coated glass slide.

4.3.2 Experimental Results

4.3.2.1 Misalignment effects caused by the ML gap

The experiments were carried out to investigate the consequences of the misalignment gap of the ML. The first experiment was done without introducing the gap. A single drop of the ML liquid fill between the prism and the glass plate. Thus, it was deemed a normal scenario. Figures 4.8 (a) and (b) show the SPR reflectivity patterns obtained by using the s- and the p-polarized lights, respectively. The dark band appeared in Fig. 4.9(b) confirm that the p-polarized light resonates the surface plasmons.

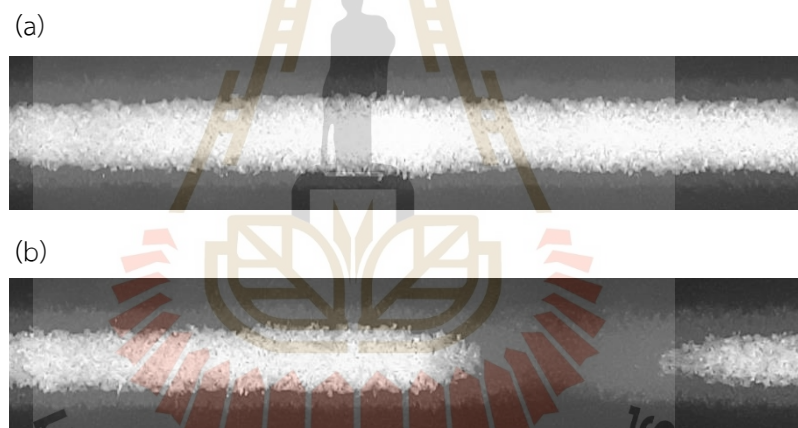


Figure 4.9 The SPR reflectivity patterns obtained by using the (a) S- (b) P-polarized lights.

In the second experiment, the uniform gap was obtained by aligning two 80 μm microtubes used as the wedges. **Fig. 4.10** shows the resultant SPR reflectivity patterns obtained by using the s- and the p-polarized lights. They are depicted in **Fig. 4.10(a)** and **(b)**, respectively. The misalignment effect on the SPR reflectivity pattern is hardly observed.

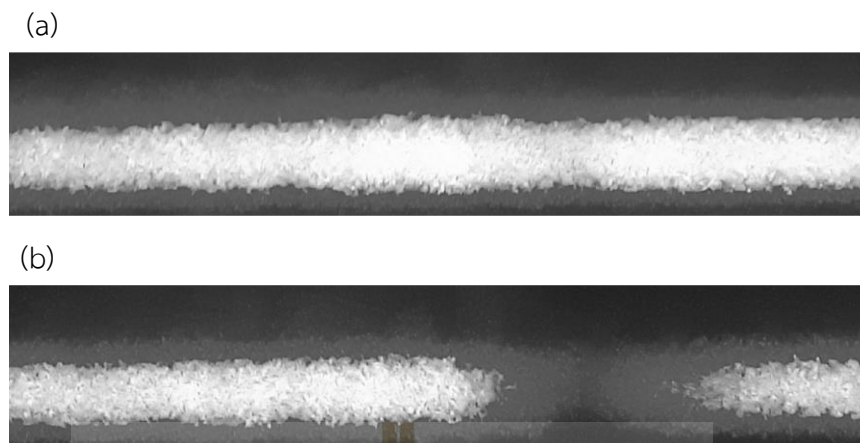


Figure 4.10 Effects of the 80 μm uniform ML gap on the SPR reflectivity patterns obtained by using the (a) S- (b) P-polarized lights.

The last experiment dealt with the non-uniform gap where one of the microtubes was placed under the gold plate with high incident angle. The other side of the plate made contact with the prism. This implies that the glass sensor chip is inclined at an angle defined by the glass sensor chip's length and the microtube diameter. **Fig. 4.11(a)** shows the SPR reflectivity pattern using the S-polarized illumination while **Fig. 4.11(b)** shows the resultant pattern by the P-polarized light. Similar dark band caused by the SPR phenomenon is clearly observed. The results reveal that there is no significant effect of the non-uniform misalignment gap on the SPR reflectivity pattern.

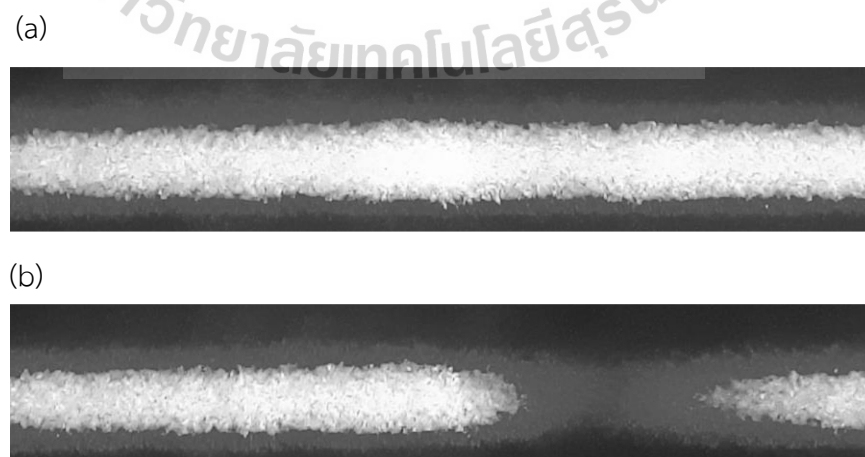


Figure 4.11 Effects of the 80 μm non-uniform ML gap on the SPR reflectivity patterns obtained by using the (a) S- (b) P-polarized lights.

4.3.2.2 Misalignment effect caused by the air gap

Another set of experiments was carried out to investigate the impact of an air bubble at the prism-glass interface. The settings were identical to those used to observe the effect of ML misalignment, with the exception that ML were substituted by air in this case. **Figure 4.12** depicts the resultant SPR reflectivity pattern obtained by using the P-polarized beam patterns for three different types of gap. This study found that there was no occurrence of the SPR phenomenon in any of the three conditions when the air gap was applied



Figure 4.12 The SPR reflectivity patterns obtained by using the p-polarized light with air gap (a) $d_2 = 0 \mu\text{m}$ (b) uniform $d_2 = 80 \mu\text{m}$ and (c) non-uniform $d_2 = 0 - 80 \mu\text{m}$

4.3.3 Discussion of the experimental misalignment effects

Figures 4.13 shows a comparison of the SPR reflectivity signals obtained by using the p-polarized light with and without gaps of the ML and air shown in Figs. 4.9, 4.10, 4.11 and 4.12. The intensities are averaged along the vertical direction. The dashed and the solid lines represent the ML and air gaps. The black, the blue and the red colors denote the normal setup, the 80 μm uniform and the non-uniform gaps, respectively.

The results show that in comparison with the normal SPR alignment, the non-uniform ML gap has insignificant effect on the SPR reflectivity signal. However, the 80 μm uniform ML gap causes the higher minimum dip intensity and the narrower width of the resonance curve. The position of the resonance dip is still detectable. The slight difference in the resonance curve might be caused by the average gap of the uniform misalignment is larger than that of the non-uniform one. The experimental results confirm that the ML gap has insignificant effect on the SPR reflectivity signals, provided that its thickness is smaller than the thickness of the glass sensor chip. Unlike the simulation results shown in Figs. 4.7 and 4.8, the fringe ripple on the experimentally detected SPR signals fluctuates randomly. This can be understood by considering Fig. 4.2, which shows that the divergent beam generated by the Powell lens is not purely uniform.

In the case of the misalignments with the air gap, the experimental results confirm that due to the short penetration depth of the evanescent wave, the larger air gap prevents the photon energy transfer. The SPR phenomenon cannot occur.

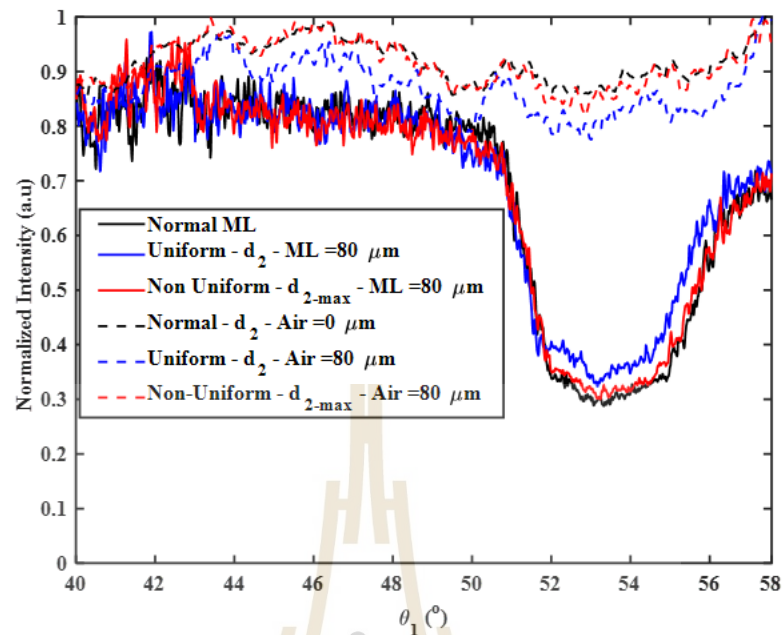


Figure 4.13 Normalized SPR reflectivity signals obtained by using the p-polarized light with and without gaps of the ML and air as a function of the angle of incidence θ_1 for (a) Normal ML and no air gap noted by black and dashed black line (b) uniform ML and air gap $d_2 = 80 \mu\text{m}$ noted by blue and dashed-blue line (c) Non-uniform ML and air gap d_2 maximum = $80 \mu\text{m}$ denoted by red and dashed-red line.

4.4 Experimental analysis of the fringe spacing.

The simulation and the experimental results have verified that the misalignment effect caused by the ML has no discernible effect on the SPR performance. This is because the thickness of the glass sensor chip is greater than the ML gap. On the other hand, the glass thickness causes the interference fringe ripple on the SPR reflectivity signal, which overrides the effect of the glass plate misalignment. In this section, the existence of the interference fringe is experimentally verified. In order to compare with the theoretical spacings, the experimentally generated SPR reflectivity signal of the 1-mm glass plate without the gap is enlarged between the same angle range as Fig. 3.5. The existence of the fringe ripple on the enlarged reflectance around the resonance angle of 54° can be clearly seen in Fig. 4.14. In the figure, the alternate reflectance peaks are denoted by numbers $P_1, P_2, P_3, P_4, P_5, P_6, P_7$,

P_8 , P_9 and P_{10} . The separation between the alternate reflectance peaks were measured as the fringe spacing.

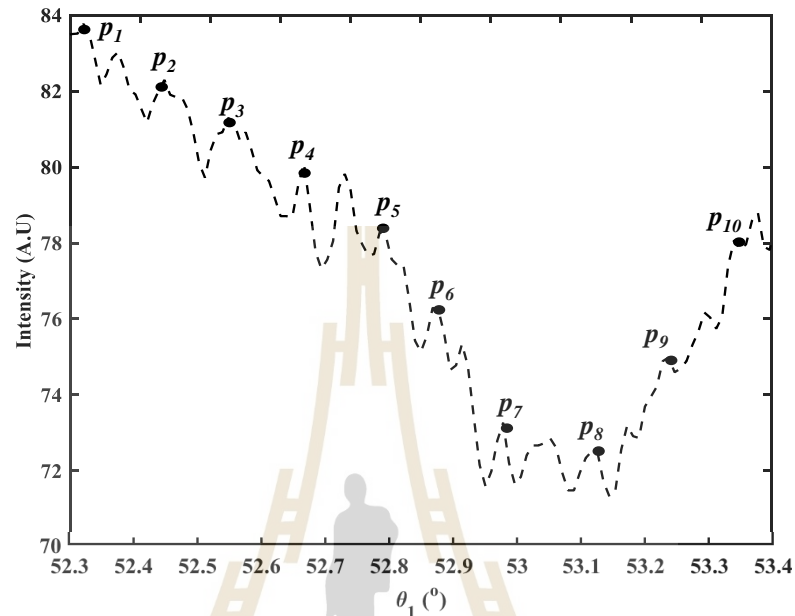


Figure 4.14 Enlarged SPR reflectivity signal of the 1-mm glass plate without gap shown in Fig. 4.13 as the function of the incident angle.

Table 4.2 presents a comparison of the fringe spacings obtained from of the experimental measurement and the theoretical values of Eq. (3.29) as a function of the incident angle θ_1 . The experimentally measured fringe spacing is about six times greater than the theoretical value. The reason for this discrepancy is that unlike the simulated reflectance, the experimentally measured spacings were obtained from the SPR reflectance pattern recorded at the sensor plane in free space away from the prism side BC . Since a larger refraction effect occurs when light travels from the prism to free space, the output beam transmitted from the prism widens before being detected by the sensor. This is the reason for the significant discrepancy.

Table 4.2 Comparison of the experimental and the theoretical fringe spacings as the function of the incident angle θ_1 .

Spacing number	θ_1 (°)	Fringe Spacing		
		Experimental (°)		Equation (3.29) (°)
1	52.3000	$P_2 - P_1$	0.163929	0.023779
2	52.4004	$P_3 - P_2$	0.128802	0.023738
3	52.5522	$P_4 - P_3$	0.152221	0.023690
4	52.7046	$P_5 - P_4$	0.163930	0.023641
5	52.8098	$P_6 - P_5$	0.093674	0.023608
6	52.9501	$P_7 - P_6$	0.140511	0.023565
7	53.1377	$P_8 - P_7$	0.175639	0.023507
8	53.2780	$P_9 - P_8$	0.140511	0.023464
9	53.4000	$P_{10} - P_9$	0.140511	0.023425

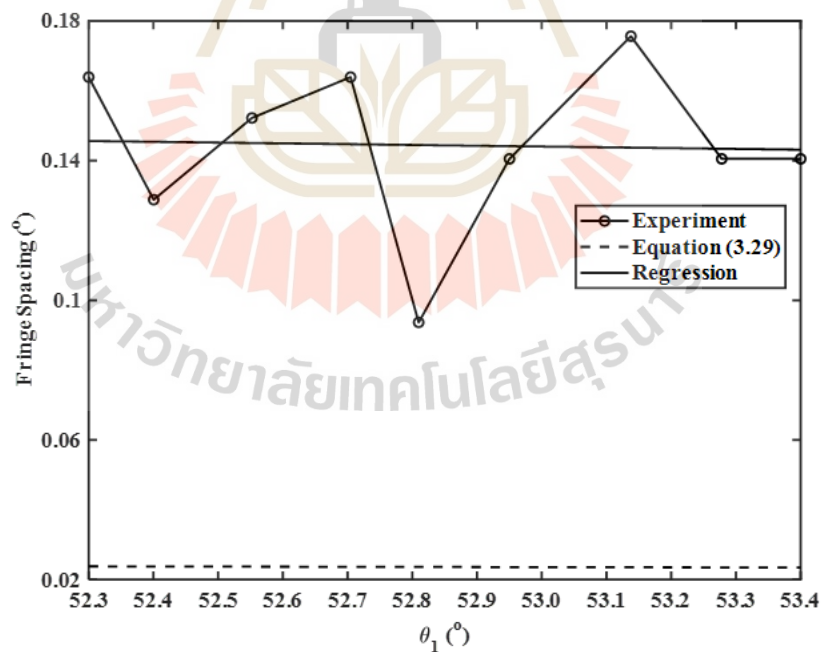
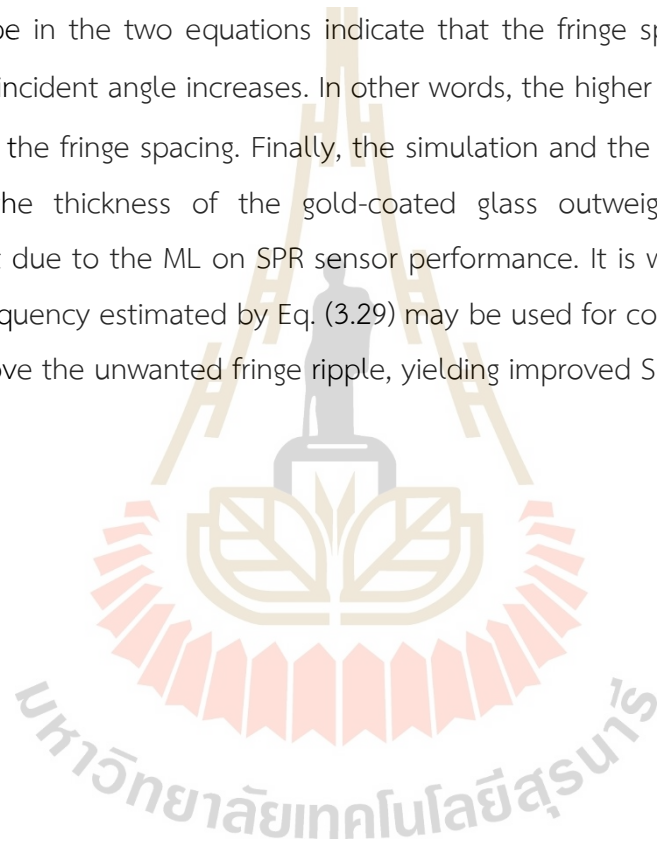


Figure 4.15 Plots of the experimental and the theoretical fringe spacings as the function of the incident angle θ_1 .

To further confirm that the ripple on the SPR signals is caused by the glass thickness, the two spacings are plotted in Figure 4.15. A regression analysis is then used to analyze a variation of the fringe spacing as a function of the incident angle θ_1 . The solid line represents the regression line. The experimentally measured fringe spacing and the incident angle is found to be linearly correlated with the regression equation $f_{s\text{-exp}} = -0.00226\theta_1 + 0.26384$. In the case of the theoretical spacing, the equation is $f_{s\text{-t}} = -0.00031\theta_1 + 0.04$. They have the same relationship strength $R^2 = 0.98$. The negative slope in the two equations indicate that the fringe spacing has downward trend as the incident angle increases. In other words, the higher the incident angle θ_1 , the narrower the fringe spacing. Finally, the simulation and the experimental findings show that the thickness of the gold-coated glass outweighs the influence of misalignment due to the ML on SPR sensor performance. It is worth mentioning that the fringe frequency estimated by Eq. (3.29) may be used for constructing a bandpass filter to remove the unwanted fringe ripple, yielding improved SPR reflectivity signals.



CHAPTER V

CONCLUSION AND FUTURE WORK

5.1 Conclusion

We have verified experimentally the validity of our proposed theory for the divergent beam illumination and detection of the surface plasmon resonance (SPR) sensor by using air, water and absolute ethanol as test samples. In each experiment, simultaneous SPR sensing of two refractive indices of samples, air–water and air–ethanol, were demonstrated. The experimental results show that the SPR sensor system has a linear response to a large range of refractive index measurement. The sensor sensitivity is comparable to the conventional angular interrogation-based SPR and can be enhanced by reducing the index measurement range. The errors in the refractive index measurements are smaller than 1%, with the sensing of air gives the smallest error, while ethanol is the highest. The increase in error stems from the broadening of the SPR dip. All resultant SPR dips have almost the same lowest depth, regardless of their corresponding resonance angles; therefore, the results verify also the advantages of using Powell lens in that first, due to uniform divergent beam illumination photon energy can be efficiently transferred into the surface across broad sensing area. Second, the well-defined SPR reflectivity pattern simplifies the detection algorithm of the SPR dip.

We theoretically and experimentally investigated the ML and air gap effects of the misaligned gold-coated glass sensing plate on the SPR reflectivity signals. The results show that firstly, due to different refractive indices, the illuminating light rays experience multiple reflections and refractions at the glass plate, yielding the interference fringes in the SPR reflectivity signals. Secondly, when the glass thickness increases, the fringe amplitude becomes higher. Thirdly, the ML gap effects of the misaligned glass plate on the SPR signals is insignificant when the gap is less than the glass thickness. This is because the ML has the refractive index closed to the glass and the prism. In contrast, the air gap affects significantly the SPR signals, because air hinders photon energy transfer. When there is no interaction between the surface charges and photons, the SPR phenomenon does not occur. As a result, it was confirmed that there would be no occurrence of the SPR phenomena.

5.2 Future works

Projects in the pipeline include:

- i. To implement a multi-channel SPR sensor by using Powell lens.
- ii. To design a filter which can attenuate the interference fringes.
- iii. To design a flow cell which can be used for implementing multichannel detections.
- iv. To modify the gold sensor chip which can increase selectivity or sensitivity for real world application such as detection bacteria in foods.
- v. To design a software which can be used for real-time SPR signal detections and calculating the rate of the reaction.

5.3 Challenges in implementing

Several practical challenges encountered during the execution of this research were as follows.

The first challenge was related to the alignment of the readout laser beam. This was because the primary surface of Powell lens has a small radius curvature and a relatively large conic constant. In order to ensure that the output beam diverged from the lens secondary surface is evenly distributed, the alignment of the laser beam incident on the conic surface was stringent. The second one was that the alignment of the Powell lens with respect to the entrance side *AC* of the prism. Precise positioning of the small lens closed to the prism requires a custom-made holder. The third one was that the use of big and heavy prism required a custom-made holder which was rotatable and stable. The last challenge was that the beam output size required a large image sensor which was costly.

REFERENCES

- Autolab, M. "Home." Retrieved 1st, July, 2022, from <https://www.metrohmautolab.com/Index.html>.
- Basso, C. R., C. D. Malossi, A. Haisi, V. de Albuquerque Pedrosa, A. N. Barbosa, R. T. Grotto and J. P. A. Junior (2021). "Fast and reliable detection of SARS-CoV-2 antibodies based on surface plasmon resonance." *Analytical Methods* 13(29): 3297-3306.
- Beusink, J. B., A. M. Lokate, G. A. Besselink, G. J. Pruijn and R. B. Schasfoort (2008). "Angle-scanning SPR imaging for detection of biomolecular interactions on microarrays." *Biosensors and Bioelectronics* 23(6): 839-844.
- Bio-Rad. "ProteOn™ XPR36 Protein Interaction Array System " Retrieved 1st, July, 2022, from <https://www.bio-rad.com/en-th/product/proteon-xpr36-protein-interaction-array-system?ID=ea380548-08ca-4b4e-896b-87e5580ac411>.
- Boruah, R., D. Mohanta, A. Choudhury, P. Nath and G. A. Ahmed (2015). "Surface plasmon resonance-based protein bio-sensing using a Kretschmann configured double prism arrangement." *IEEE Sensors Journal* 15(12): 6791-6796.
- Bremer, K. and B. Roth (2015). "Fibre optic surface plasmon resonance sensor system designed for smartphones." *Optics express* 23(13): 17179-17184.
- Bruker. "Surface plasmon resonance (SPR) Sierra SPR®-32 Pro." Retrieved 1st, July, 2022, from <https://www.bruker.com/en/products-and-solutions/surface-plasmon-resonance/sierra-spr-32-pro.html>.
- Canning, J., J. Qian and K. Cook (2015). "Large dynamic range SPR measurements using a ZnSe prism." *Photonic Sensors* 5(3): 278-283.
- Chan, B. L. and S. Jutamulia (2012). SPR prism sensor using laser line generator. *Plasmonics in Biology and Medicine IX*, International Society for Optics and Photonics.
- Chen, R., M. Wang, S. Wang, H. Liang, X. Hu, X. Sun, J. Zhu, L. Ma, M. Jiang and J. Hu (2015). "A low Cost surface plasmon resonance biosensor using a laser line generator." *Optics Communications* 349: 83-88.
- Chen, W. and J. Chen (1981). "Use of surface plasma waves for determination of the thickness and optical constants of thin metallic films." *JOSA* 71(2): 189-191.
- Chinowsky, T., J. Quinn, D. Bartholomew, R. Kaiser and J. Elkind (2003). "Performance of the Spreeta 2000 integrated surface plasmon resonance affinity sensor."

- Sensors and Actuators B: Chemical 91(1-3): 266-274.
- Daniyal, W. M. E. M. M., Y. W. Fen, N. A. A. Anas, N. A. S. Omar, N. S. M. Ramdzan, H. Nakajima and M. A. Mahdi (2019). "Enhancing the sensitivity of a surface plasmon resonance-based optical sensor for zinc ion detection by the modification of a gold thin film." RSC Advances 9(71): 41729-41736.
- Devanarayanan, V., V. Manjuladevi and R. Gupta (2016). "Surface plasmon resonance sensor based on a new opto-mechanical scanning mechanism." Sensors and Actuators B: Chemical 227: 643-648.
- Forzani, E. S., H. Zhang, W. Chen and N. Tao (2005). "Detection of heavy metal ions in drinking water using a high-resolution differential surface plasmon resonance sensor." Environmental science & technology 39(5): 1257-1262.
- Geng, J., E. Zhang and X. Yu (2012). "A scanning surface plasmon resonance sensor based on the phase shift algorithm." Measurement Science and Technology 23(4): 045105.
- Geng, Z., Q. Li, W. Wang and Z. Li (2010). "PDMS prism-glass optical coupling for surface plasmon resonance sensors based on MEMS technology." Science China Information Sciences 53(10): 2144-2158.
- Gordon, J. G. and J. D. Swalen (1977). "The effect of thin organic films on the surface plasma resonance on gold." Optics Communications 22(3): 374-376.
- Gwon, H. R. and S. H. Lee (2010). "Spectral and angular responses of surface plasmon resonance based on the Kretschmann prism configuration." Materials transactions 51(6): 1150-1155.
- Hale, G. M. and M. R. Querry (1973). "Optical constants of water in the 200-nm to 200- μ m wavelength region." Applied optics 12(3): 555-563.
- Han, C.-Y. and C.-W. Luo (2013). "An ellipsometric surface plasmon resonance system for quantitatively determining the normal of a sensor surface and multi-channel measurement." Optics Communications 294: 8-12.
- Hariharan, P. (2010). Basics of interferometry, Elsevier.
- Hickel, W. and W. Knoll (1991). "Time- and spatially resolved surface plasmon optical investigation of the photodesorption of Langmuir-Blodgett multilayer assemblies." Thin Solid Films 199(2): 367-373.
- Homola, J., H. Vaisocherová, J. Dostálek and M. Piliarik (2005). "Multi-analyte surface plasmon resonance biosensing." Methods 37(1): 26-36.
- Homola, J., S. S. Yee and G. Gauglitz (1999). "Surface plasmon resonance sensors." Sensors and actuators B: Chemical 54(1-2): 3-15.
- Hong, D., T. Kim, K. Kim, J. Yuk and K. Ha (2007). "Development of an immunosensor

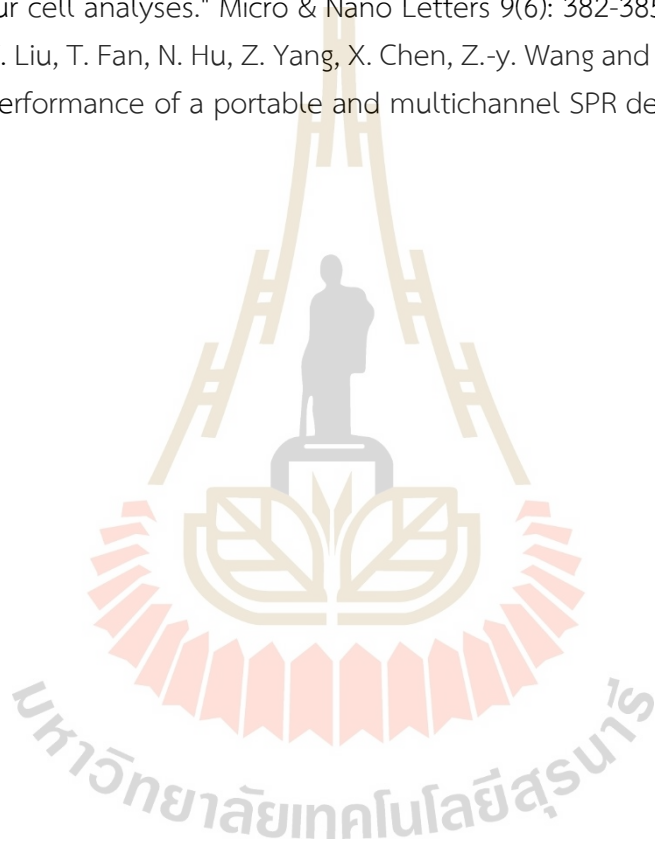
- with angular interrogation-based SPR spectroscopy." *Measurement Science and Technology* 18(5): 1367.
- Hossain, M. and M. Rana (2016). "Graphene coated high sensitive surface plasmon resonance biosensor for sensing DNA hybridization." *Sensor Letters* 14(2): 145-152.
- Hossea, J. and J. Widjaja (2020). "Effects of Prism Types and Materials on Divergent Beam Illumination and Detection in Surface Plasmon Resonance (SPR) Sensors." *International Journal of Laser Science* 1(1): 71-85
- Huang, C.-J., G. V. Narasimha, Y.-C. Chen, J.-K. Chen and G.-C. Dong (2021). "Measurement of Low Concentration of Micro-Plastics by Detection of Bioaffinity-Induced Particle Retention Using Surface Plasmon Resonance Biosensors." *Biosensors* 11(7): 219.
- Isaacs, S. and I. Abdulhalim (2015). "Long range surface plasmon resonance with ultra-high penetration depth for self-referenced sensing and ultra-low detection limit using diverging beam approach." *Applied Physics Letters* 106(19): 193701.
- Karabchevsky, A., S. Karabchevsky and I. Abdulhalim (2011). "Fast surface plasmon resonance imaging sensor using Radon transform." *Sensors and Actuators B:Chemical* 155(1): 361-365.
- Kausaite, A., M. van Dijk, J. Castrop, A. Ramanaviciene, J. P. Baltrus, J. Acaite and A. Ramanavicius (2007). "Surface plasmon resonance label-free monitoring of antibody antigen interactions in real time." *Biochemistry and Molecular Biology Education* 35(1): 57-63.
- Kooyman, R. P., A. T. Lenferink, R. G. Eenink and J. Greve (1991). "Vibrating mirror surface plasmon resonance immunosensor." *Analytical chemistry* 63(1): 83-85.
- Kretschmann, E. (1972). "Decay of non radiative surface plasmons into light on rough silver films. Comparison of experimental and theoretical results." *Optics Communications* 6(2): 185-187.
- Kretschmann, E. and H. Raether (1968). "Radiative decay of non radiative surface plasmons excited by light." *Zeitschrift für Naturforschung A* 23(12): 2135-2136.
- Lan, G., S. Liu, X. Zhang, Y. Wang and Y. Song (2015). "A simplified high figure-of-merit prism-free surface plasmon resonance refractive index sensor based on self adaptive angular interrogation." *Review of Scientific Instruments* 86(2): 025006.
- Lenferink, A. T., R. Kooyman and J. Greve (1991). "An improved optical method for surface plasmon resonance experiments." *Sensors and Actuators B: Chemical* 3(4): 261-265.
- Liang, H., H. Miranto, N. Granqvist, J. W. Sadowski, T. Viitala, B. Wang and M. Yliperttula

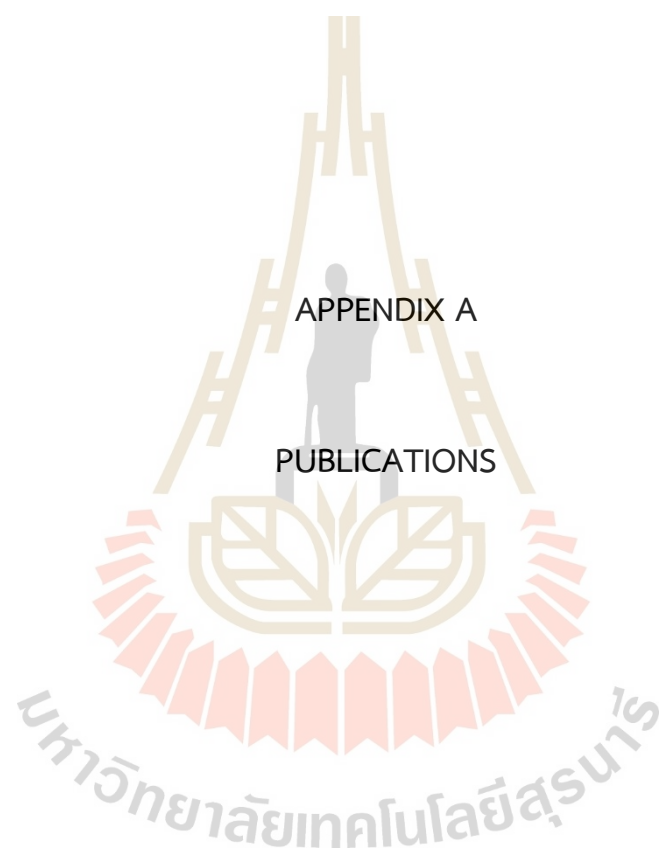
- (2010). "Surface plasmon resonance instrument as a refractometer for liquids and ultrathin films." *Sensors and Actuators B: Chemical* 149(1): 212-220.
- Life Sciences, P. a. s. s. "SPR NAVI™ 220A – the automated mp-SPR." Retrieved 1st, July, 2022, from <https://scisol.com.au/product/spr-navi-220a-automated-mp-spr/>.
- Lokate, A. M., J. B. Beusink, G. A. Besselink, G. J. Pruijn and R. B. Schasfoort (2007). "Biomolecular interaction monitoring of autoantibodies by scanning surface plasmon resonance microarray imaging." *Journal of the American Chemical Society* 129(45): 14013-14018.
- Sensiby Ltd. "SPR molecular interaction instrument." Retrieved 1st, July, 2022, from <http://sensiby.com/en/index.php?m=content&c=index&a=lists&catid=15>.
- Matsubara, K., S. Kawata and S. Minami (1988). "Optical chemical sensor based on surface plasmon measurement." *Applied optics* 27(6): 1160-1163.
- Mauriz, E., A. Calle, J. Manclus, A. Montoya and L. M. Lechuga (2007). "Multi-analyte SPR immunoassays for environmental biosensing of pesticides." *Analytical and bioanalytical chemistry* 387(4): 1449-1458.
- Mauriz, E., A. Calle, J. Manclus, A. Montoya and L. M. Lechuga (2007). "On-line determination of 3, 5, 6-trichloro-2-pyridinol in human urine samples by surface plasmon resonance immunosensing." *Analytical and bioanalytical chemistry* 387(8): 2757-2765.
- Mazumdar, S. D., M. Hartmann, P. Kämpfer and M. Keusgen (2007). "Rapid method for detection of Salmonella in milk by surface plasmon resonance (SPR)." *Biosensors and Bioelectronics* 22(9-10): 2040-2046.
- Mitsushio, M., K. Miyashita and M. Higo (2006). "Sensor properties and surface characterization of the metal-deposited SPR optical fiber sensors with Au, Ag, Cu, and Al." *Sensors and Actuators A: Physical* 125(2): 296-303.
- Mohanty, B. C. and S. Kasiviswanathan (2005). "Two-prism setup for surface plasmon resonance studies." *Review of scientific instruments* 76(3): 033103.
- Moznuzzaman, M., I. Khan and M. R. Islam (2021). "Nano-layered surface plasmon resonance-based highly sensitive biosensor for virus detection: A theoretical approach to detect SARS-CoV-2." *AIP Advances* 11(6): 065023.
- Nanospr. "NanoSPR77 – Dual Channel Electrochemical Surface Plasmon Resonance Spectrometer." Retrieved 1st, July, 2022, from <https://nanospr.com/nanospr77-dual-channel-electrochemical-surface-plasmon-resonance-spectrometer/>.
- Nguyen, H. H., S. Y. Yi, A. Woubit and M. Kim (2016). "A portable surface plasmon resonance biosensor for rapid detection of Salmonella typhimurium." *Applied*

- Science and Convergence Technology 25(3): 61-65.
- O'Brien II, M. J., V. c. H. Pérez-Luna, S. Brueck and G. P. López (2001). "A surface plasmon resonance array biosensor based on spectroscopic imaging." *Biosensors and Bioelectronics* 16(1-2): 97-108.
- Ohta, K. and H. Ishida (1990). "Matrix formalism for calculation of electric field intensity of light in stratified multilayered films." *Applied optics* 29(13): 1952-1959.
- Olsen, R. G. and D. Rouseff (1985). "On the wave impedance for power lines." *IEEE transactions on power apparatus and systems*(3): 711-717.
- Otto, A. (1968). "Excitation of nonradiative surface plasma waves in silver by the method of frustrated total reflection." *Zeitschrift für Physik A Hadrons and nuclei* 216(4): 398-410.
- Otto, A. (1968). "Excitation of nonradiative surface plasma waves in silver by the method of frustrated total reflection." *Zeitschrift für Physik* 216(4): 398-410.
- Palumbo, M., C. Pearson, J. Nagel and M. Petty (2003). "A single chip multi-channel surface plasmon resonance imaging system." *Sensors and Actuators B: Chemical* 90(1-3): 264-270.
- Photonicsys. "Technology Photonicsys Surface Plasmon Resonance Sensors." Retrieved 1st, July, 2022, from <https://www.photonicsys.com/technology>.
- Plasmetrix. "Surface Plasmon Resonance Technology." Retrieved 27, July, 2022, from <https://plasmetrix.com/technology/>.
- Powell, I. (1989). Linear deiverging lens, Google Patents.
- Raikwar, S., Y. Prajapati, D. Srivastava and J. Saini (2020). "Graphene oxide based SPR sensor for sensing of sea water concentration." *Results in Optics* 1: 100011.
- Saleviter, S., Y. W. Fen, N. Sheh Omar, W. Daniyal, J. Abdullah and M. A. Mahdi (2020). "Label-free binding analysis of 4-(2-Pyridylazo)-resorcinol-based composite layer with cobalt ion using surface plasmon resonance optical sensor." *Sens. Mater* 32: 2877-2889.
- Shalabney, A. and I. Abdulhalim (2010). "Electromagnetic fields distribution in multilayer thin film structures and the origin of sensitivity enhancement in surface plasmon resonance sensors." *Sensors and Actuators A: Physical* 159(1): 24-32.
- Sharma, A. K., R. Jha and H. S. Pattanaik (2010). "Design considerations for surface plasmon resonance based detection of human blood group in near infrared." *Journal of Applied Physics* 107(3): 034701.
- Shin, Y.-B., H. M. Kim, Y. Jung and B. H. Chung (2010). "A new palm-sized surface plasmon resonance (SPR) biosensor based on modulation of a light source by

- a rotating mirror." *Sensors and Actuators B: Chemical* 150(1): 1-6.
- Tao, N., S. Boussaad, W. Huang, R. Arechabaleta and J. D'Agnese (1999). "High resolution surface plasmon resonance spectroscopy." *Review of Scientific Instruments* 70(12): 4656-4660.
- Technologies, I. "Publications." Retrieved 1st, July, 2022, from <https://www.ibis-spr.nl/inhoud/uploads/151015-WP1-Specifications-of-the-MX96.pdf>.
- Thirstrup, C., W. Zong, M. Borre, H. Neff, H. Pedersen and G. Holzhueter (2004). "Diffractive optical coupling element for surface plasmon resonance sensors." *Sensors and Actuators B: Chemical* 100(3): 298-308.
- Tiwari, K., S. C. Sharma and N. Hozhabri (2015). "High performance surface plasmon sensors: Simulations and measurements." *Journal of Applied Physics* 118(9): 093105.
- Uddin, S. M. A., S. S. Chowdhury and E. Kabir (2021). "Numerical analysis of a highly sensitive surface plasmon resonance sensor for sars-cov-2 detection." *Plasmonics*: 1-13.
- VanWiggeren, G. D., M. A. Bynum, J. P. Ertel, S. Jefferson, K. M. Robotti, E. P. Thrush, D. M. Baney and K. P. Killeen (2007). "A novel optical method providing for high-sensitivity and high-throughput biomolecular interaction analysis." *Sensors and Actuators B: Chemical* 127(2): 341-349.
- Vestri, A., G. Margheri, E. Landini, E. Meacci and B. Tiribilli (2020). "A versatile and compact surface plasmon resonance spectrometer based on single board computer." *Review of Scientific Instruments* 91(1): 013106.
- Wang, D., F.-C. Loo, H. Cong, W. Lin, S. K. Kong, Y. Yam, S.-C. Chen and H. P. Ho (2018). "Real-time multi-channel SPR sensing based on DMD-enabled angular interrogation." *Optics express* 26(19): 24627-24636.
- Widjaja, J. and J. Hossea (2021). "Experimental Validations of Divergent Beam Illumination and Detection Conditions in a Surface Plasmon Resonance Sensor Using a Powell Lens." *Lasers in Engineering (Old City Publishing)* 48: 17-32
- J. Workman (2001). *Handbook of Organic Compounds: Methods and Interpretations*, Academic Press.
- Yamamoto, M. (2002). "Surface plasmon resonance (SPR) theory: tutorial." *Review of Polarography* 48(3): 209-237.
- Zagorodko, O., J. Bouckaert, T. Dumych, R. Bilyy, I. Larroulet, A. Yanguas Serrano, D. Alvarez Dorta, S. G. Gouin, S.-O. Dima and F. Oancea (2015). "Surface plasmon resonance (SPR) for the evaluation of shear-force-dependent bacterial adhesion." *Biosensors* 5(2): 276-287.

- Zainuddin, N. H., Y. W. Fen, A. A. Alwahib, M. H. Yaacob, N. Bidin, N. A. S. Omar and M. A. Mahdi (2018). "Detection of adulterated honey by surface plasmon resonance optical sensor." *Optik* 168: 134-139.
- Zeng, Y., J. Zhou, X. Xiao, L. Wang, J. Qu, X. Li, B. Z. Gao and Y. Shao (2019). "A Speckle-Free Angular Interrogation SPR Imaging Sensor Based on Galvanometer Scan and Laser Excitation." *Plasmonics* 14(6): 1497-1504.
- Zhang, L., X. Chen, H. Wei, H. Li, J. Sun, J. Chen and D. Cui (2014). "Development of dual-channel surface plasmon resonance imaging system applied to living tumour cell analyses." *Micro & Nano Letters* 9(6): 382-385.
- Zhang, X.-l., Y. Liu, T. Fan, N. Hu, Z. Yang, X. Chen, Z.-y. Wang and J. Yang (2017). "Design and performance of a portable and multichannel SPR device." *Sensors* 17(6): 1435.





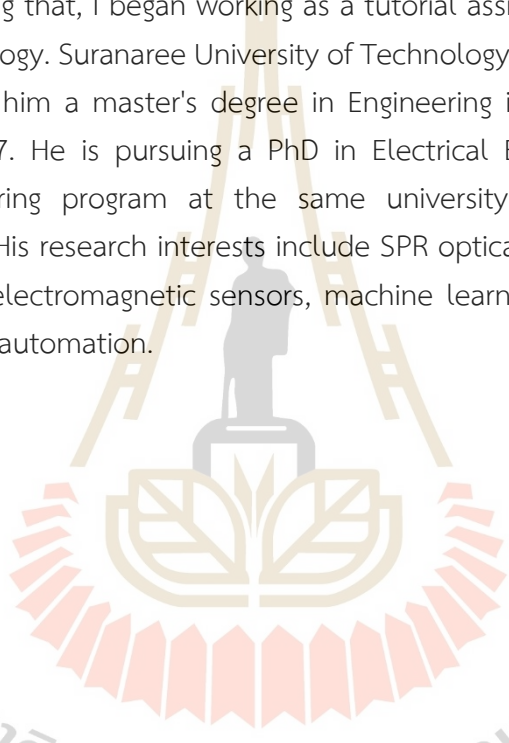
Publications that are related to this research work are included.

- 1 J. Widjaja and J. H. Hossea. "Experimental Validations of Divergent Beam Illumination and Detection Conditions in a Surface Plasmon Resonance Sensor Using a Powell Lens." *Lasers in Engineering* (Old City Publishing), pp. 17-32, (2021).
- 2 J. H. Hossea and J. Widjaja, "Effects of Misalignment Gap of Sensing Chip on Resonant Reflectivity in Divergent Beam-based Surface Plasmon Resonance Sensor," in *2020 International Electrical Engineering Congress (iEECON)*, Chiang Mai, Thailand, 2020



BIOGRAPHY

Mr. Jordan Hakim Hossea was born in Tanzania's Morogoro area, in the Kilombero district. In 2012, he obtained his Bachelor of Engineering in Electronic and Communication Engineering from Tanzania's Saint Joseph University in Dar-es-Salaam. From October 2012 to October 2013, he worked as a tutorial assistant at St Joseph University. Following that, I began working as a tutorial assistant at the Dar es Salaam Institute of Technology. Suranaree University of Technology (SUT), Nakhon Ratchasima, Thailand, awarded him a master's degree in Engineering in Electronic and Photonic Engineering in 2017. He is pursuing a PhD in Electrical Engineering as part of the Electronic Engineering program at the same university, Suranaree University of Technology (SUT). His research interests include SPR optical sensors and instruments, bioelectronics, bioelectromagnetic sensors, machine learning, the Internet of Things (IoT) and industrial automation.



มหาวิทยาลัยเทคโนโลยีสุรนารี